

Low-Dimensional Nanostructures for Optoelectronic Applications

Guest Editors: Wen Lei, Lorenzo Faraone, H. Hoe Tan, and Wei Lu





Low-Dimensional Nanostructures for Optoelectronic Applications

Low-Dimensional Nanostructures for Optoelectronic Applications

Guest Editors: Wen Lei, Lorenzo Faraone, H. Hoe Tan,
and Wei Lu



Copyright © 2014 Hindawi Publishing Corporation. All rights reserved.

This is a special issue published in “Journal of Nanomaterials.” All articles are open access articles distributed under the Creative Commons Attribution License, which permits unrestricted use, distribution, and reproduction in any medium, provided the original work is properly cited.

Editorial Board

Domenico Acierno, Italy
Katerina E. Aifantis, USA
Sheikh Akbar, USA
Nageh K. Allam, USA
Margarida Amaral, Portugal
Jordi Arbiol, Spain
Raul Arenal, Spain
Ilaria Armentano, Italy
Xuedong Bai, China
Lavinia Balan, France
Thierry Baron, France
Andrew R. Barron, USA
Hongbin Bei, USA
Stefano Bellucci, Italy
Enrico Bergamaschi, Italy
D. Bhattacharyya, New Zealand
Giovanni Bongiovanni, Italy
T. Borca-Tasciuc, USA
M. Bououdina, Bahrain
C. Jeffrey Brinker, USA
Christian Brosseau, France
Yibing Cai, China
Chuanbao Cao, China
Xuebo Cao, China
Victor M. Castaño, Mexico
Albano Cavaleiro, Portugal
Bhanu P. S. Chauhan, USA
Wei Chen, China
Yuan Chen, Singapore
Tupei Chen, Singapore
Shafiul Chowdhury, USA
Kwang-Leong Choy, UK
Jin-Ho Choy, Korea
Yu-Lun Chueh, Taiwan
Elisabetta Comini, Italy
Giuseppe Compagnini, Italy
M. A. Correa-Duarte, Spain
P. Davide Cozzoli, Italy
Majid Darroudi, Iran
Shadi A. Dayeh, USA
Yong Ding, USA
Bin Dong, China
Zehra Durmus, Turkey
Joydeep Dutta, Oman
Ali Eftekhari, USA

Samy El-Shall, USA
Farid El-Tantawy, Egypt
Ovidiu Ersen, France
Claude Estournès, France
Andrea Falqui, Saudi Arabia
Xiaosheng Fang, China
Bo Feng, China
Matteo Ferroni, Italy
W. Fritzsche, Germany
Alan Fuchs, USA
Lian Gao, China
Peng Gao, China
Miguel A. Garcia, Spain
Siddhartha Ghosh, Singapore
P. K. Giri, India
Russell E. Gorga, USA
Jihua Gou, USA
Alexander Govorov, USA
Jean M. Greneche, France
Changzhi Gu, China
Hongchen Chen Gu, China
Mustafa O. Guler, Turkey
John Z. Guo, USA
Lin Guo, China
Smrati Gupta, Germany
K. Hamad-Schifferli, USA
Michael Harris, USA
Jr-Hau He, Taiwan
Nguyen D. Hoa, Vietnam
Zhongkui Hong, China
Michael Z. Hu, USA
Nay Ming Huang, Malaysia
Qing Huang, China
Shaoming Huang, China
David Hui, USA
Zafar Iqbal, USA
B. Jeyadevan, Japan
Sheng-Rui Jian, Taiwan
Xin Jiang, Germany
Wanqin Jin, China
Rakesh K. Joshi, UK
Myung-Hwa Jung, Korea
Jeong-won Kang, Korea
Zhenhui Kang, China
Hassan Karimi-Maleh, Iran

Fathallah Karimzadeh, Iran
Antonios Kelarakis, UK
Alireza Khataee, Iran
Ali Khorsand Zak, Iran
Wonbaek Kim, Korea
Jang-Kyo Kim, Hong Kong
Dojin Kim, Korea
Philippe Knauth, France
Christian Kübel, Germany
Prashant Kumar, UK
Sanjeev Kumar, India
Sushil Kumar, India
Subrata Kundu, India
Alan K. T. Lau, Hong Kong
Michele Laus, Italy
Eric Le Bourhis, France
Burtrand Lee, USA
Jun Li, Singapore
Benxia Li, China
Xing-Jie Liang, China
Meiyong Liao, Japan
Shijun Liao, China
Silvia Licoccia, Italy
Wei Lin, USA
Gong-Ru Lin, Taiwan
Jun Liu, USA
Tianxi Liu, China
Zainovia Lockman, Malaysia
Jue Lu, USA
Songwei Lu, USA
Ed Ma, USA
Malik Maaza, South Africa
Lutz Mädler, Germany
Gaurav Mago, USA
Morteza Mahmoudi, Iran
Santanu K. Maiti, India
Mohammad A. Malik, UK
Devanesan Mangalaraj, India
Sanjay R. Mathur, Germany
V. Mittal, United Arab Emirates
Paulo Cesar Morais, Brazil
Mahendra A. More, India
Paul Munroe, Australia
Jae-Min Myoung, Korea
Rajesh Naik, USA



Albert Nasibulin, Russia
Toshiaki Natsuki, Japan
Weihai Ni, China
Koichi Niihara, Japan
Sherine Obare, USA
W.-C. Oh, Republic of Korea
Atsuto Okamoto, Japan
Abdelwahab Omri, Canada
Ungyu Paik, Republic of Korea
Edward A. Payzant, USA
Ton Peijs, UK
Kui-Qing Peng, China
O. Perales-Perez, Puerto Rico
A. Phuruangrat, Thailand
Wenxiu Que, China
S. Sinha Ray, South Africa
Peter Reiss, France
Orlando Rojas, USA
Marco Rossi, Italy
Cengiz S. Ozkan, USA
Vladimir Šepelák, Germany
Ugur Serincan, Turkey
Huaiyu Shao, Japan
Prashant K. Sharma, India
Donglu Shi, USA

Bhanu P. Singh, India
Surinder Singh, USA
Vladimir Sivakov, Germany
Yanlin Song, China
Ashok Sood, USA
Marinella Striccoli, Italy
Bohua Sun, South Africa
Jing Sun, China
Xuping Sun, Saudi Arabia
Ashok K. Sundramoorthy, USA
Sabine Szunerits, France
Nyan-Hwa Tai, Taiwan
Bo Tan, Canada
Somchai Thongtem, Thailand
Ion Tiginyanu, Moldova
Alexander Tolmachev, Ukraine
Valeri P. Tolstoy, Russia
Muhammet S. Toprak, Sweden
Ramon Torrecillas, Spain
Takuya Tsuzuki, Australia
Tamer Uyar, Turkey
Bala Vaidhyanathan, UK
Luca Valentini, Italy
Rajender S. Varma, USA
Raquel Verdejo, Spain

Antonio Villaverde, Spain
Ajayan Vinu, Australia
Zhenbo Wang, China
Shiren Wang, USA
Yong Wang, USA
Ruibing Wang, Macau
Magnus Willander, Sweden
Xingcai Wu, China
Zhi Li Xiao, USA
Ping Xiao, UK
Shuangxi Xing, China
Yangchuan Xing, USA
Doron Yadlovker, Israel
Yingkui Yang, China
Piaoping Yang, China
Yoke K. Yap, USA
Ramin Yousefi, Iran
William W. Yu, USA
Kui Yu, Canada
Haibo Zeng, China
Bin Zhang, China
Renyun Zhang, Sweden
Yanbao Zhao, China
L. Zheng, United Arab Emirates
Chunyi Zhi, Hong Kong

Contents

Low-Dimensional Nanostructures for Optoelectronic Applications, Wen Lei, Lorenzo Faraone, H. Hoe Tan, and Wei Lu
Volume 2014, Article ID 734614, 2 pages

Crystallites of α -Sexithiophene in Bilayer Small Molecule Organic Solar Cells Double Efficiency, Michal Radziwon, André Luis Fernandes Cauduro, Morten Madsen, and Horst-Günter Rubahn
Volume 2014, Article ID 482372, 6 pages

Hydrothermal Synthesis and Mechanism of Unusual Zigzag Ag_2Te and $\text{Ag}_2\text{Te}/\text{C}$ Core-Shell Nanostructures, Saima Manzoor, Yumin Liu, Zhongyuan Yu, Xiuli Fu, and Guijun Ban
Volume 2014, Article ID 350981, 5 pages

Void Structures in Regularly Patterned ZnO Nanorods Grown with the Hydrothermal Method, Yu-Feng Yao, Chen-Hung Shen, Wei-Fang Chen, Pei-Ying Shih, Wang-Hsien Chou, Chia-Ying Su, Horng-Shyang Chen, Che-Hao Liao, Wen-Ming Chang, Yean-Woei Kiang, and C. C. Yang
Volume 2014, Article ID 756401, 11 pages

Effects of Polaron and Quantum Confinement on the Nonlinear Optical Properties in a $\text{GaAs}/\text{Ga}_{1-x}\text{Al}_x\text{As}$ Quantum Well Wire, L. Caroline Sugirtham, A. John Peter, and Chang Woo Lee
Volume 2014, Article ID 823065, 6 pages

Preparation and Characterization of Graphene Oxide, Jianguo Song, Xinzhi Wang, and Chang-Tang Chang
Volume 2014, Article ID 276143, 6 pages

Second-Order Nonlinearity Assisted by Dual Surface Plasmon Resonance Modes in Perforated Gold Film, Renlong Zhou, Guozheng Nie, Lingxi Wu, Qiong Liu, Suxia Xie, Mengxiong Wu, Lisan Zeng, and Yingyi Xiao
Volume 2014, Article ID 252950, 7 pages

The Formation Site of Noninterfacial Misfit Dislocations in InAs/GaAs Quantum Dots, Shuai Zhou, Yumin Liu, Pengfei Lu, Lihong Han, and Zhongyuan Yu
Volume 2014, Article ID 103640, 5 pages

Mixed Phases at the Bottom Interface of Si-Doped AlGaIn Epilayers of Optoelectronic Devices, Chen-hui Yu, Qing-zhou Luo, Xiang-dong Luo, and Pei-sheng Liu
Volume 2014, Article ID 729041, 5 pages

Nonnegative Matrix Factorization Numerical Method for Integrated Photonic Cavity Based Spectroscopy, Zhengyu Huang, Dayuan Xiong, Guixu Zhang, Yiqin Shi, Changning Hao, and Junli Duan
Volume 2014, Article ID 310601, 5 pages

Improving Light Outcoupling Efficiency for OLEDs with Microlens Array Fabricated on Transparent Substrate, Jun Wang, Weizhi Li, and Chong Wang
Volume 2014, Article ID 289752, 6 pages

Thickness-Dependent Strain Effect on the Deformation of the Graphene-Encapsulated Au Nanoparticles, Shuangli Ye, Honghua Huang, Cailei Yuan, Feng Liu, Min Zhai, Xinzhi Shi, Chang Qi, and Gaofeng Wang
Volume 2014, Article ID 989672, 6 pages



Strain Distribution of Au and Ag Nanoparticles Embedded in Al₂O₃ Thin Film, Honghua Huang,
Ying Zhang, Cailei Yuan, Gang Gu, and Shuangli Ye
Volume 2014, Article ID 471718, 4 pages

A Flexible Blue Light-Emitting Diode Based on ZnO Nanowire/Polyaniline Heterojunctions, Y. Y. Liu,
X. Y. Wang, Y. Cao, X. D. Chen, S. F. Xie, X. J. Zheng, and H. D. Zeng
Volume 2013, Article ID 870254, 4 pages

Editorial

Low-Dimensional Nanostructures for Optoelectronic Applications

Wen Lei,¹ Lorenzo Faraone,¹ H. Hoe Tan,² and Wei Lu³

¹ School of Electrical, Electronic and Computer Engineering, The University of Western Australia, 35 Stirling Highway, Crawley, WA 6009, Australia

² Department of Electronic Materials Engineering, Australian National University, Acton, ACT 0200, Australia

³ Shanghai Institute of Technical Physics, Chinese Academy of Sciences, 500 Yutian Road, Hongkou, Shanghai 200083, China

Correspondence should be addressed to Wen Lei; wen.lei@uwa.edu.au

Received 20 August 2014; Accepted 20 August 2014; Published 23 December 2014

Copyright © 2014 Wen Lei et al. This is an open access article distributed under the Creative Commons Attribution License, which permits unrestricted use, distribution, and reproduction in any medium, provided the original work is properly cited.

In recent years, low-dimensional (zero-, one-, and two-dimensional) nanostructures have attracted wide attention and become a focus of scientific research and engineering application. This is due to their novel physical and chemical properties caused by size and quantum effects, as well as potential applications in various kinds of devices, for example, optoelectronics, nanoelectronics, and so forth. This special issue is intended to bring the most recent advances in the field of low-dimensional nanostructures for optoelectronic applications. As expected, the research articles in this special issue cover a wide range of topics in this research field, ranging from theoretical simulation to material synthesis, to material characterization, to device fabrication, and to device characterization.

In the paper “*The formation site of noninterfacial misfit dislocations in InAs/GaAs quantum dots*,” S. Zhou et al. simulate the preferential formation site of noninterfacial 60° mixed dislocations in InAs/GaAs quantum dots and find that the positions near the right edge of the quantum dot are the energetically favourable areas for these dislocations. In the paper “*Thickness-dependent strain effect on the deformation of the graphene-encapsulated Au nanoparticles*,” S. Ye et al. simulate the effect of strain on the morphology of graphene-encapsulated Au nanoparticles. The modelling results indicate that strain and deformation can be designed by the graphene layer thickness, providing an opportunity to engineer the structure and morphology of the graphene-encapsulated nanoparticles. In the paper “*Strain distribution of Au and Ag nanoparticles embedded in Al₂O₃ thin*

film,” H. Huang et al. calculate the strain distribution in Au and Ag nanoparticles embedded in amorphous Al₂O₃ matrix. The calculation results indicate that both the Au and Ag nanoparticles incur compressive strain caused by the Al₂O₃ matrix. However, the compressive strain existing on the Au nanoparticle is much weaker than that on the Ag nanoparticle. This different strain distribution of Au and Ag nanoparticles in the same host matrix may have a significant influence on the technological potential applications of the Au-Ag alloy nanoparticles.

In the paper “*Second-order nonlinearity assisted by dual surface plasmon resonance modes in perforated gold film*,” R. Zhou et al. report the enhanced light transmission (assisted with surface plasmon) through a nanoscale square lattice perforated gold film. In the paper “*Effects of polaron and quantum confinement on the nonlinear optical properties in a GaAs/Ga_{1-x}Al_xAs quantum well wire*,” L. C. Sugirtham et al. calculate the binding energy of a polaron confined in a GaAs/Ga_{1-x}Al_xAs quantum well wire with the variational technique and Lee-Low Pines approach and study the effect of polaron and quantum confinement on the nonlinear optical properties of GaAs/Ga_{1-x}Al_xAs quantum well wire. In the paper “*Nonnegative matrix factorization numerical method for integrated photonic cavity based spectroscopy*,” Z. Huang et al. use a nonnegative matrix factorization method to improve the spectral resolution of integrated photonic cavity based spectroscopy. The spectral resolution can be improved from 5.5 to 1.8 nm, which is helpful for enhancing the spectral resolution of miniature spectrometers.

In the paper “*Void structures in regularly patterned ZnO nanorods grown with the hydrothermal method*,” Y.-F. Yao et al. study the effect of thermal annealing on the void structures and optical properties of ZnO nanorod arrays obtained by hydrothermal method, which provides good understanding about the structural change of ZnO nanorods under thermal annealing. In the paper “*Hydrothermal synthesis and mechanism of unusual zigzag Ag_2Te and $\text{Ag}_2\text{Te}/\text{C}$ core-shell nanostructures*,” S. Manzoor et al. fabricate the zigzag silver telluride nanowires and silver telluride coated with carbon core-shell nanowires via simple hydrothermal route, which has promising applications in optoelectronic devices. In the paper “*Preparation and characterization of graphene oxide*,” J. Song et al. report the fabrication of graphene oxide films with the modified Hummer method, which presents a promising way to synthesize graphene oxide films on a large scale. In the paper “*Mixed phases at the bottom interface of Si-doped AlGaIn epilayers of optoelectronic devices*,” C.-h. Yu et al. present a study of the crystalline structures of Si-doped $\text{Al}_{0.4}\text{Ga}_{0.6}\text{In}$ layers grown on unintentionally doped AlGaIn buffer layer with an AlIn nucleation layer, which is helpful for understanding the fundamental properties of high aluminium content Si-doped AlGaIn alloys and providing specific guidance on the fabrication of multilayer optoelectronic devices where weak cubic subgrains potentially occur and exert complicated influence on device performance.

In the paper “*Improving light outcoupling efficiency for OLEDs with microlens array fabricated on transparent substrate*,” J. Wang et al. utilize microlens array substrate to increase the light output efficiency of organic LED, which is very encouraging. In the paper “*A flexible blue light-emitting diode based on ZnO nanowire/polyaniline heterojunctions*,” Y. Y. Liu et al. report an organic/inorganic light-emitting diode consisting of n-type vertically aligned ZnO nanowires and p-type proton acid doped polyaniline. A broad blue light emission band ranging from 390 to 450 nm is observed for the device, and the turn-on voltage of the device is ~ 3.5 V. In combination with easy fabrication, flexibility, low power consumption, and mechanical robustness, this novel device is very promising for the application of blue light-emitting diodes. In the paper “*Crystallites of α -sexithiophene in bilayer small molecule organic solar cells double efficiency*,” M. Radziwon et al. present an interesting study on the α -6T/ C_{60} inverted bilayer organic solar cells by investigating the influence of α -sexithiophene (α -6T) nanostructures on the performance parameters. It is found that the crystalline nanostructures can significantly improve the device conversion efficiency.

In summary, as reflected by its content this special issue provides a broad panorama for research in this specific field and will benefit the readers, especially those working in this field.

Acknowledgments

We would like to thank our reviewers for their time and comments and thank the authors for their contributions to

this special issue. This special issue could not have been successful without their contribution and support.

Wen Lei
Lorenzo Faraone
H. Hoe Tan
Wei Lu

Research Article

Crystallites of α -Sexithiophene in Bilayer Small Molecule Organic Solar Cells Double Efficiency

Michal Radziwon, André Luis Fernandes Cauduro,
Morten Madsen, and Horst-Günter Rubahn

Mads Clausen Institute, University of Southern Denmark, NanoSYD, Alsion 2, 6400 Sønderborg, Denmark

Correspondence should be addressed to Michal Radziwon; michal@radziwon.pl

Received 29 December 2013; Revised 30 March 2014; Accepted 31 March 2014; Published 11 May 2014

Academic Editor: Wen Lei

Copyright © 2014 Michal Radziwon et al. This is an open access article distributed under the Creative Commons Attribution License, which permits unrestricted use, distribution, and reproduction in any medium, provided the original work is properly cited.

Recent efforts in research and development of small molecule based organic solar cells have led to power conversion efficiencies exceeding 10%. Understanding the incorporated interfaces in these devices is an utterly important parameter for their improvement. Here we investigate the influence of α -sexithiophene (α -6T) nanostructures on the performance parameters of α -6T/C₆₀ inverted bilayer solar cells. By *in situ* controlled growth, crystalline α -6T nanostructures are formed in the devices and a correlation between the morphology of the structures and the device performance is presented. Under certain, well-defined circumstances, we observe an efficiency increase of around 100% when implementing crystalline nanostructures.

1. Introduction

The device performance of small molecule organic solar cells has significantly advanced in recent years and power conversion efficiencies of up to 12% have now been reached [1]. As demonstrated in the past, one of the methods to improve the performance of small molecule devices is through controlled formation of organic nanoscale crystalline structures, as this can lead to both an increased donor-acceptor interface area and an improved intermolecular packing in the donor layer [2, 3], which in turn can lead to both improved charge carrier generation and charge transport properties in the devices. The importance of molecular packing is due to the fact that in conjugated oligomers a strong anisotropy in the charge transport properties is observed, which can be attributed to the anisotropy of the molecules themselves. In the case of α -sexithiophene (α -6T), the herringbone packed monoclinic crystalline system ensures a strong π - π overlap in the planes parallel to the long molecular axes, whereas the overlap in the planes perpendicular to the long molecular axes is small.

In the past, it has been demonstrated that the nanocrystalline morphology in small molecule organic solar cells

could be optimized through, for example, thermal [3, 4] or solvent [5] annealing processes as well as by the use of solvent additives [2]. Work on *in situ* controlled growth of crystalline nanostructures from physical vapor deposition through oblique angle deposition [6] has also been demonstrated as a way of improving the performance of small molecule based solar cells. In the present study, we focus on *in situ* controlled growth of α -6T nanoscale crystalline structures for solar cell applications. Previously, it has been shown that structures varying in shape, size, and molecular packing can be obtained from α -6T thin films formed through organic molecular beam deposition (OMBD) on various substrates including mica [7], titanium oxides [8], and gold [9]. We recently demonstrated the growth of α -6T nanoscale structures on C₆₀ thin films [10], which, especially from a device point of view, is interesting, as it allows for direct implementation in inverted organic solar cells. The α -6T/fullerene system has previously been investigated in standard configuration solar cells [4] and despite the fact that the power conversion efficiencies of these systems are not higher than 1% for standard configuration devices [4], amongst others from a poor spectral match between their absorption spectra and

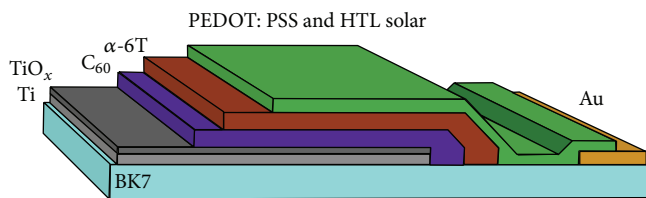


FIGURE 1: Schematic diagram of the inverted α -6T/ C_{60} solar cell structure employed in this work.

the solar spectrum, they are still quite interesting as they can serve as a model system [11] for basic research on processes involved in crystalline organic solar cells. Similar studies on crystalline small molecule bilayer devices have recently been carried out on Rubrene/ C_{60} systems, which show the importance of controlling the molecular packing in small molecule based organic solar cells [12].

In order to utilize the phenomenon of α -6T nanostructure formation on C_{60} films in organic solar cells, the inverted configuration of the investigated system has been chosen (see Figure 1). The solar cells are fabricated on Ti/TiO_x cathodes using a PEDOT:PSS/HTL solar mixture as an anode. The resulting devices show a clear correlation between the power conversion efficiency and the crystalline structure formation, and a 100% increase in power conversion efficiency is obtained at optimum morphology of the α -6T layers.

2. Materials and Methods

300 μ m BK7 glass wafers were precleaned by sonication for 30 s in acetone, rinsed with deionized water, and spindried. A negative photolithography process, followed by e-beam evaporation of a 3 nm Ti adhesive layer and 30 nm of Au, defined the device cathodes and anodes. Then, a shadow mask was introduced to deposit 20 nm of Ti in the cathode regions only, and the wafer was cut into 20 mm \times 10.5 mm substrates containing 6 devices each. Prior to deposition of organic layers, the substrates were precleaned by an ultrasonic bath in acetone for 5 min, rinsed with isopropyl alcohol and deionized water, blow-dried with N₂, and exposed to 130 W RF glow discharge oxygen plasma for 90 s. The latter treatment also forms a thin layer of TiO_x on the surface, which has been demonstrated to work as a cathode interfacial layer in organic solar cells [13].

For formation of the active organic layer, 20 nm of commercially available fullerene C_{60} (Sigma-Aldrich, purity 99.5%) was evaporated in an OMBD system, under a deposition pressure of ca. 10^{-7} mbar and at a growth rate of 0.3 $\text{\AA}/\text{s}$. Subsequently, without breaking the vacuum, 30 nm of commercially available α -6T (Tokyo Chemical Industry Co., Ltd.) was evaporated under the same pressure at a growth rate of 0.1–0.2 $\text{\AA}/\text{s}$ at temperatures of the substrate holder ranging between 300 K and 390 K. A shadow mask defined the desired exposure area. A water-cooled, calibrated quartz microbalance was used for *in situ* detection of the nominal thickness and growth rate. Immediately after the deposition, the substrates were moved into a N₂ dry glove

box where spin coating of a 1:1 mixture of the commercially available conductive polymer HTL SOLAR and CPP PEDOT (Heraeus Precious Metals GmbH & Co. KG) was performed at 1000 RPM for 45 s. The substrates were then annealed for 30 min at 360 K. After 10 min cooldown at room temperature, commercially available UV curable encapsulant (DELO katiobond LPVE) was spun at 4000 RPM for 45 s. A schematic diagram of the device architecture is presented in Figure 1.

The devices were characterized using a Newport 9600 solar simulator with an AM 1.5 G filter set to 1 sun with a Newport 91150-KG1 reference cell. The devices were light-soaked for 15 min prior to measurement. *I*-*V* curves have been taken with a Keithley 2400 series source meter, by scanning in the 0 mV–500 mV bias range. The V_{OC} value was obtained in a separate measurement, where the source meter was set to source zero current. The reported values are the averages of the measurements across the substrate. Afterwards, epifluorescence micrographs were taken (Nikon Eclipse ME-600, Hg lamp, excitation 465 nm–469 nm, detection 515 nm–555 nm). External quantum efficiency (EQE) measurements were performed by irradiating the samples with a 150 W Xe lamp through a Monochromator (VIS-NIR Newport Cornerstone 1/4 m) followed by fiber coupling into a Mitoyo FS-70 microscope. The external quantum efficiency measurements were carried out in air at 300 K using the same conditions aforementioned. A Si calibrated photodiode (Hamamatsu S2386-44 K) was used to measure the incident power. Reflectance measurements were conducted using a Spectroscopic Ellipsometer (TFProbe Sun Angstrom Technology SE200BA) set 45° with respect to normal incidence.

3. Results and Discussion

In order to investigate the effect from heating the substrates during deposition of α -6T molecules on the morphology of the underlying C_{60} layers, AFM scans of the C_{60} layers directly after deposition and after a postannealing treatment at 420 K were conducted. The RMS roughness from the two different scans is 1.5 nm and 1.6 nm, respectively, which demonstrates that the surface morphology does not change during the heating of the substrates (see Figure 2).

The deposition of α -6T molecules at different substrate temperatures led to the formation of thin films with different morphologies. Epifluorescence micrographs of the α -6T thin films obtained at different substrate temperatures are presented in Figure 3. The micrographs were taken through the UV absorbing encapsulant, which required application of suitable filters in the microscope. At room temperature, a rough continuous film is observed, while at 320 K, small (<3 μ m) clusters are formed at individual nucleation points (Figures 3(a) and 3(b)). At 330 K, we observe a mesh of fiber-like structures formed in randomly distributed domains of various sizes, while at 340 K, such structures fully cover the surface area (Figures 3(c) and 3(d)). At an increased substrate temperature of 360 K, the formation of fiber-like structures persists but, contrary to the sample prepared at 340 K, the structures are clearly separated by the areas where

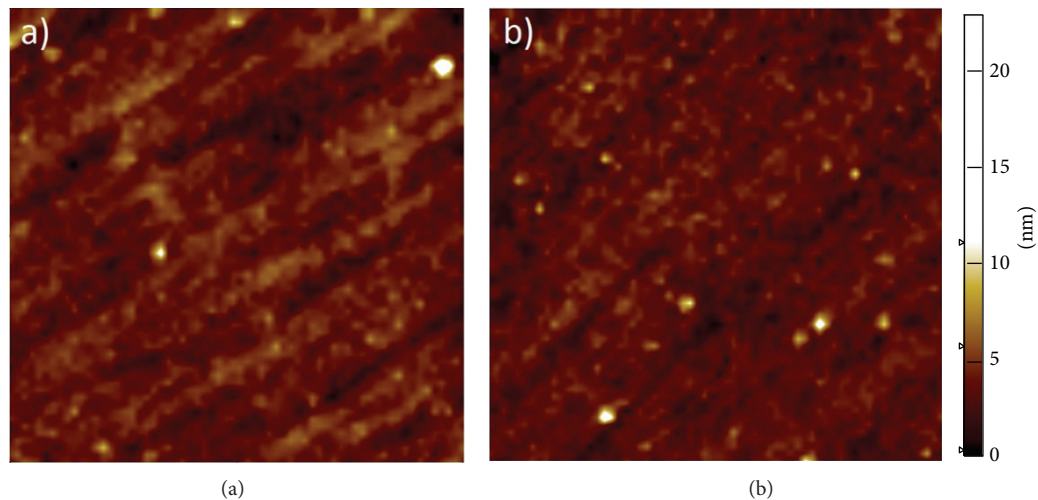


FIGURE 2: 25 μm by 25 μm AFM scans of C_{60} as deposited at room temperature (a) and postannealed at 420 K (b).

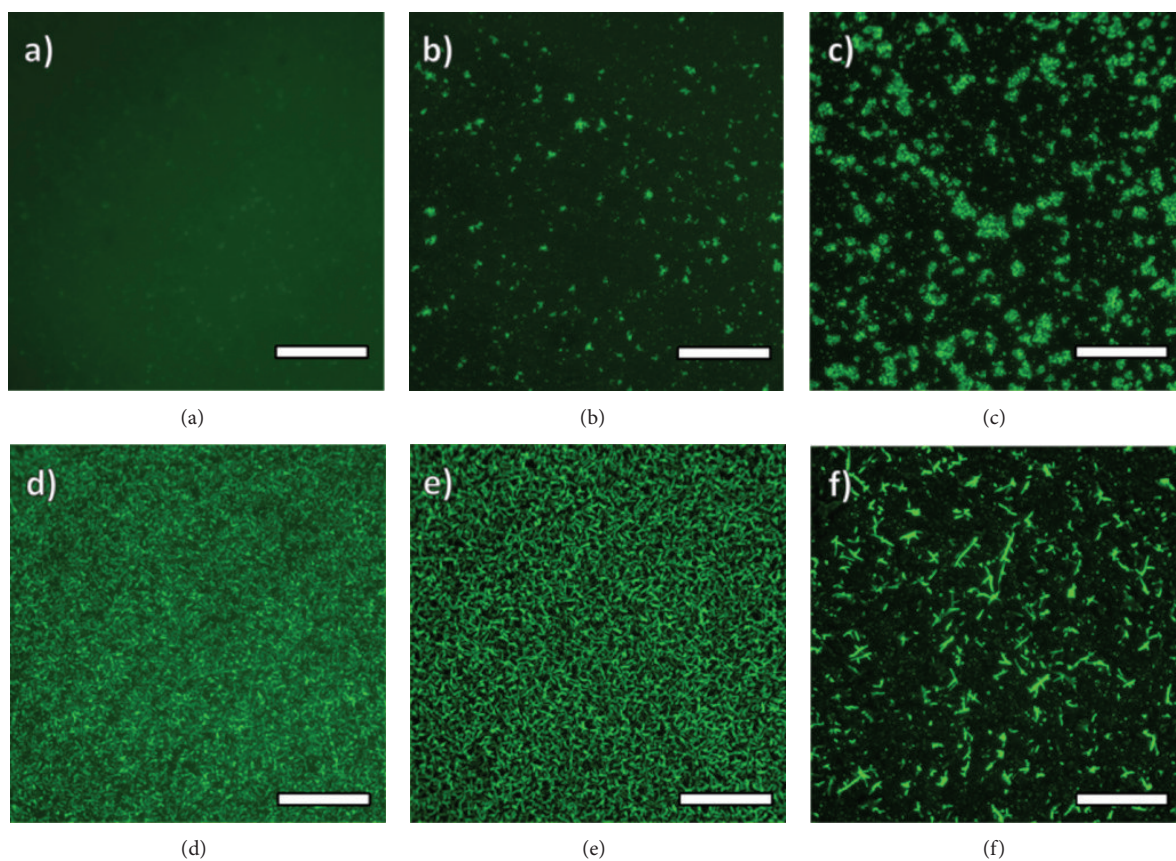


FIGURE 3: Epifluorescence micrographs of $\alpha\text{-6T}/\text{C}_{60}$ solar cells with electron donor layer deposited at 300 K, 320 K, 330 K, 340 K, 360 K, and 390 K, from (a) to (f), respectively. The scale bars are 20 μm . As the encapsulant layer absorbs UV light, 460 nm–495 nm excitation and 515 nm–555 nm emission filters were employed.

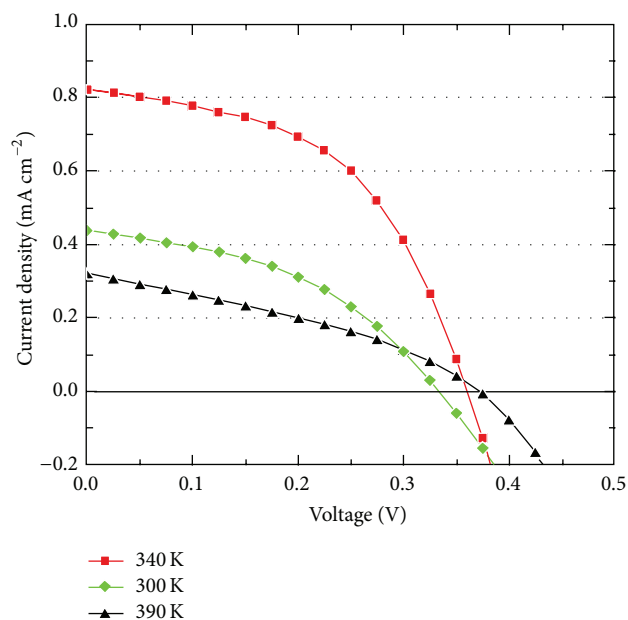


FIGURE 4: J - V curves of organic solar cells fabricated at different substrate temperatures during α -6T.

virtually no fluorescence is observed (Figure 3(e)). At 390 K, 10 μm –20 μm long, straight, and branching fibers are formed, which are surrounded by a mesh of shorter ones $\sim 2 \mu\text{m}$ –5 μm (Figure 3(f)). A similar temperature dependent morphology was observed for thicker (100 nm) α -6T thin films on C_{60} layers, where the crystalline nature was investigated via XRD and fluorescence polarimetry measurements [10]. It could be concluded, that although the films formed at elevated temperatures are dominated mainly by the presence of standing molecules, the formed fiber-like structures consist of lying molecules.

In Figure 4, representative J - V curves from devices consisting of the α -6T layers grown at 300 K, 340 K, and 390 K are shown. At these temperatures, distinct differences in the device performances are obtained, which is related to the morphology of the formed nanostructures. At 330 K–340 K, a mesh of crystalline fibers starts to be formed (Figures 3(c) and 3(d)) along with crystallites consisting of standing molecules. A crystalline structured interface can lead to less trap sites and more efficient exciton dissociation [14], and the lying molecules in fiber-like structures do not only provide areas with preferential orientation of the high mobility axis in the α -6T layer [15, 16] but also facilitate enhanced absorption as the transition dipoles in those are almost perpendicular to the direction of the incident light. The crystallites consisting of standing molecules could also enhance the performance of the devices by facilitating efficient horizontal charge transport from the α -6T nanostructures to the transparent electrode. In combination, these effects should result in an increase of the short circuit current density as well as in a drop of the equivalent series resistance, which can explain the J - V curves for the 340 K devices compared to the 300 K devices. At temperatures higher than 340 K, the surface mobility of

the individual α -6T molecules is high enough to cause the material to form separated fibers, which increase in size with the temperature.

In Figure 5, the characteristic device parameters for the solar cells fabricated with different α -6T morphologies are shown. As expected, the open circuit voltage (V_{OC}) shows only little variation with temperature (Figure 5(a)), mostly due to the fact that its value is predominantly determined by the electronic properties of the materials used [17]. The short circuit current density (J_{SC}), fill factor (FF), and power conversion efficiency (PCE) all exhibit a raise in the 330 K–340 K range (Figures 5(b)–5(d)). The PCE shows an increase of about 100% at a substrate temperature of 340 K in comparison to 300 K. At substrate temperatures of 360 K and higher, larger α -6T fibers are being formed and α -6T depleted areas occur, which leads to a decrease of the overall junction area, which explains the eventual drop in the short circuit current density and PCE.

To further elaborate on the efficiency enhancement observed in devices including crystalline structures formed at 340 K, EQE and effective absorption spectra were taken for cells consisting of α -6T layers grown at 300 K and 340 K, respectively (Figure 6). The effective absorption is here defined as “100%-reflection” of the 340 K sample using the 300 K sample as a reference, as this directly relates to their change in absorption. It is evident that the EQE in the 340 K devices is improved over the investigated wavelength range compared to the 300 K devices. The effective absorption also shows that the 340 K devices exhibit stronger light absorption compared to the 300 K samples, due to the formation of the crystalline nanostructures at the elevated temperature. Notably though, as the EQE ratio (ratio between the EQE at 340 K and the EQE at 300 K, not plotted) remains almost constant over the investigated wavelength range, it can be interpreted that the absorption enhancement is not the main factor for the increase in charge collection at short circuit conditions. The improvement is instead considered to take place following absorption of photons in the cell, namely, in the subsequent exciton dissociation process and charge collection at the electrodes, which can be ascribed to the crystalline structure formation in these devices. The crystalline structure formation could lead to improved exciton dissociation, as recently demonstrated in crystalline Rubrene/ C_{60} solar cells [12], as well as to improved charge transport properties. Similar morphology dependent improvement in charge collection properties has been demonstrated for postannealed small molecule mixed heterojunction cells [18]. Note, however, that in these cells, due to the presence of a mixed heterojunction, the annealing step leads to a change in both the molecular packing and the domain sizes of the acceptor and donor phases.

4. Conclusions

In this work, we have investigated the influence of various α -6T nanostructures, formed by OMBD at substrate temperatures ranging between 300 K and 390 K, on the performance of inverted organic α -6T/ C_{60} solar cells. We have shown that

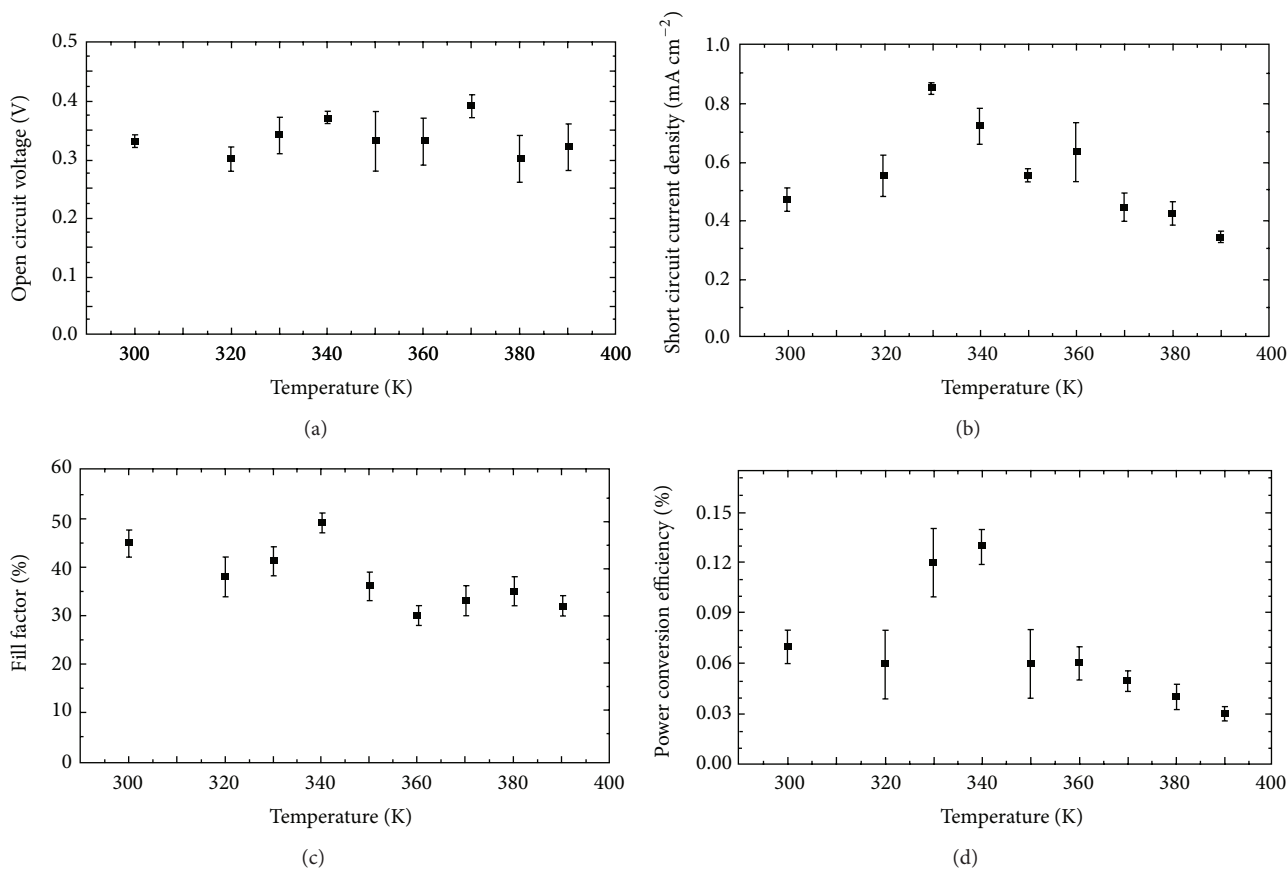


FIGURE 5: Performance parameters α -6T/ C_{60} solar cells with electron donor layer deposited at various surface temperatures.

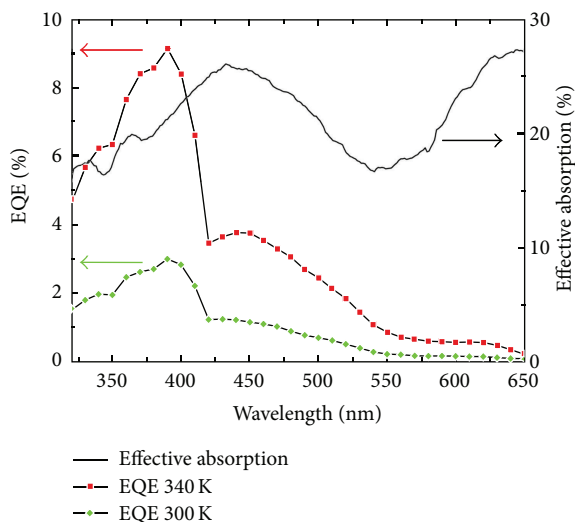


FIGURE 6: External quantum efficiency and effective absorption extracted from “100%-reflection ratio” of the sample α -6T (@340 K)/ C_{60} to α -6T (@300 K)/ C_{60} .

controlled growth of nanostructures in the electron donor layer leads to a power conversion efficiency enhancement of around 100% in the 330 K–340 K temperature range. This

range is characterized by a maximum density of fiber-like structures which due to their internal molecular packing are responsible for improving both the charge carrier generation and collection at the electrodes. At higher temperatures, the low density of larger fibers leads to a reduced junction area and thus a worse device performance.

Conflict of Interests

The authors declare that they have no conflict of interests regarding the publication of this paper.

Acknowledgments

The authors thank the Fabrikant Mads Clausen trust for the financial support of the research presented in this publication. André Luis Fernandes Cauduro is thankful to the CNPq Brazilian research council for granting a scholarship under process no. 213909/2012-0.

References

- [1] Heliatek, “Heliatek consolidates its technology leadership by establishing a new world record for organic solar technology with a cell efficiency of 12%,” 2013, http://www.heliatek.com/newscenter/latest_news/.

- [2] Y. Sun, G. C. Welch, W. L. Leong, C. J. Takacs, G. C. Bazan, and A. J. Heeger, "Solution-processed small-molecule solar cells with 6.7% efficiency," *Nature Materials*, vol. 11, no. 1, pp. 44–48, 2012.
- [3] G. Wei, X. Xiao, S. Wang et al., "Functionalized squaraine donors for nanocrystalline organic photovoltaics," *ACS Nano*, vol. 6, no. 1, pp. 972–978, 2012.
- [4] J. Sakai, T. Taima, T. Yamanari, and K. Saito, "Annealing effect in the sexithiophene: C₇₀ small molecule bulk heterojunction organic photovoltaic cells," *Solar Energy Materials and Solar Cells*, vol. 93, no. 6-7, pp. 1149–1153, 2009.
- [5] G. Wei, S. Wang, K. Sun, M. E. Thompson, and S. R. Forrest, "Solvent-annealed crystalline squaraine: PC70BM (1:6) solar cells," *Advanced Energy Materials*, vol. 1, no. 2, pp. 184–187, 2011.
- [6] N. Li and S. R. Forrest, "Tilted bulk heterojunction organic photovoltaic cells grown by oblique angle deposition," *Applied Physics Letters*, vol. 95, no. 12, Article ID 123309, 2009.
- [7] C. Simbrunner, G. Hernandez-Sosa, M. Oehzelt et al., "Epitaxial growth of sexithiophene on mica surfaces," *Physical Review B: Condensed Matter and Materials Physics*, vol. 83, no. 11, Article ID 115443, 2011.
- [8] J. Ivanco, T. Haber, J. R. Krenn, F. P. Netzer, R. Resel, and M. G. Ramsey, "Sexithiophene films on ordered and disordered TiO₂(1 1 0) surfaces: Electronic, structural and morphological properties," *Surface Science*, vol. 601, no. 1, pp. 178–187, 2007.
- [9] A. J. Mäkinen, J. P. Long, N. J. Watkins, and Z. H. Kafafi, "Sexithiophene adlayer growth on vicinal gold surfaces," *Journal of Physical Chemistry B*, vol. 109, no. 12, pp. 5790–5795, 2005.
- [10] M. Radziwon, M. Madsen, F. Balzer, R. Resel, and H. G. Rubahn, "Growth of a-sexithiophene nanostructures on C₆₀ thin film layers," *Thin Solid Films*, vol. 558, pp. 165–169, 2014.
- [11] S. Veenstra, G. G. Malliaras, H. J. Brouwer et al., "Sexithiophene-C₆₀ blends as model systems for photovoltaic devices," *Synthetic Metals*, vol. 84, no. 1, pp. 971–972, 1997.
- [12] B. Verreet, P. Heremans, A. Stesmans, and B. P. Rand, "Microcrystalline organic thin-film solar cells," *Advanced Materials*, vol. 25, no. 38, pp. 5504–5507, 2013.
- [13] S. Sista, M.-H. Park, Z. Hong et al., "Highly efficient tandem polymer photovoltaic cells," *Advanced Materials*, vol. 22, no. 3, pp. 380–383, 2010.
- [14] J. Halls, K. Pichler, R. Friend, S. Moratti, and A. Holmes, "Exciton diffusion and dissociation in a poly (p-phenylenevinylene)/C₆₀ heterojunction photovoltaic cell," *Applied Physics Letters*, vol. 68, no. 22, pp. 3120–3122, 1996.
- [15] V. Coropceanu, J. Cornil, D. A. da Silva Filho, Y. Olivier, R. Silbey, and J.-L. Brédas, "Charge transport in organic semiconductors," *Chemical Reviews*, vol. 107, no. 4, pp. 926–952, 2007.
- [16] J. Y. Lee, S. Roth, and Y. W. Park, "Anisotropic field effect mobility in single crystal pentacene," *Applied Physics Letters*, vol. 88, no. 25, Article ID 252106, 2006.
- [17] C. J. Brabec, A. Cravino, D. Meissner et al., "Origin of the open circuit voltage of plastic solar cells," *Advanced Functional Materials*, vol. 11, no. 5, pp. 374–380, 2001.
- [18] D. Wynands, M. Levichkova, M. Riede et al., "Correlation between morphology and performance of low bandgap oligothiophene: C₆₀ mixed heterojunctions in organic solar cells," *Journal of Applied Physics*, vol. 107, no. 1, Article ID 014517, 2010.

Research Article

Hydrothermal Synthesis and Mechanism of Unusual Zigzag Ag₂Te and Ag₂Te/C Core-Shell Nanostructures

Saima Manzoor,¹ Yumin Liu,¹ Zhongyuan Yu,¹ Xiuli Fu,² and Guijun Ban²

¹ State Key Laboratory of Information Photonics and Optical Communications, Beijing University of Posts and Telecommunications (BUPT), Beijing 100876, China

² School of Science, State Key Laboratory of Information Photonics and Optical Communications, Beijing University of Posts and Telecommunications (BUPT), Beijing 100876, China

Correspondence should be addressed to Yumin Liu; liuyumintech@hotmail.com and Xiuli Fu; xiulifu@bupt.edu.cn

Received 30 November 2013; Accepted 20 February 2014; Published 23 March 2014

Academic Editor: Wen Lei

Copyright © 2014 Saima Manzoor et al. This is an open access article distributed under the Creative Commons Attribution License, which permits unrestricted use, distribution, and reproduction in any medium, provided the original work is properly cited.

A single step surfactant-assisted hydrothermal route has been developed for the synthesis of zigzag silver telluride nanowires with diameter of 50–60 nm and length of several tens of micrometers. Silver nitrate (AgNO₃) and sodium tellurite (Na₂TeO₃), are the precursors and polyvinylpyrrolidone (PVP) is used as surfactant in the presence of the reducing agent, that is, hydrazine hydrate (N₂H₄·H₂O). In addition to the zigzag nanowires a facile hydrothermal reduction-carbonization route is proposed for the preparation of uniform core-shell Ag₂Te/C nanowires. In case of Ag₂Te/C synthesis process the same precursors are employed for Ag and Te along with the ethylene glycol used as reducing agent and glucose as the carbonizing agent. Morphological and compositional properties of the prepared products are analyzed with the help of scanning electron microscopy, transmission electron microscopy, and energy dispersive X-ray spectroscopy, respectively. The detailed formation mechanism of the zigzag morphology and reduction-carbonization growth mechanism for core-shell nanowires are illustrated on the bases of experimental results.

1. Introduction

The use of 1D nanostructures for advancement in nanoelectronic and optoelectronic devices requires great diversity of structures and needs different morphologies to be synthesized in either bulk form or in thin films. The recent recommendation of new geometric configurations for smart materials has made it essential to set up nanoscale building blocks in axial or radial way that allow another dimension to tune their properties [1–3]. For this reason, the zigzag morphology possessing breaks in the lattice periodicity at junctions exhibits another class of nanostructures that can propose confinement effect and increased excitonic behaviour. Similarly, the core-shell nanostructures present a formal protocol to realize the aim of functional nanomaterials, integrated with multiple roles in single crystal. The isolation of the core from the surroundings can be utilized to prepare such materials or devices whose properties are different from the bare nanomaterials. The shell may be used to reduce the chemical reactivity

of the surface to modify its optical properties or to devise some nanoscale devices with specific electrical functionality. Especially the functionalized carbonaceous nanowires have appealed attention for potential applications.

The monoclinic structure of Ag₂Te is a narrow band gap material with high electron mobility. Until now different morphologies regarding Ag₂Te have been synthesized. For example, the rod-like nanostructure of Ag₂Te was obtained with the use of Te nanorods as the template reagents [4]. Ag₂Te nanotubes were hydrothermally synthesized with the use of sodium tellurite and silver nitrate as the precursors in the presence of hydrazine and ammonia solution [5]. Samal and Sandeep have reported the room temperature synthesis method for synthesizing Ag₂Te nanowires [6]. Most recently, another facile hydrothermal route is reported for Ag₂Te NWs [7]. The same group worked on the morphological evolution and growth mechanism of its nanostructures by employing ammonia as a pH regulator and hydrazine as the reducing agent [8].

To the best of our knowledge, synthesis of zigzag Ag_2Te nanowires and core-shell Ag_2Te nanowires with carbonaceous shell has not been achieved so far. Herein, on the bases of simple hydrothermal conditions we demonstrate that for the synthesis of zigzag Ag_2Te , hydrazine is used as the reducing agent and PVP is employed as the surfactant. In case of core-shell nanowires D-glucose and EG have been utilized as the carbonizing and reducing agent. Hence, we believe that this discovery of formation of new morphologies of 1D nanostructures of Ag_2Te could promote further advances and potential applications.

2. Materials and Methods

2.1. Synthesis of Zigzag Ag_2Te Nanowires. For the zigzag Ag_2Te nanostructures the materials used include Na_2TeO_3 (98%), AgNO_3 (99.8%), polyvinylpyrrolidone (M.W. 58, 99%), and $\text{N}_2\text{H}_4 \cdot \text{H}_2\text{O}$ (85%). All of these reagents were directly used in the experiment without any further purification. The synthesis process involves a simple hydrothermal route. In a typical experiment 2 mmol of AgNO_3 was dissolved in 50 mL of deionized water. After stirring for several minutes 1 mmol of Na_2TeO_3 was dissolved in the solution. Then the 0.5 g of PVP was added along with the dropwise addition of $\text{N}_2\text{H}_4 \cdot \text{H}_2\text{O}$. A mixed solution was dropped in 100 mL Teflon lined autoclave, followed by heating at 240°C for 24 hrs. After heating for predefined duration, the autoclave was allowed to cool at room temperature. The precipitates were centrifuged and washed with ethanol and distilled water several times and finally dried at 60°C for 12 hrs.

2.2. Synthesis of $\text{Ag}_2\text{Te}/\text{C}$ Nanowires. In case of $\text{Ag}_2\text{Te}/\text{C}$ core-shell nanostructures sodium tellurite (Na_2TeO_3), ethylene glycol ($\text{C}_2\text{H}_6\text{O}_2$), silver nitrate (AgNO_3), and D-glucose ($\text{C}_6\text{H}_{12}\text{O}_6$) were used in typical hydrothermal synthesis process. 0.34 g of AgNO_3 and 0.22 g of Na_2TeO_3 and 0.3 g of $\text{C}_6\text{H}_{12}\text{O}_6$ were dissolved in 10 mL of deionized water. Then 20 mL of ethylene glycol was added and stirred continuously. The final solution was shifted into a 100 mL Teflon lined autoclave. The autoclave was maintained at 180°C for 18 hrs. After the required time the autoclave was left to cool naturally at the room temperature. Final product was centrifuged with deionized water and ethanol and was then dried at 60°C for 12 hrs.

The size and the morphology of the prepared Ag_2Te nanostructures were characterized using scanning electron microscopy (SEM) (Hitachi S-4800), provided with X-ray energy dispersive spectrum analysis (EDS). The crystalline structure was characterized by using the TEM and high resolution TEM (HRTEM) (Tecnai G2 F20 U-TWIN field emission).

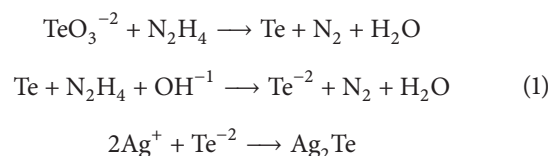
3. Result and Discussion

Ag_2Te Zigzag Nanostructures. The first synthesis process which involves the production of silver telluride zigzag nanostructures was examined with the help of SEM reported

in Figure 1(a). Numerous long wiggly nanowires of diameter 50–60 nm and typical length of several tens of nanometers are formed. A detailed investigation was carried out using TEM and HRTEM. Figure 1(b) shows a distinctive low magnification TEM image of the zigzag nanostructure with the length of several micrometers. The inset of Figure 1(b) expresses the edge morphology of a typical zigzag nanowire.

EDS analysis (Figure 1(c)) generated with an electron nanoprobe is used to check the composition of nanowires. Spectrum shows that the product consists of Ag and Te elements at an atomic ratio close to the silver telluride stoichiometry, indicating the formation of Ag_2Te nanowires. The high resolution TEM and FFT images of representative nanowire are presented in Figure 2. The lattice fringes with 0.160 nm and 0.185 nm separations are normal for the (−501) and (004) plane d-spacing in monoclinic silver telluride structure. FFT pattern analysis demonstrates that the nanostructure exhibits the polycrystalline nature due to the ring pattern. The great change in volume can produce a rapid increment in stress in all directions, which leads to the multicrystalline nature.

These experimental results and previous reports [5, 7, 8] manifest that initially Te cluster form was obtained by the reduction of Na_2TeO_3 in the presence of N_2H_4 . Chemical reactions for this possible hydrothermal mechanism for the formation of silver telluride zigzag nanowires are as follows:



Since the shape of nanocrystals in synthesis relies on the surface energies of different facets that decrease when passivated by the capping agent, the affinity of the molecules of this agent is an essential parameter in finding out the nanostructure shape. Hence, in this whole process the most important role is of water soluble surfactant or stabilizing agent PVP. Its molecules are successfully employed as the structure directing agent for the growth of the zigzag morphology. Thus, we can speculate that existence of PVP in the reaction system has an effective influence on the crystal growth behaviour. The previous precursory researches have proposed that atoms on the different crystallographic facets have different interaction strength with a polymeric capping agent, leading to the anisotropic growth of a solid material [9–12]. Hence, the more plausible synthesis route is uninterrupted anisotropic growth along with the anisotropic surface passivation by the weak surfactant molecules resulting in the saw tooth-like surface along the growth axis.

$\text{Ag}_2\text{Te}/\text{C}$ Core-Shell Structure. A general overview of SEM picture shown in Figure 3(a) represents that the product obtained after the hydrothermal process at 180°C for 18 hrs is composed of nanowires ca. 100 nm and hundreds of micrometers in length.

In the high resolution TEM image (Figure 3(b)) there is an observable contrast between the inner core and external shell which suggests the core-shell structure. The heavy

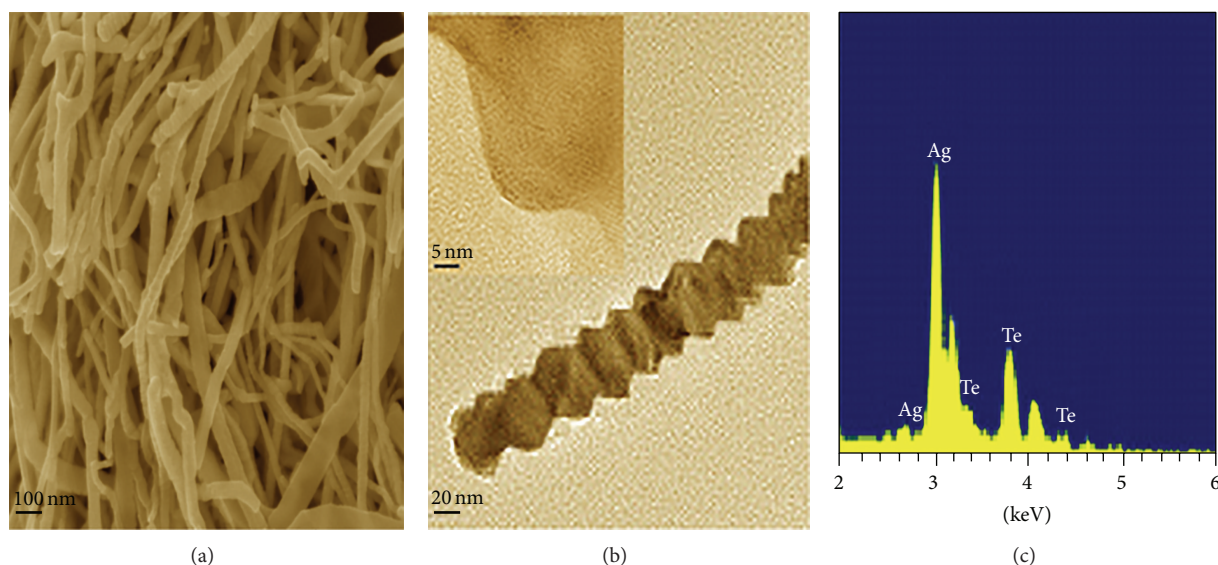


FIGURE 1: (a-b) The SEM and TEM images of fully grown zigzag Ag_2Te /nanowires; inset of (b) shows the morphology of the edge of the nanowire. (c) EDS spectrum of zigzag silver telluride nanowires.

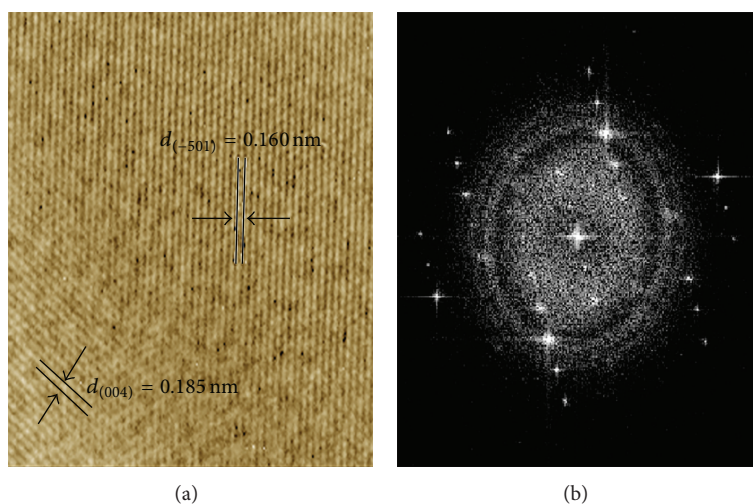


FIGURE 2: (a-b) The HRTEM image of a representative zigzag nanowire and its corresponding FFT ED pattern.

carbon coating has a consistent thickness of ca. 75 nm over the complete surface of inner silver telluride nanowire including the outer end also. Final, the EDS analysis shown in Figure 3(c) indicates strong Ag, Te, and C peaks, while the Cu peak originates from the supporting TEM grid. The amorphous carbon shell in completely grown nanostructure covering the edge can be clearly seen in Figure 4(a). This outer sheath effectively protects the inner metal telluride nanowires against attack from moisture and oxygen. The lattice spacing in HRTEM image of the inner core in Figure 4(b) is estimated to be 1.77 nm, which lies for (142) plane for monoclinic silver telluride.

The formation of the core-shell nanostructures continues under hydrothermal conditions which is greater than the normal glycosidation temperature and extends to aromatization and carbonization process [13]. This is in fact the

simplified view as there are a number of various chemical reactions of glucose which can occur under hydrothermal conditions in the sealed autoclave. In this synthesis process, reduction and carbonization route is followed by using the Na_2TeO_3 , AgNO_3 , and the glucose as Te, Ag, and C sources, respectively. Ethylene glycol (EG) used here acts as reducing agent and provides the free cations Ag^{+2} and anions TeO_3^{-2} in the solution, and further reduction of TeO_3^{-2} to the elemental tellurium takes place very rapidly [14].

The reports [15–18] predict that in the hydrothermal process the nanowires grow first, and the carbon shell occurs as the last step. Thus, as the process continues, glucose in the system carbonises to amorphous carbon and an amorphous carbon coats on telluride nanowires surface and finally results in the formation of silver telluride core-shell nanostructure. Figure 5 presents the schematic view of the reaction sequence

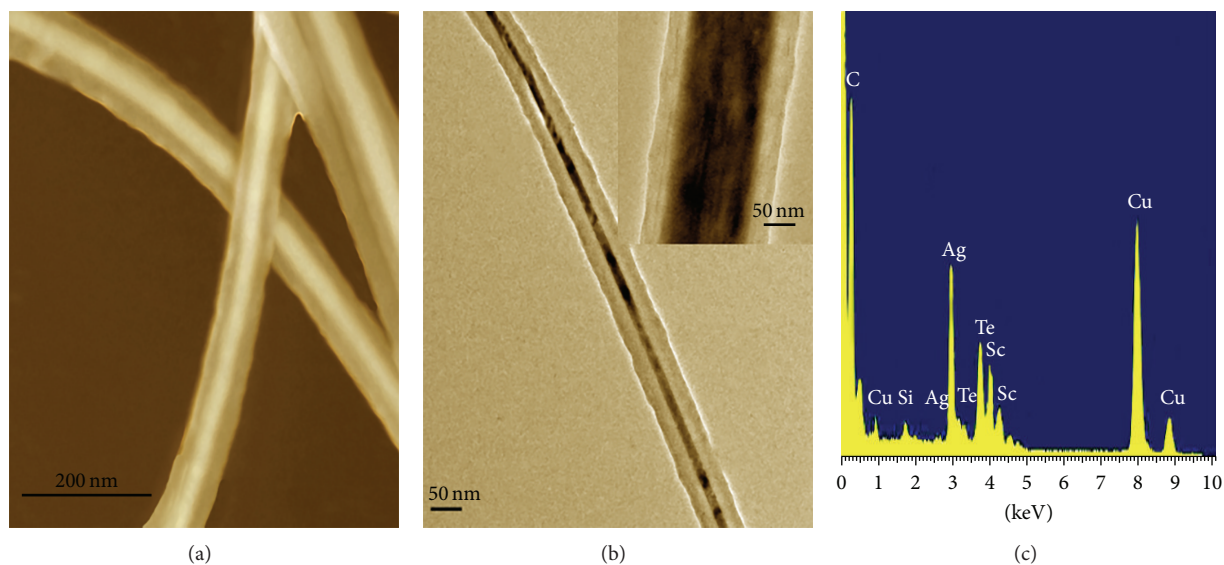


FIGURE 3: Magnified SEM and TEM images obtained from the presence of glucose at 180°C for 18 hrs. (a) A magnified SEM image of the nanowires. (b) and inset are the TEM images of the Carbon coated nanowires. (c) EDS spectrum of $\text{Ag}_2\text{Te}/\text{C}$ nanowires.

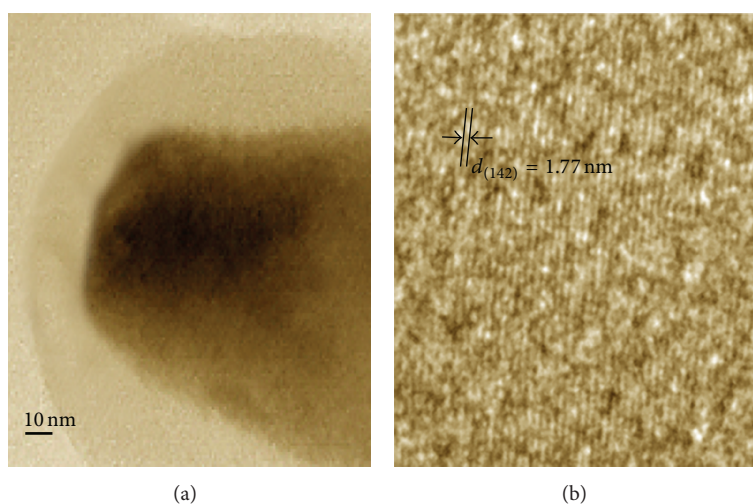


FIGURE 4: (a) TEM image of the edge of the fully grown $\text{Ag}_2\text{Te}/\text{C}$ core-shell nanowires. (b) HRTEM image of the core of the nanowire.

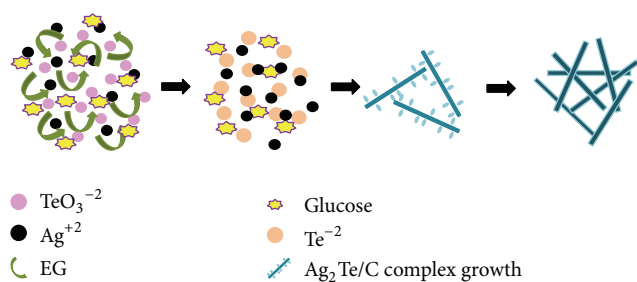


FIGURE 5: Schematic illustration of formation process of $\text{Ag}_2\text{Te}/\text{C}$ nanowires.

of the growth of $\text{Ag}_2\text{Te}/\text{C}$ nanowires. Briefly sodium tellurite and silver nitrate (precursors) dissolved in water are

converted to tellurite TeO_3^{-2} and Ag^{+2} ions in the presence of EG. In step (ii) the tellurite ions are rapidly converted to Te^{-2} . It should be noted that the glucose does not react in these reaction processes. When the temperature of the system increases the polymerization and carbonization reactions of glucose will take place, which finally produces the carbonaceous layer on the silver telluride nanowires [15].

4. Conclusion

In summary, surfactant and carbonizing agent assisted morphology is presented for the silver telluride-based nanostructures. Unconventional zigzag silver telluride nanowires and silver telluride coated with carbon core-shell nanowires were synthesized via simple hydrothermal route. SEM, TEM, and EDS have been used to study the morphology and

composition. Unusual silver telluride nanowires here report the sawtooth-like zigzag nanowires in the presence of PVP. A growth model depicting the growth of core-shell nanowires via reduction-carbonization route is proposed. These unique structural characteristics of both morphologies can be evaluated by dispersing them in ethanol solution to excel their properties in viewpoint of applications in optoelectronic devices.

Conflict of Interests

The authors declare that there is no conflict of interests regarding the publication of this paper.

Acknowledgments

The work was supported by the National Natural Science Foundation of China (61275201), the Program for New Century Excellent Talents in University of Ministry of Education of China (Grant no. NCET-10-0261), the Fund of State Key Laboratory of Information Photonics and Optical Communications (Beijing University of Posts and Telecommunications), China, and the Open Program of State Key Lab on integrated Optoelectronics, China.

References

- [1] S. Mathur and S. Barth, "Molecule-based chemical vapor growth of aligned SnO_2 nanowires and branched $\text{SnO}_2/\text{V}_2\text{O}_5$ heterostructures," *Small*, vol. 3, no. 12, pp. 2070–2075, 2007.
- [2] J. Zhan, Y. Bando, J. Hu, F. Xu, and D. Golberg, "Unconventional gallium oxide nanowires," *Small*, vol. 1, no. 8–9, pp. 883–888, 2005.
- [3] H. Peng, S. Meister, C. K. Chan, X. F. Zhang, and Y. Cui, "Morphology control of layer-structured gallium selenide nanowires," *Nano Letters*, vol. 7, no. 1, pp. 199–203, 2007.
- [4] P. Zuo, S. Zhang, B. Jin, Y. Tian, and J. Yang, "Rapid synthesis and electrochemical property of Ag_2Te nanorods," *Journal of Physical Chemistry C*, vol. 112, no. 38, pp. 14825–14829, 2008.
- [5] A. Qin, Y. Fang, P. Tao, J. Zhang, and C. Su, "Silver telluride nanotubes prepared by the hydrothermal method," *Inorganic Chemistry*, vol. 46, no. 18, pp. 7403–7409, 2007.
- [6] A. K. Samal and T. Pradeep, "Room-temperature chemical synthesis of silver telluride nanowires," *Journal of Physical Chemistry C*, vol. 113, no. 31, pp. 13539–13544, 2009.
- [7] N. Li, S. Zhou, S. Lou, and Y. Wang, "Electrical properties of individual Ag_2Te nanowires synthesized by a facile hydrothermal approach," *Materials Letters*, vol. 81, pp. 212–214, 2012.
- [8] G. Li, X. Tang, S. Zhou, N. Li, and X. Yuan, "Morphological evolution, growth mechanism, and magneto-transport properties of silver telluride one-dimensional nanostructures," *Nanoscale Research Letters*, vol. 8, article 356, 2013.
- [9] X. Peng, "Mechanisms for the shape-control and shape-evolution of colloidal semiconductor nanocrystals," *Advanced Materials*, vol. 15, no. 5, pp. 459–463, 2003.
- [10] Y. Sun, Y. Yin, and Y. Xia, "Uniform silver nanowires synthesis by reducing AgNO_3 with ethylene glycol in the presence of seeds and Poly(Vinyl Pyrrolidone)," *Chemistry of Materials*, vol. 14, no. 11, pp. 4736–4745, 2002.
- [11] Y. Sun, B. Gates, B. Mayers, and Y. Xia, "Crystalline silver nanowires by soft solution processing," *Nano Letters*, vol. 2, no. 2, pp. 165–168, 2002.
- [12] T. S. Ahmadi, Z. L. Wang, T. C. Green, A. Henglein, and M. A. El-Sayed, "Shape-controlled synthesis of colloidal platinum nanoparticles," *Science*, vol. 272, no. 5270, pp. 1924–1926, 1996.
- [13] G. S. Cao, Y. G. Liu, W. W. Yang, C. Tan, H. Li, and X. J. Zhang, "Synthesis and chemical etching of Te/C nanocables," *Bulletin of Materials Science*, vol. 34, no. 6, pp. 1185–1188, 2011.
- [14] K. Sridharan, M. S. Ollakkan, R. Philip, and T. J. Park, "Non-hydrothermal synthesis and optical limiting properties of one-dimensional Se/C , Te/C and Se-Te/C core-shell nanostructures," *Carbon*, vol. 63, pp. 263–273, 2013.
- [15] G. Xi, C. Wang, X. Wang, Y. Qian, and H. Xiao, "Te/Carbon and Se/Carbon nanocables: size-controlled in situ hydrothermal synthesis and applications in preparing metal M/Carbon nanocables ($M = \text{tellurides and selenides}$)," *The Journal of Physical Chemistry C*, vol. 112, pp. 965–971, 2008.
- [16] H. S. Qian, S. H. Yu, S. H. Luo, J. Y. Gong, L. F. Fei, and X. M. Liu, "Synthesis of uniform Te carbon-rich composite nanocables with photoluminescence properties and carbonaceous nanofibers by the hydrothermal carbonization of glucose," *Chemistry of Materials*, vol. 18, no. 8, pp. 2102–2108, 2006.
- [17] X. C. Song, Y. Zhao, Y. F. Zheng, E. Yang, W. Q. Chen, and Y. Q. Fang, "Fabrication of Se/C coaxial nanocables through a novel solution process," *Journal of Physical Chemistry C*, vol. 112, no. 14, pp. 5352–5355, 2008.
- [18] X. C. Song, Y. Zhao, E. Yang, Y. F. Zheng, L. Z. Chen, and F. M. Fu, "Fabrication and characterization of Te/C nanocables and carbonaceous nanotubes," *Crystal Growth & Design*, vol. 9, no. 1, pp. 344–347, 2008.

Research Article

Void Structures in Regularly Patterned ZnO Nanorods Grown with the Hydrothermal Method

Yu-Feng Yao, Chen-Hung Shen, Wei-Fang Chen, Pei-Ying Shih, Wang-Hsien Chou, Chia-Ying Su, Horng-Shyang Chen, Che-Hao Liao, Wen-Ming Chang, Yean-Woei Kiang, and C. C. Yang

Institute of Photonics and Optoelectronics and Department of Electrical Engineering, National Taiwan University, 1 Roosevelt Road, Section 4, Taipei 10617, Taiwan

Correspondence should be addressed to C. C. Yang; ccy@cc.ee.ntu.edu.tw

Received 14 December 2013; Accepted 14 February 2014; Published 19 March 2014

Academic Editor: Wen Lei

Copyright © 2014 Yu-Feng Yao et al. This is an open access article distributed under the Creative Commons Attribution License, which permits unrestricted use, distribution, and reproduction in any medium, provided the original work is properly cited.

The void structures and related optical properties after thermal annealing with ambient oxygen in regularly patterned ZnO nanorod (NR) arrays grown with the hydrothermal method are studied. In increasing the thermal annealing temperature, void distribution starts from the bottom and extends to the top of an NR in the vertical (*c*-axis) growth region. When the annealing temperature is higher than 400°C, void distribution spreads into the lateral (*m*-axis) growth region. Photoluminescence measurement shows that the ZnO band-edge emission, in contrast to defect emission in the yellow-red range, is the strongest under the *n*-ZnO NR process conditions of 0.003 M in Ga-doping concentration and 300°C in thermal annealing temperature with ambient oxygen. Energy dispersive X-ray spectroscopy data indicate that the concentration of hydroxyl groups in the vertical growth region is significantly higher than that in the lateral growth region. During thermal annealing, hydroxyl groups are desorbed from the NR leaving anion vacancies for reacting with cation vacancies to form voids.

1. Introduction

Because of its large band gap of 3.36 eV and high exciton binding energy of ~60 meV, ZnO nanostructures have attracted much research attention for nanodevice applications, including light-emitting devices [1], solar cells [2], power generators [3], and others [4]. ZnO nanostructures, such as nanorods (NRs) [5], nanowires [6], nanotubes [7], and nanowalls [7], have been widely investigated in the past several years due to their superior electrical and optical properties, when compared with a planar structure. In the device applications of ZnO NRs, it is important not only to grow ZnO NRs with a high degree of regularity and uniformity in terms of their height and cross-sectional size, but also to accurately control their positions. Good controls of NR position and shape can improve the performances of the fabricated electronics and optoelectronics devices [8, 9]. A few vapor-phase methods have been used for the growth of ZnO NRs, including metalorganic chemical vapor deposition (MOCVD) [10], pulsed laser deposition [11], and radiofrequency magnetron

sputtering [12]. A ZnO NR formed via the hydrothermal method has attracted attention because of its advantages of fast, large-scale, low-cost, and low-temperature (<100°C) growth. Selective-area growth (SAG) on a patterned mask has been proved to be an effective method for localizing the growth of ZnO nanostructures. Various lithography methods for SAG patterning have been reported, including nanoimprint [13], interference [14], electron-beam writing [15], and nanosphere coating [16]. For a high-throughput, low-cost, and large-area fabrication, nanoimprint lithography is a preferred choice.

Although the growth of ZnO NRs with the hydrothermal method has the aforementioned advantages, it may result in a high defect density due to the low growth temperature. In particular, it has been reported that voids could be formed in a ZnO structure grown with the hydrothermal method [17–19]. However, although the existence of voids in a ZnO film [17], on a ZnO NR surface [18], or inside a ZnO NR after thermal annealing has been mentioned or briefly discussed [19], so far no detailed study on the void distribution inside a ZnO NR

and its formation condition and mechanism was reported, particularly in a regularly patterned ZnO NR array grown with the hydrothermal method. In this paper, we first demonstrate the growth of regularly patterned ZnO NR arrays on GaN template with the hydrothermal method based on the nanoimprint lithography technique. The optimum conditions of growth solution concentration, growth temperature, and growth duration are identified. Then, with the measurements of scanning electron microscopy (SEM), backscattering electron microscopy (BSEM), and transmission electron microscopy (TEM), including the observations of high-angle annular dark-field (HAADF) image and energy dispersive X-ray (EDX) spectrum, the void distributions and their formation mechanisms under various thermal annealing and Ga-doping conditions are investigated. Also, the emission properties under various conditions are explored with room-temperature photoluminescence (PL) measurement.

In Section 2 of this paper, the fabrication procedures and growth conditions of regularly patterned ZnO NR arrays are reported. The void microstructures under different thermal annealing and Ga-doping conditions are discussed in Section 3. Then, the optical characterization results are shown in Section 4. Discussions regarding the formation of voids are given in Section 5. Finally, conclusions are drawn in Section 6.

2. Growth of Regularly Patterned ZnO Nanorod Arrays

The ZnO NR arrays are grown on a 2 μm undoped GaN template with a patterned Si_3N_4 mask layer of 40 nm in thickness, which is deposited with plasma enhanced chemical vapor deposition. The GaN layer is grown with MOCVD at 1000°C on a *c*-plane sapphire substrate. The nanoimprint lithography technique is used for patterning the Si_3N_4 mask with a triangular arrangement of circular holes of 350 nm in hole diameter and 1453 nm in pitch. Figure 1(a) shows the plan-view SEM image (with a JEOL JSM-7001F system at 15 kV in electron acceleration voltage) of the patterned template used for ZnO NR growth. In the hydrothermal growth process, after cleaning such a template is placed upside down in the growth solution for avoiding the accumulation of precipitates in the gaps between NRs. For undoped ZnO NR growth, the aqueous solution for the hydrothermal reaction consists of equal-molar zinc nitrate hexahydrate and hexamethylenetetramine of controlled concentrations. Before use, the chemicals are well mixed in the solution and the precipitates are filtered. The template is immersed in the solution 10 min after the solution is heated to the designated growth temperature. Then, the sealed beaker containing the growth solution and the template is kept at the designated growth temperature for the designated growth duration.

Figures 1(b)–1(d) show the 30° tilted SEM images of the growth results on the template with the growth durations of 10, 30, and 180 min, respectively, when the concentration of the growth solution is 0.08 M and the growth temperature is 80°C. As shown in Figure 1(b), multiple ZnO nucleation clusters are formed in each hole on the patterned mask after

the growth duration of 10 min. Each of those nucleation clusters can extend its length along the *c*-axis to form a small NR, as shown in Figure 1(c). As the growth duration becomes longer, those small ZnO NRs in a hole can merge into a large hexagonal NR with the cross-sectional size larger than the hole diameter, as shown in Figure 1(d). The larger cross-sectional size of the grown NRs implies that both the vertical growth (along the *c*-axis) and lateral growth (along the *m*-axis) of ZnO occur during the formation of an NR. Here, one can see that the top faces of the NRs are quite flat. The cross-sectional size (the distance between two parallel sides of the hexagonal shape) is about 850 nm. The height of this ZnO NR array is around 2 μm . Figure 1(e) shows a larger-scale tilted SEM image of the same sample illustrating the uniformity of the ZnO NR array. It is found that the ZnO NR growths with higher growth solution concentrations (say, 0.1 M), higher growth temperatures (say, 95°C), or longer growth durations (say, 300 min) lead to coalesced growth of NRs to form thin films. In the hydrothermal reaction study, we also consider the growth of *n*-ZnO NR arrays by doping ZnO with Ga through the addition of gallium nitrate hydrate to the growth solution of various concentrations. Figure 1(f) shows the tilted SEM image of a Ga-doped ZnO NR array under the same growth conditions as those for Figures 1(b)–1(e). The Ga doping is implemented by adding gallium nitrate hydrate of a designated concentration to the growth solution. The used concentration of gallium nitrate hydrate for growing the sample shown in Figure 1(f) is 0.003 M. The cross-sectional size of the Ga-doped ZnO NRs is smaller than that of the undoped NRs. The electron concentration of the grown *n*-ZnO (a thin film growth of 300 min in growth duration) under the same growth conditions as those for the sample in Figure 1(f) is measured to give $2.57 \times 10^{19} \text{ cm}^{-3}$. Since many undoped ZnO NR array samples in the following discussions are grown under the same growth condition as that for the sample shown in Figure 1(d) (0.08 M in growth solution concentration, 80°C in growth temperature, and 180 min in growth duration), this set of growth parameters will be referred to as the standard growth condition for undoped ZnO NR array. By adding gallium nitrate hydrate of 0.003 M, the set of growth parameters will be referred to as the standard growth condition for Ga-doped ZnO NR array.

As shown in Figure 1(c), an NR is formed through the growth of multiple small rod structures first and then their mergence. Figures 2(a) and 2(b) show a cross-sectional TEM image of an NR and the close-up image around the bottom of the NR, respectively, based on the standard growth condition. The TEM specimens are prepared through the sample ablation by a focused ion beam. The TEM investigation is performed using a Philips/Tecni F30 field-emission electron microscope with an accelerating voltage of 300 kV and a probe forming lens of $C_s = 1.2 \text{ mm}$. In Figure 2(b), the dark line pattern dividing different domains indicates the merging process of the multiple nucleation clusters. During this process, the domain boundaries may evolve into threading dislocations as growth continues. In Figure 2(b), two dislocations are formed as indicated by the white arrows. As shown in Figure 2(a), one of them propagates to the top of the NR. The other extends toward

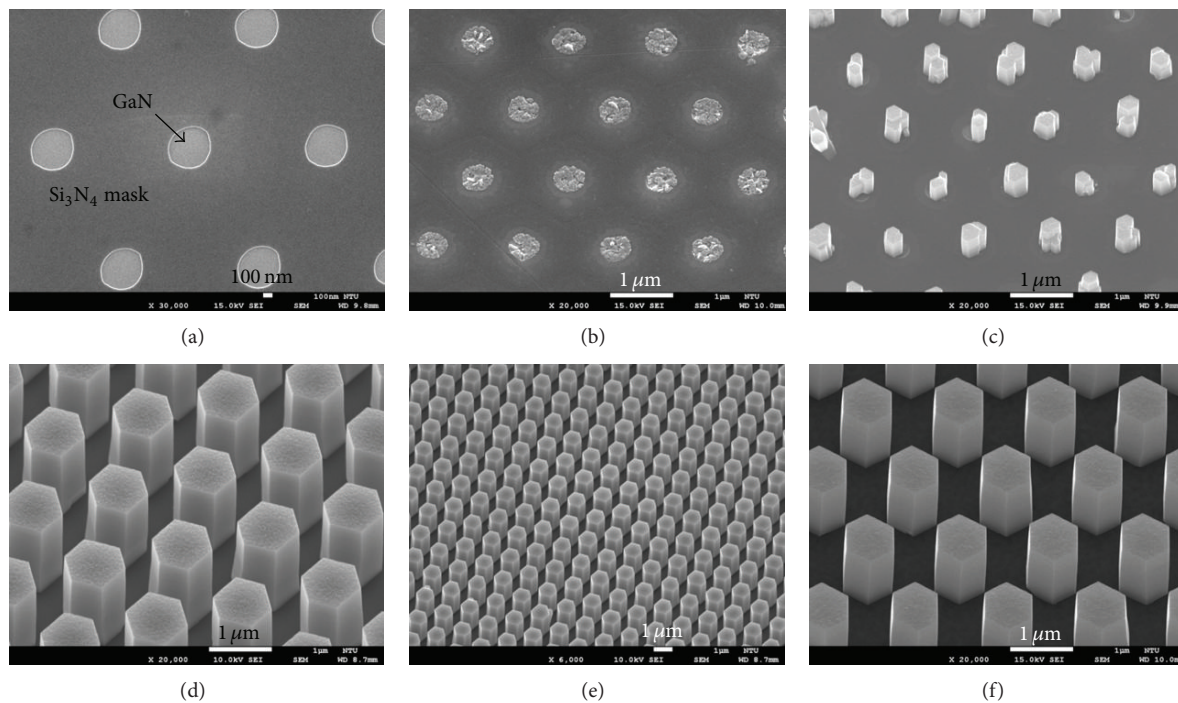


FIGURE 1: (a) Plan-view SEM image of a patterned template for ZnO NR growth. (b)–(d) 30° tilted SEM images of the growth results on the template with the growth durations of 10, 30, and 180 min, respectively, when the concentration of the growth solution is 0.08 M and the growth temperature is 80°C. (e) Larger-scale tilted SEM image of the same sample illustrating the uniformity of the ZnO NR array. (f) Tilted SEM image of a Ga-doped ZnO NR array sample under the same growth conditions as those in parts (b)–(e) and 0.003 M in Ga-doping concentration.

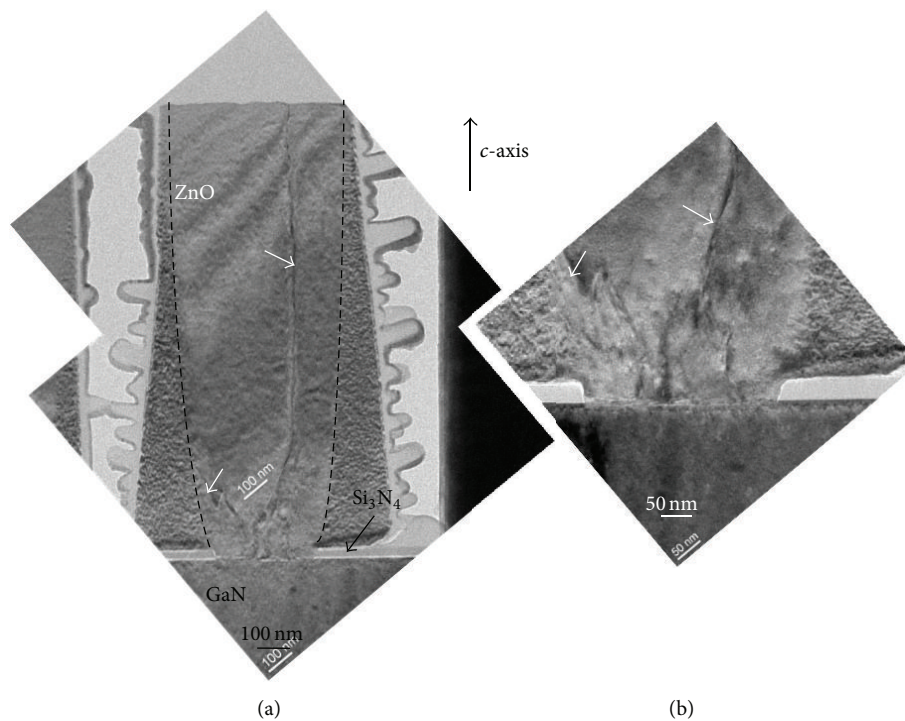


FIGURE 2: (a) and (b) Cross-sectional TEM image of an NR and the close-up image around the bottom of the NR, respectively. The arrows show the two dislocations. The two dashed curves divide the regions of the vertical and lateral growth regions.

the upper-left direction. In this image, this dislocation stops at the boundary between two regions of different levels of surface roughness. As approximately divided by the two dashed curves in Figure 2(a), the relatively smoother and rougher regions correspond to the portions of vertical (along the c -axis) and lateral (along the m -axis) growths, as to be further discussed later. The left dislocation in Figure 2(a) can be bended in the lateral growth region such that it does not propagate toward the top of the NR.

3. Void Formation in ZnO Nanorods

Thermal annealing can improve the crystal and optical qualities of the grown ZnO NRs. Figures 3(b)–3(e) show the cross-sectional TEM images of undoped ZnO NRs after thermal annealing with ambient oxygen for 60 min at 200, 300, 400, and 500°C, respectively. For comparison, the TEM image of an as-grown sample is also shown in Figure 3(a). The undoped ZnO NRs are grown under the standard growth condition. In the as-grown sample, no void structure can be seen in the ZnO NR. Voids are formed after thermal annealing. At 200°C in annealing temperature, the voids are small such that the image contrast is weak. A few voids are indicated by the arrows. Here, the voids are distributed around the lower central portion of the NR. As the annealing temperature increases, the void size and density become larger and its distribution extends upward to cover a larger area. With the annealing temperatures at 300 and 400°C, the voids are distributed only in the region of vertical growth. In Figures 3(c) and 3(d), the dashed curves again indicate roughly the boundaries between the regions of vertical and lateral growths. When the annealing temperature is 500°C, the void distribution reaches the top of the NR and extends into the region of lateral growth. As shown in Figures 3(d) and 3(e), the void size can be as large as 100 nm.

The scenarios of void formation in Ga-doped ZnO NRs are quite different. Figures 4(a)–4(d) show the cross-sectional TEM images of an as-grown Ga-doped ZnO NR, and Ga-doped ZnO NRs thermally annealed at 200, 300, and 400°C, respectively, with ambient oxygen for 60 min. The Ga-doped ZnO NRs are grown under the standard condition. Here, different from the case of undoped ZnO NR, essentially void is not formed under the annealing condition of 200°C in temperature. Voids are clearly seen when the annealing temperature becomes higher, as shown in Figures 4(c) and 4(d). Therefore, voids can be formed in a Ga-doped ZnO NR when it is annealed at a higher temperature, when compared with an undoped ZnO NR. To understand the crystal microstructures around voids, in Figures 5(b) and 5(c), we show two atomic-scale TEM images in the two regions across the void boundaries marked with the rectangles in Figure 5(a) in a Ga-doped ZnO NR thermally annealed at 400°C with ambient oxygen for 60 min (the same as the sample shown in Figure 4(d)). Figures 5(d) and 5(e) show the Fourier-transform patterns of the whole TEM images in Figures 5(b) and 5(c), respectively. In Figures 5(b) and 5(c), the brighter regions correspond to the two neighboring voids around the marked areas in Figure 5(a). Here, one can see that the

lattice fringes are continuous across the void boundaries. Also, as shown in Figures 5(d) and 5(e), the corresponding Fourier-transform patterns are quite coherent. These results indicate that during void formation in the thermal annealing process, the atomic arrangement follows the structure of the neighboring ZnO crystal.

The void structures in the NRs can also be seen with the observation of BSEM. Figure 6(a) shows the SEM image of four fallen undoped ZnO NRs grown under the standard condition before thermal annealing. The SEM image of the same sample after thermal annealing at 300°C for 60 min with ambient oxygen is shown in Figure 6(b). The SEM image of the same sample after the second annealing process at 400°C for 60 min with ambient oxygen is shown in Figure 6(c). Then, The SEM image of the same sample after the third annealing process at 500°C for 60 min with ambient oxygen is shown in Figure 6(d). Here, one can see that void cannot be observed with SEM either before or after thermal annealing. However, voids can be observed with BSEM, as shown in Figures 6(f)–6(h). Figures 6(e)–6(h) show the BSEM images corresponding to the SEM images in Figures 6(a)–6(d), respectively. The dark spots in Figures 6(f)–6(h) show the void distributions under different annealing conditions. The SEM images in Figures 7(a) and 7(b) show either the bottom or top faces of a few undoped ZnO NRs after the three-stage annealing process (300, 400, and then 500°C). On a bottom face, one can see a circular protrusion, which corresponds to the ZnO portion in the patterned hole on the growth template. Figures 7(c) and 7(d) show the corresponding BSEM images of Figures 7(a) and 7(b), respectively. Here, one can see that on a bottom face, voids distribute only in the protrusion portion, that is, the portion of vertical growth. On a top face, the voids distribute in a larger circular area. This result is consistent with those in Figures 3(e) and 4(d).

4. Photoluminescence Measurement

Figure 8 shows the PL spectra of undoped ZnO NR array samples under the as-grown and the thermal annealing conditions of different ambient gases (air and oxygen). The NR array samples are grown under the standard condition. The thermal annealing conditions include 300°C in temperature and 60 min in duration. The PL measurement is excited by a HeCd laser at 325 nm with the incident power at 10 mW. In each curve of Figure 8, a narrow peak around 375 nm due to the band-edge emission of ZnO and a broad hump in the range of 470–800 nm from defect emission can be observed. The small peak around 360 nm in the spectrum with ambient air originates from the band-edge emission of the GaN template. Because the spectral portions of band-edge and defect emissions can be well separated, the ratio of their individual integrated intensities can be used for indicating the optical quality of the NR array sample. Here, one can see that the defect emission is significantly weaker under the annealing condition of ambient oxygen. The integrated PL intensity ratios of band-edge emission over defect emission are 0.05, 0.45, and 2.11 in the as-grown case, the cases of annealing with ambient air, and annealing

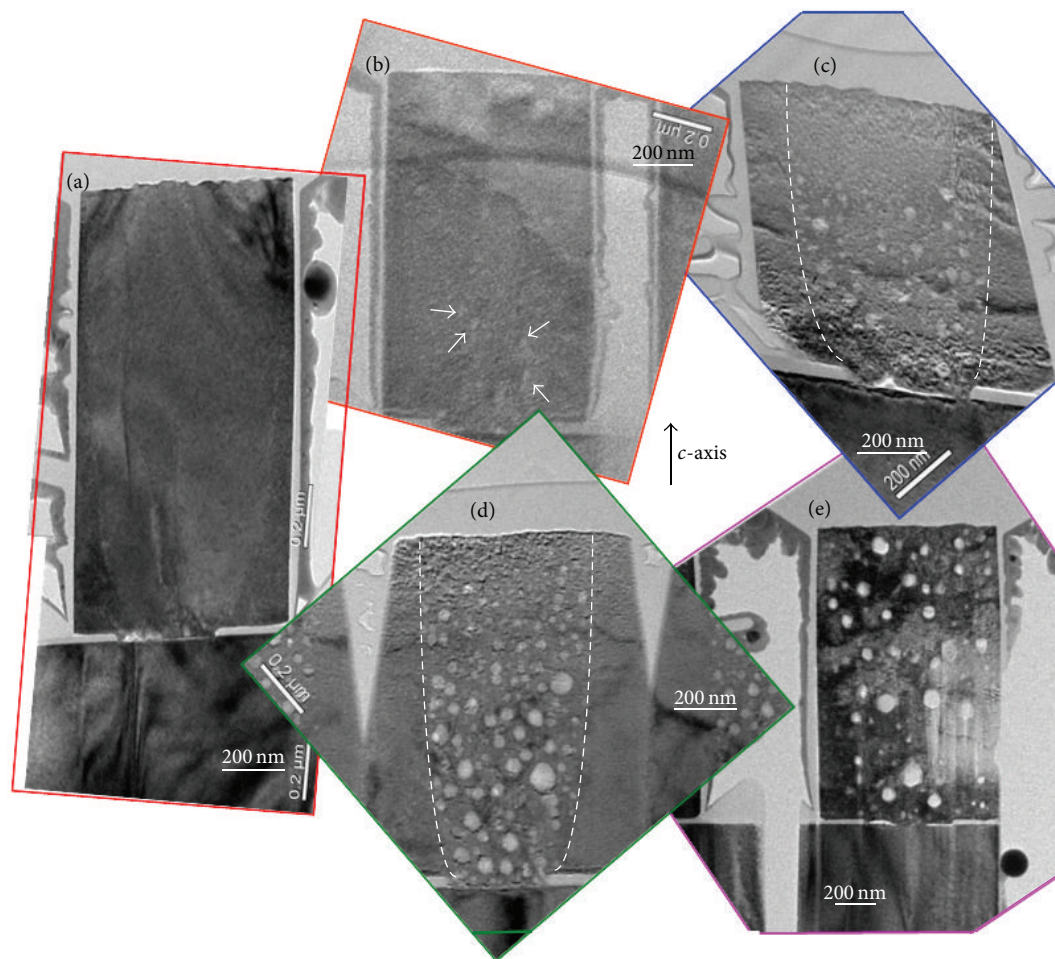


FIGURE 3: (a) Cross-sectional TEM image of an as-grown undoped ZnO NR sample. (b)–(e): Cross-sectional TEM images of undoped ZnO NRs after thermal annealing with ambient oxygen for 60 min at 200, 300, 400, and 500°C, respectively. The ZnO NRs are grown under the standard condition.

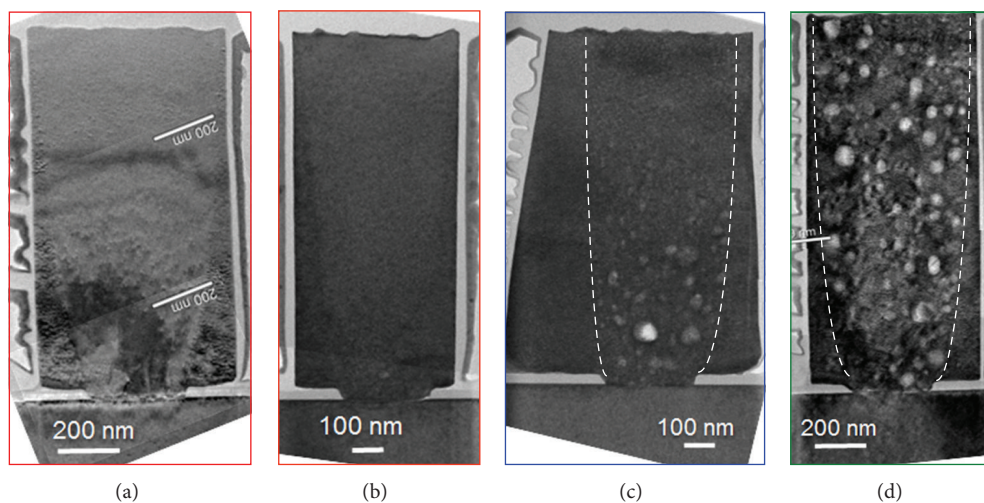


FIGURE 4: (a)–(d) Cross-sectional TEM images of an as-grown Ga-doped ZnO NR and Ga-doped ZnO NRs thermally annealed at 200, 300, and 400°C, respectively, with ambient oxygen for 60 min. The Ga-doped ZnO NRs are grown under the standard condition.

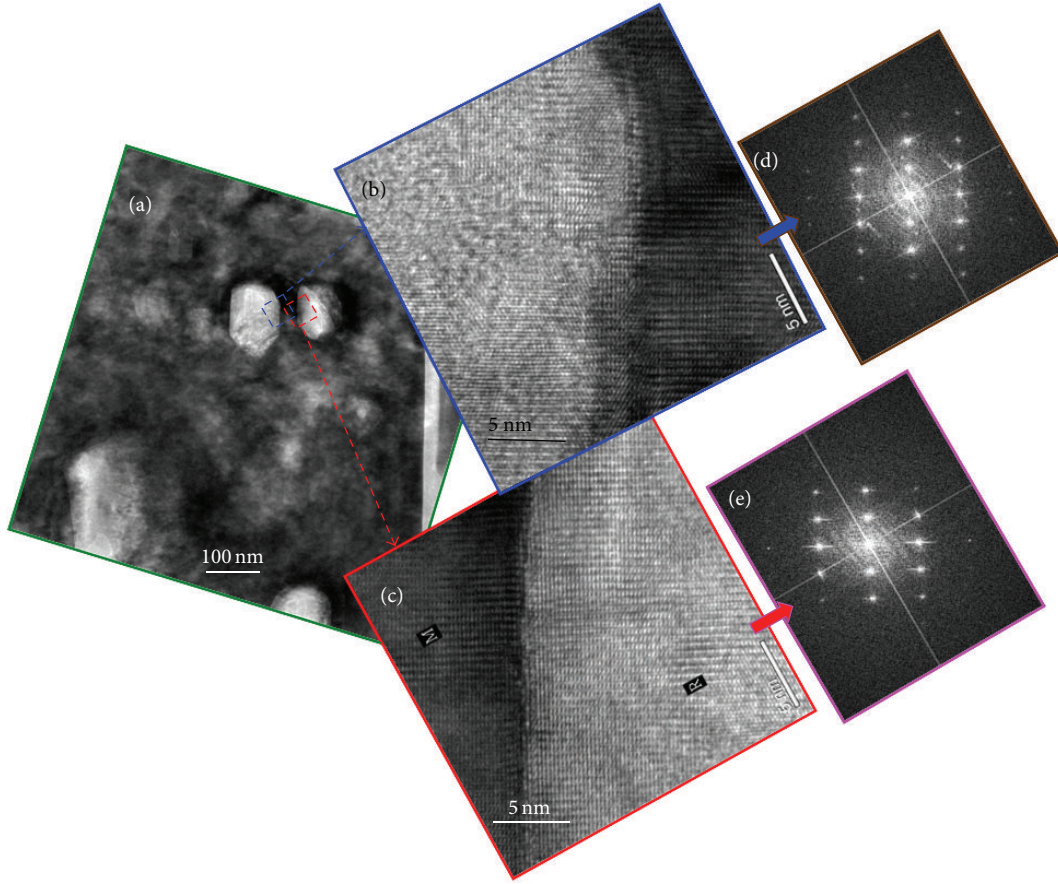


FIGURE 5: (a) Cross-sectional TEM image of a Ga-doped ZnO NR thermally annealed at 400°C with ambient oxygen for 60 min (the same as the sample shown in Figure 4(d)). (b) and (c) Atomic-scale TEM images in the regions marked with the two rectangles in part (a). (d) and (e) Fourier-transform patterns of the images in parts (b) and (c), respectively.

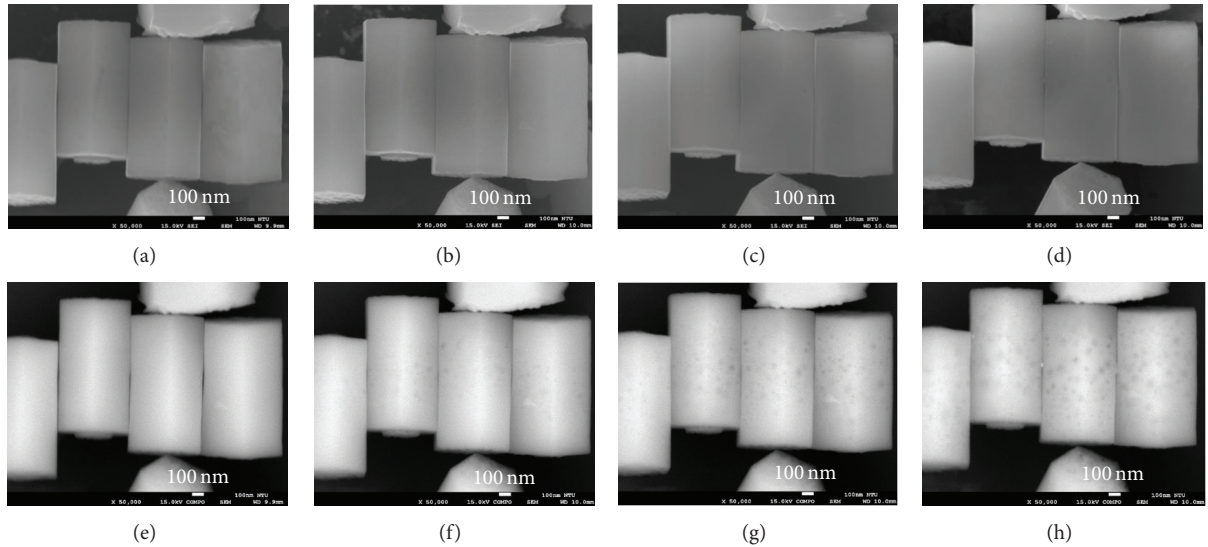


FIGURE 6: (a) SEM image of four fallen undoped ZnO NRs before thermal annealing. (b) SEM image of the sample in (a) after thermal annealing at 300°C for 60 min with ambient oxygen. (c) SEM image of the sample in (b) after the second annealing process at 400°C for 60 min with ambient oxygen. (d) SEM image of the sample in (c) after the third annealing process at 500°C for 60 min with ambient oxygen. (e)–(h) BSEM images corresponding to the SEM images in parts (a)–(d), respectively. The undoped ZnO NRs are grown under the standard condition.

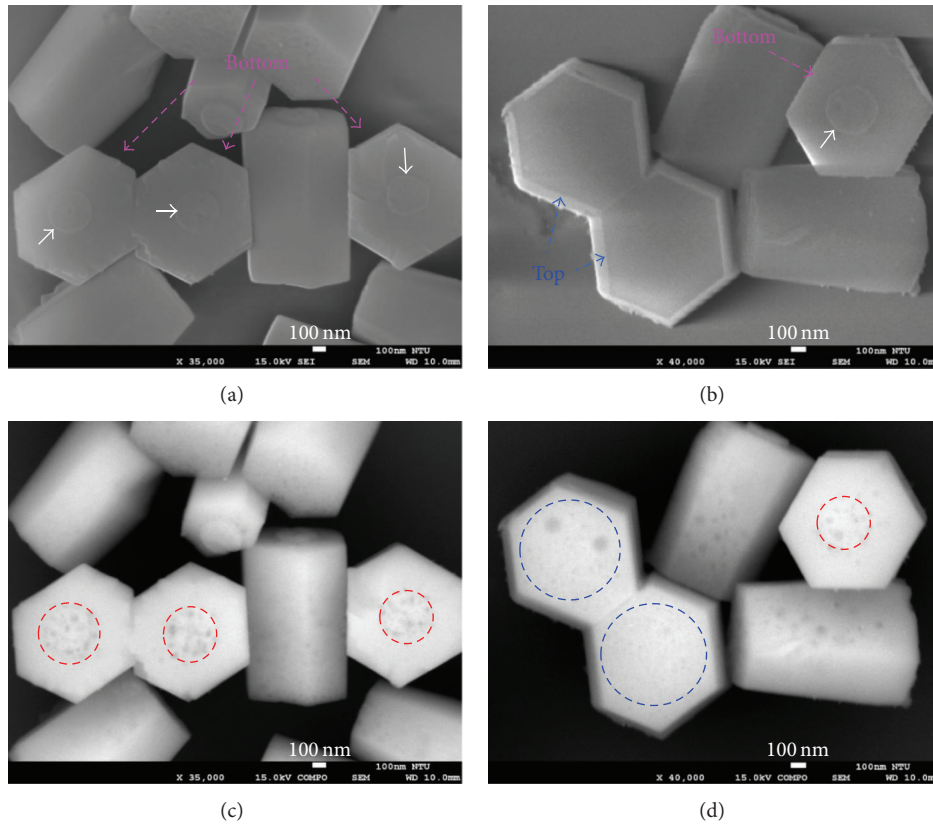


FIGURE 7: (a) and (b) SEM images of a few fallen ZnO NRs showing either their bottom or top faces after the three-stage annealing process (the same condition as the sample in Figure 6(d)). (c) and (d) The corresponding BSEM images of parts (a) and (b), respectively.

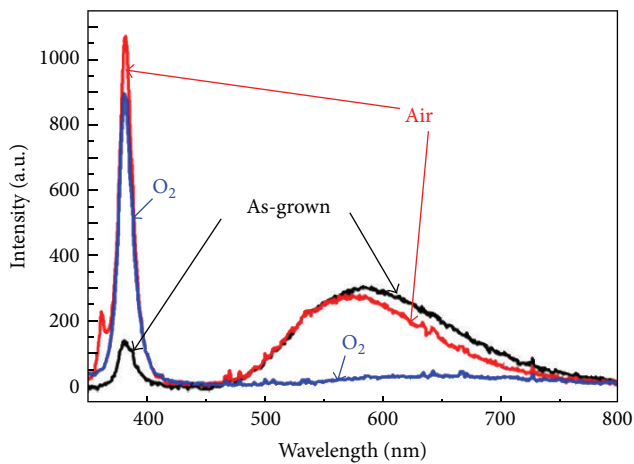


FIGURE 8: PL spectra of undoped ZnO NR array samples under the as-grown condition and the thermal annealing conditions of different ambient gases (air and oxygen). The NR array samples are grown under the standard condition. The thermal annealing conditions include 300°C in temperature and 60 min in duration.

with ambient oxygen, respectively. One can see that thermal annealing can improve the optical quality of a ZnO NR array sample, particularly when oxygen is used as the ambient gas. Therefore, oxygen was used as the ambient gas in the annealing processes leading to the results in Figures 3–7.

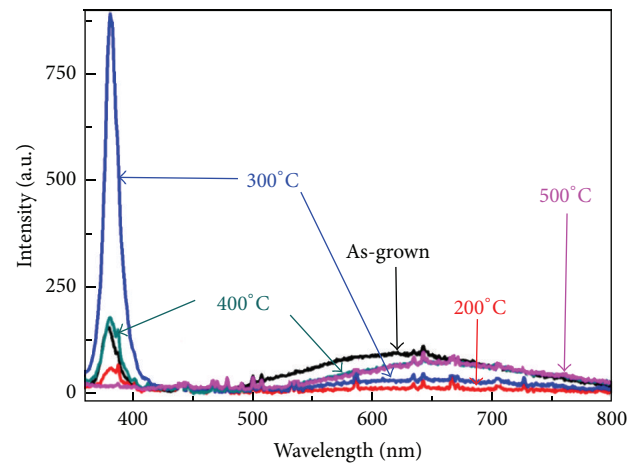


FIGURE 9: PL spectra of Ga-doped ZnO NR array samples with different thermal annealing temperatures. The Ga-doped ZnO NRs are grown under the standard condition. The annealing process is undertaken with ambient oxygen for 60 min.

Figure 9 shows the PL spectra of Ga-doped ZnO NR array samples at different thermal annealing temperatures. The result of the as-grown sample is also shown here for comparison. The Ga-doped ZnO NRs are grown under the standard condition. The annealing process is undertaken with ambient oxygen for 60 min. Here, one can see that the defect emission level decreases first and then increases as the

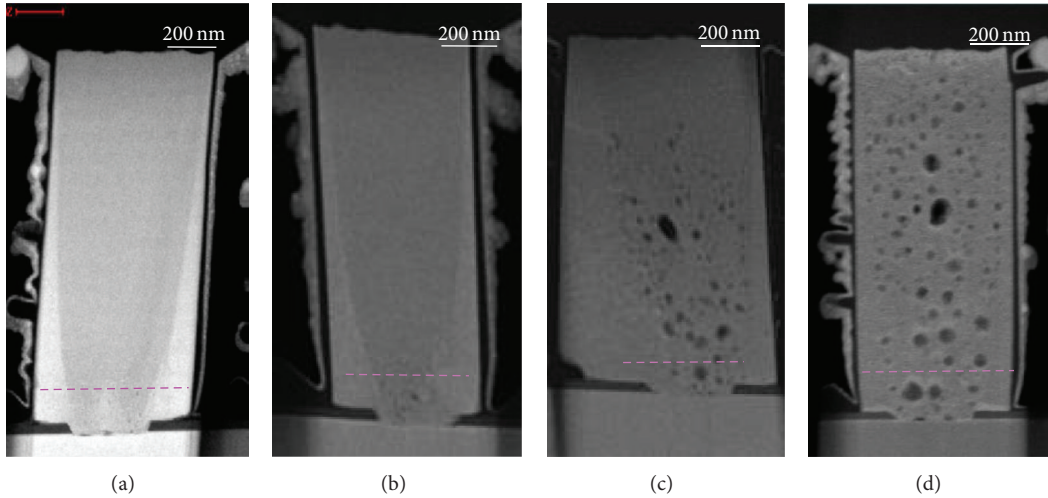


FIGURE 10: (a) HAADF image of an as-grown Ga-doped NR sample. (b)–(d) HAADF images of the Ga-doped ZnO NR samples after they are thermally annealed at 200, 300, and 400°C, respectively. The Ga-doped ZnO NRs are grown under the standard condition. The annealing process is undertaken with ambient oxygen for 60 min. In each of those images, a horizontal dashed line is drawn, along which EDX analysis is made.

TABLE 1: Ratio of integrated PL intensity of the ZnO band-edge emission over that of the defect emission with different Ga doping concentrations at different thermal annealing temperatures.

Doping concentration (M)	As-grown	200°C	300°C	400°C	500°C
0.002	0.24	0.43	1.69	0.18	0.08
0.003	0.17	0.53	2.11	0.28	0.09
0.004	0.15	0.55	0.84	0.22	0.01

annealing temperature increases from 200 to 500°C. At 400 and 500°C for thermal annealing, the spectral peak of defect emission red shifts. The ratio of integrated intensity between the band-edge and defect emissions is the largest when the annealing temperature is 300°C. Table 1 shows the integrated PL intensity ratios of various samples with different Ga-doping concentrations when they are annealed at different temperatures. The annealing is undertaken with ambient oxygen for 60 min. Here, one can see that at the annealing temperature of 300°C, we can always obtain the highest integrated intensity ratio under each doping condition. The ratio is the highest when the doping concentration is 0.003 M. Therefore, 0.003 M in gallium nitrate hydrate concentration and 300°C in annealing temperature represent the optimum conditions for forming Ga-doped ZnO NR arrays based on the hydrothermal method as far as optical property is concerned.

5. Discussions

Figures 10(b)–10(d) show the HAADF images of Ga-doped ZnO NR array samples when they are thermally annealed at 200, 300, and 400°C, respectively. For comparison, the HAADF image of the as-grown sample is also shown in Figure 10(a). The doped ZnO NRs are grown under the

standard condition. The annealing process is undertaken with ambient oxygen for 60 min. In each part of Figure 10, one can see the darker and brighter regions of vertical and lateral growths, respectively, indicating that the vertical growth region is oxygen richer, when compared with the lateral growth region, because the signal intensity in a HAADF image is proportional to average atomic number. The contrast between the vertical and lateral growth regions diminishes as the annealing temperature becomes higher. In each of those images, a horizontal dashed line is drawn, along which EDX analysis is made. The atomic % levels of O, Zn, and Ga along the dashed lines in Figures 10(a)–10(d) are shown in Figures 11(a)–11(d), respectively. It is noted that in each case, the dashed line passes the boundaries between the vertical and lateral growth regions. In each part of Figure 11, data points 1, 2, 7, and 8 (3–6) are located in the lateral (vertical) growth region. As shown in Figure 11(a), the oxygen atomic composition % is higher than that of zinc in both regions of vertical and lateral growths. The difference between the oxygen and zinc contents in the vertical growth region is significantly larger than that in the lateral growth region, indicating that the crystal in the lateral growth region is closer to the stoichiometric condition. The oxygen-rich condition in the vertical growth region is the major cause for easier formation of void. The gallium atomic % is low and quite uniform over the two growth regions. When the sample is thermally annealed, the difference between the oxygen and zinc contents becomes smaller in either the vertical or lateral growth region. The difference level decreases with increasing annealing temperature. At 400°C in annealing temperature, both atomic % levels of oxygen and zinc become close to 50%. The difference between the vertical and lateral growth regions diminishes due to desorption of excess oxygen atoms during the process of thermal annealing.

As shown in Figure 9, the defect emission level decreases at the thermal annealing temperatures of 200 and 300°C

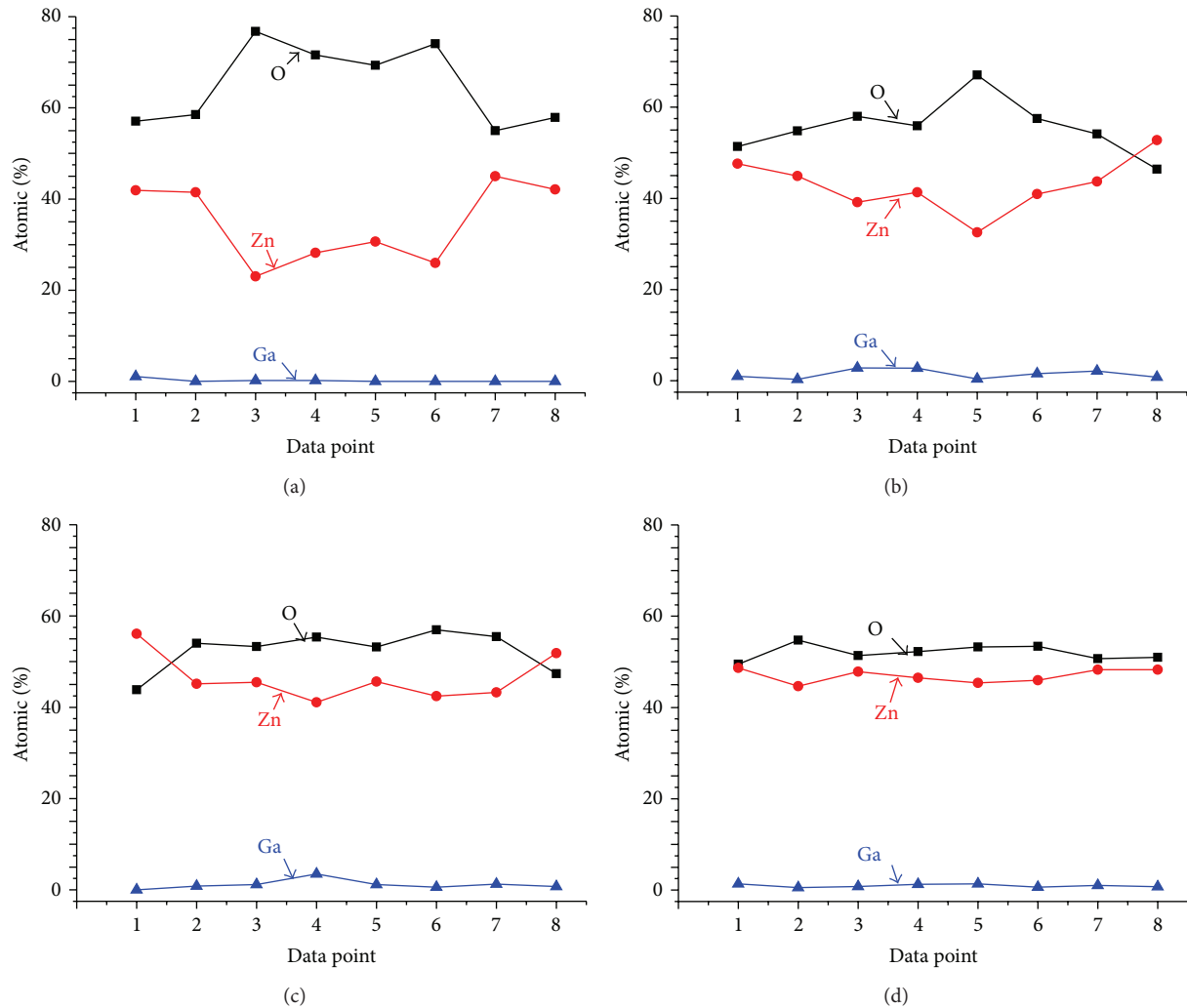


FIGURE 11: (a)–(d) Atomic % levels of O, Zn, and Ga along the dashed lines in Figures 10(a)–10(d), respectively. In each part, data points 1, 2, 7, and 8 (3–6) are located in the lateral (vertical) growth region.

and then increases as the annealing temperature is raised to 400 and 500°C. It is noted that the emission spectral peak is red shifted from ~620 to ~660 nm when the annealing temperature is increased from 200 to 500°C. The defect emission band can be split into two components, including one centered at ~590 nm (yellow emission) and the other centered at ~690 nm (red emission). The red emission in a ZnO sample grown with the hydrothermal method has been attributed to oxygen interstitials [17, 20]. The yellow emission was partly attributed to oxygen interstitials [21]. It was also ascribed to the presence of hydroxyl groups in the sample, which are commonly observed in a sample with a solution growth method [22]. The hydroxyl groups are involved in the crystallization of ZnO NRs by substituting oxygen anions at their positions [17]. During the annealing process, the hydroxyl groups gain the energy required to escape from their crystal lattice sites. The desorption rate reaches the peak level at 150°C in annealing temperature [22]. Hence, the reduction of hydroxyl groups in ZnO lattice may be responsible for the decrease of the yellow emission level

in the PL spectrum. With ambient oxygen during thermal annealing, ambient oxygen can be absorbed by the NRs while oxygen interstitials can evade from NRs at the same time. When the annealing temperature is lower than 400°C, the process of oxygen desorption may dominate such that the red emission caused by excess oxygen becomes weaker. As the annealing temperature becomes higher, the process of oxygen absorption dominates such that the red emission level becomes higher. On the other hand, during thermal annealing at a high temperature, no supply of hydroxyl groups can lead to the increase of yellow emission. It is noted that the aforementioned increase of oxygen interstitials under the conditions of 400 and 500°C in annealing temperature can occur only in a thin subsurface layer on a ZnO NR, particularly near the bottom of an NR where the supply of ambient oxygen is smaller. In this situation, the increase of oxygen interstitials near the NR top can be monitored to show the increase of red emission (and effectively the red shift of the overall defect emission spectrum) with the PL measurement under the conditions of shallow penetration (~100 nm in

depth from the NR surface) and shadowed illumination of UV excitation laser. However, in the EDX measurement with the results shown in Figure 11, the locations for acquiring the data are close to the NR bottom (see the dashed lines in Figure 10) where the increase of oxygen interstitials is insignificant such that the stoichiometric condition can be almost reached, as shown in Figure 11(d).

The formation of voids can be attributed to the desorption of hydroxyl groups during the annealing process [17]. In the ZnO crystal with hydroxyl groups, to maintain local electrical neutrality, cation vacancies must exist to neutralize the additional positive charges of hydrogen ions in the hydroxyl groups. During thermal annealing, the hydroxyl groups leave the sample in the form of water vapor and generate anion vacancies at their originally resting sites. The cation vacancies react with the anion vacancies to form vacancy pairs. The gathering of vacancy pairs forms the cores of the voids. With the thermal energy, a few small voids can merge into a larger one at a higher annealing temperature.

The speed of vertical growth is much higher than that of lateral growth in forming a ZnO NR. The higher growth speed in the vertical direction leads to poorer crystal quality with abundant defects [19]. As shown in Figures 3 and 4, void formation can be observed in the vertical growth region at lower thermal annealing temperatures, implying that the density of hydroxyl groups is higher in the vertical growth region, when compared with the lateral growth region. One of the reasons for vertical growth being more defective is the polarity along the *c*-axis owing to the hexagonal wurtzite structure of ZnO [23]. The top polar plane is more attractive to hydroxyl groups when compared with the nonpolar plane on the sidewall of a ZnO NR. The nonuniform void distribution along the *c*-axis in an NR under the thermal annealing conditions at 300 and 400°C in temperature (see Figures 3 and 4) can be attributed to the temperature gradient (decreasing temperature from the bottom to the top of an NR) in thermally annealing the NR sample. Although the desorption rate of hydroxyl groups decreases with increasing annealing temperature beyond 150°C [24], only when the annealing temperature is high enough for the void cores to grow into small voids and for the small voids to merge into large voids such that they can be observed with TEM. In Figures 3(c), 3(d), and 4(c), the void cores or small voids near the NR tops are too small to be observed.

6. Conclusions

In summary, we have investigated the void structures and related optical properties after thermal annealing with ambient oxygen in regularly patterned ZnO NR arrays grown with the hydrothermal method. In increasing the annealing temperature, based on the TEM and BSEM observations, void distribution started from the bottom and extended to the top of an NR in the vertical growth region. When the annealing temperature became higher than 400°C, void distribution spread into the lateral growth region. PL measurement showed that the ZnO band-edge emission, in contrast to defect emission in the yellow-red range, was the strongest under the *n*-ZnO NR process conditions of 0.08 M in growth

solution concentration, 0.003 M in Ga-doping concentration, 80°C in growth temperature, 180 min in growth duration, and 300°C in thermal annealing temperature with ambient oxygen for 60 min. EDX data indicated that the concentration of hydroxyl groups, which took the positions of anions in ZnO, in the vertical growth region was significantly higher than that in the lateral growth region of an NR. During thermal annealing, hydroxyl groups were desorbed from the NR leaving anion vacancies for reacting with cation vacancies to form void cores. The thermal annealing process provided energy for merging small voids into large ones.

Conflict of Interests

The authors declare that there is no conflict of interests regarding the publication of this paper.

Acknowledgment

This research was supported by National Science Council, Taiwan, The Republic of China, under the Grants of NSC 101-2120-M-002-013, NSC 101-2622-E-002-002-CC2, NSC 99-2221-E-002-123-MY3, and NSC 101-2221-E-002-153, by the Excellent Research Projects of National Taiwan University (101R890952 and 101R890951) and by US Air Force Scientific Research Office under the Ccontract of AOARD-12-4068.

References

- [1] W. I. Park and G.-C. Yi, "Electroluminescence in *n*-ZnO Nanorod Arrays Vertically Grown on *p*-GaN," *Advanced Materials*, vol. 16, no. 1, pp. 87–90, 2004.
- [2] M. Law, L. E. Greene, J. C. Johnson, R. Saykally, and P. Yang, "Nanowire dye-sensitized solar cells," *Nature Materials*, vol. 4, no. 6, pp. 455–459, 2005.
- [3] Y. Qin, X. Wang, and Z. L. Wang, "Microfibre-nanowire hybrid structure for energy scavenging," *Nature*, vol. 451, no. 7180, pp. 809–813, 2008.
- [4] M. H. Huang, S. Mao, H. Feick et al., "Room-temperature ultraviolet nanowire nanolasers," *Science*, vol. 292, no. 5523, pp. 1897–1899, 2001.
- [5] Y.-J. Lee, D. S. Ruby, D. W. Peters, B. B. McKenzie, and J. W. P. Hsu, "ZnO nanostructures as efficient antireflection layers in solar cells," *Nano Letters*, vol. 8, no. 5, pp. 1501–1505, 2008.
- [6] S.-W. Lee, M.-C. Jeong, J.-M. Myoung, G.-S. Chae, and I.-J. Chung, "Magnetic alignment of ZnO nanowires for optoelectronic device applications," *Applied Physics Letters*, vol. 90, no. 13, Article ID 133115, 2007.
- [7] Y. J. Hong, H. S. Jung, J. Yoo et al., "Shape-controlled nanoarchitectures using nanowalls," *Advanced Materials*, vol. 21, no. 2, pp. 222–226, 2009.
- [8] L. E. Jensen, M. T. Björk, S. Jeppesen, A. I. Persson, B. J. Ohlsson, and L. Samuelson, "Role of surface diffusion in chemical beam epitaxy of InAs nanowires," *Nano Letters*, vol. 4, no. 10, pp. 1961–1964, 2004.
- [9] C.-H. Lee, J. Yoo, Y. J. Hong et al., "GaN/In_{1-x}Ga_xN/GaN/ZnO nanoarchitecture light emitting diode microarrays," *Applied Physics Letters*, vol. 94, no. 21, Article ID 213101, 2009.

- [10] W. I. Park, G.-C. Yi, J.-W. Kim, and S.-M. Park, "Schottky nano-contacts on ZnO nanorod arrays," *Applied Physics Letters*, vol. 82, no. 24, pp. 4358–4360, 2003.
- [11] A. K. Sharma, J. Narayan, J. F. Muth et al., "Optical and structural properties of epitaxial $\text{Mg}_x\text{Zn}_{1-x}\text{O}$ alloys," *Applied Physics Letters*, vol. 75, no. 21, pp. 3327–3329, 1999.
- [12] T. Minemoto, T. Negami, S. Nishiwaki, H. Takakura, and Y. Hamakawa, "Preparation of $\text{Zn}_{1-x}\text{Mg}_x\text{O}$ films by radio frequency magnetron sputtering," *Thin Solid Films*, vol. 372, no. 1, pp. 173–176, 2000.
- [13] M.-H. Jung and H. Lee, "Open selective patterning of zno nanorods on silicon substrates using nanoimprint lithography," *Nanoscale Research Letters*, vol. 6, article 159, 2011.
- [14] Y. Wei, W. Wu, R. Guo, D. Yuan, S. Das, and Z. L. Wang, "Wafer-scale high-throughput ordered growth of vertically aligned ZnO nanowire arrays," *Nano Letters*, vol. 10, no. 9, pp. 3414–3419, 2010.
- [15] S. Xu, Y. Wei, M. Kirkham et al., "Patterned growth of vertically aligned ZnO nanowire arrays on inorganic substrates at low temperature without catalyst," *Journal of the American Chemical Society*, vol. 130, no. 45, pp. 14958–14959, 2008.
- [16] J. J. Dong, X. W. Zhang, Z. G. Yin et al., "Controllable growth of highly ordered ZnO nanorod arrays via inverted self-assembled monolayer template," *ACS Applied Materials and Interfaces*, vol. 3, no. 11, pp. 4388–4395, 2011.
- [17] J. J. Richardson, G. K. L. Goh, H. Q. Le, L.-L. Liew, F. F. Lange, and S. P. Denbaars, "Thermally induced pore formation in epitaxial ZnO films grown from low temperature aqueous solution," *Crystal Growth and Design*, vol. 11, no. 8, pp. 3558–3563, 2011.
- [18] S. M. Jeon, M. S. Kim, M. Y. Cho et al., "Fabrication of porous ZnO nanorods with nano-sized pores and their properties," *Journal of the Korean Physical Society*, vol. 57, no. 6, pp. 1477–1481, 2010.
- [19] J. M. Stiegler, R. Tena-Zaera, O. Idigoras, A. Chuvilin, and R. Hillenbrand, "Correlative infrared-electron nanoscopy reveals the local structure-conductivity relationship in zinc oxide nanowires," *Nature Communications*, vol. 3, article 1131, 2012.
- [20] J.-W. Cai, J.-P. Xu, X.-S. Zhang et al., "Defect-related visible luminescence of ZnO nanorods annealed in oxygen ambient," *Optoelectronics Letters*, vol. 8, no. 1, pp. 4–8, 2012.
- [21] A. B. Djurišić, Y. H. Leung, K. H. Tam et al., "Green, yellow, and orange defect emission from ZnO nanostructures: influence of excitation wavelength," *Applied Physics Letters*, vol. 88, no. 10, Article ID 103107, 2006.
- [22] K. H. Tam, C. K. Cheung, Y. H. Leung et al., "Defects in ZnO nanorods prepared by a hydrothermal method," *Journal of Physical Chemistry B*, vol. 110, no. 42, pp. 20865–20871, 2006.
- [23] K. S. Kim, H. Jeong, M. S. Jeong, and G. Y. Jung, "Polymer-templated hydrothermal growth of vertically aligned single-crystal ZnO nanorods and morphological transformations using structural polarity," *Advanced Functional Materials*, vol. 20, no. 18, pp. 3055–3063, 2010.
- [24] R. Xie, T. Sekiguchi, T. Ishigaki et al., "Enhancement and patterning of ultraviolet emission in ZnO with an electron beam," *Applied Physics Letters*, vol. 88, no. 13, Article ID 134103, 2006.

Research Article

Effects of Polaron and Quantum Confinement on the Nonlinear Optical Properties in a GaAs/Ga_{1-x}Al_xAs Quantum Well Wire

L. Caroline Sugirtham,¹ A. John Peter,² and Chang Woo Lee³

¹ Department of Physics, Fatima College, Madurai 625 018, India

² Department of Physics, Government Arts College, Melur 625 106, Madurai, India

³ Department of Chemical Engineering, College of Engineering, Kyung Hee University, 1732 Deogyong-daero, Giheung, Yongin, Gyeonggi 446-701, Republic of Korea

Correspondence should be addressed to A. John Peter; a-johnpeter@rediffmail.com

Received 17 November 2013; Revised 26 January 2014; Accepted 10 February 2014; Published 11 March 2014

Academic Editor: Wen Lei

Copyright © 2014 L. Caroline Sugirtham et al. This is an open access article distributed under the Creative Commons Attribution License, which permits unrestricted use, distribution, and reproduction in any medium, provided the original work is properly cited.

The binding energy of a polaron confined in a GaAs/Ga_{1-x}Al_xAs quantum well wire is calculated within the framework of the variational technique and Lee-Low Pines approach. The polaron-induced photoionization cross section as a function of normalized photon energy for a on-centre donor impurity in the quantum wire is investigated. The oscillator strength with the geometrical effect is studied taking into account the polaron effects in a GaAs/Ga_{0.8}Al_{0.2}As quantum well wire. The effect of polaron on the third-order susceptibility of third harmonic generation is studied. Our theoretical results are shown to be in good agreement with previous investigations.

1. Introduction

The electronic properties and the potential applications for fabricating high performance novel optical devices in low dimensional semiconductor systems (LDSS) are quite interesting. The LDSSs can be produced with molecular beam epitaxy, metal organic chemical vapor deposition, chemical self-assemble technique, electron lithography, and molecular imprinted polymer. A lot of theoretical approaches have been devoted to study the nonlinear optical properties such as absorption coefficients, changes of refractive index, optical rectification coefficients, and second and third harmonic generation coefficients of these LDSSs [1–5]. These nonlinear optical properties pave the way for using any LDSS as probe for studying its electronic structure. The reduction in dimensionality in LDSS leads to a dramatic enhancement of optical nonlinearities. Electric field-induced polaron energy with a modified variational technique in a GaAs/Al_xGa_{1-x}As parabolic quantum well has been investigated by Zhao and Guo [6] who included the longitudinal optical phonons and the four branches of interface modes of phonon-polaritons in their study.

The study of phonon effect on any charged particle has been given due attention nowadays since the electron-phonon interactions are considered to be more pronounced phenomena and expected to modify the electronic structure and transport properties of these systems since the phonons are confined in LDSSs. Especially, the electron-phonon interaction is enhanced by the spatial confinement and eventually one can expect the multiphonon processes. In particular, the electron-phonon interaction is necessary to comprehend the optical absorption spectra in materials. In fact, the effects of polaronic states are affected by the changes in the form developed by Fröhlich Hamiltonian describing the electron-phonon interaction. Effects of electron and impurity ion LO phonon couples on the impurity states in cylindrical quantum wires have been dealt with [7]. Polaron effect in a wide band gap GaN material has been investigated by Zhang et al. [8], who studied the electron couples with both branches of longitudinal optical-like and transverse optical-like phonons in the presence of electric field.

Polaron-induced third-order nonlinear optical susceptibility in a GaAs quantum disk has been investigated [9].

Exciton-phonon scattering in quantum wires along with the geometrical confinement has been investigated earlier [10]. The ground state energy of an electron coupled with a Coulomb potential and a longitudinal-optical phonon field in a quantum wire has been studied [11]. Vasilevskiy et al. [12] proposed a nonperturbative and nonadiabatic approach for the calculation of the polaron effect on the Raman scattering which gives information about single particle excitations.

In the present work, the binding energy of a polaron confined in a GaAs/Ga_{1-x}Al_xAs quantum well wire is calculated within the framework of the variational and Lee-Low Pines approach. The oscillator strength as a function of wire radius is studied with and without the phonon effects. The polaron-induced photoionization cross section as a function of normalized photon energy for on-centre donor impurity in the quantum wire is investigated. The effect of polarons on the third-order susceptibility of third harmonic generation is studied. The method followed is presented in Section 2 while the results and discussion are provided in Section 3.

2. Model and Calculation

Based on the effective mass approximation, the Hamiltonian of a hydrogenic shallow donor impurity located at the centre of a quantum well wire, GaAs/Ga_{1-x}Al_xAs, is considered. An electron which interacts with the phonons described by the Fröhlich Hamiltonian is given by

$$H = H_e + H_{ph} + H_{e-ph}, \quad (1)$$

where H_e is the Hamiltonian of the electron without including phonons given by

$$H_e = -\frac{\hbar^2}{2m_e^*} \left[\frac{\partial^2}{\partial \rho^2} + \frac{1}{\rho} \frac{\partial}{\partial \rho} + \frac{\partial^2}{\partial z^2} + \frac{1}{\rho^2} \frac{\partial^2}{\partial \phi^2} \right] - \frac{e^2}{\epsilon_\infty \sqrt{\rho^2 + z^2}} + V(\rho), \quad (2)$$

where ϵ_∞ is the optical dielectric constant of the wire material and m_e^* is the effective mass of electron defined as

$$\frac{1}{m_e^*} = \frac{1}{m_0} + \frac{2P^2}{3\hbar^2} \left[\frac{2}{E_g} + \frac{1}{E_g + \Delta} \right], \quad (3)$$

where E_g is the band gap and Δ is the spin orbit energy of GaAs material. The confining potential, $V(\rho)$, is given as

$$V(\rho) = \begin{cases} 0, & 0 \leq \rho \leq R, \\ V_0, & \rho > R, \end{cases} \quad (4)$$

where $V(\rho)$ is the barrier height corresponding to 60% of the difference between the forbidden band of inner and outer material of the wire with $\Delta E_g = (1.36x + 0.22x^2)$ eV [13]. Here, the optical dielectric constant describes the electron cloud screening:

$$H_{ph} = \sum_{\vec{q}} \hbar \omega_{LO} a_{\vec{q}}^\dagger a_{\vec{q}}, \quad (5)$$

where $a_{\vec{q}}^\dagger a_{\vec{q}}$ and $b_{\vec{q}}^\dagger b_{\vec{q}}$ are the phonon creation and annihilation operators with wave vector \vec{q} with the frequency ω_{LO} . It describes noninteracting optical phonon system. These operators satisfy the commutation relations $[a_{\vec{q}}^\dagger, a_{\vec{q}'}] = \delta_{\vec{q}, \vec{q}'}$. This gives Bose statistics to the phonons. The energy value for LO phonon is taken as $\hbar \omega_{LO} = 36.75$ meV at 4.2 K.

The electron-phonon interaction, H_{e-ph} , is given by [14]

$$H_{e-ph} = \sum_{mlk_z} \{ [V_{LO}^*(r) e^{im\phi} e^{ik_z z} - V_{LO}^*(r_i)] a_{ml}^+(k_z) + \text{h.c.} \}, \quad (6)$$

where V_{LO}^* is the Fourier coefficient of the electron-phonon interaction, due to the LO phonons. The matrix elements, V_{LO}^* , bring out the strength of the interaction and, in fact, depend on the wave vector. The coupling parameter, V_{LO}^* , is given by

$$V_{LO}^* = \begin{cases} \Gamma_{LO}^{*ml}(k_z) J_m \left(\frac{\chi_m^l r}{R} \right), & r \neq 0, \\ \Gamma_{LO}^{*ml}(k_z), & r = 0, \end{cases} \quad (7)$$

where the coupling coefficient of the electron-phonon interaction is given by

$$\Gamma_{LO}^{*ml}(k_z) = \frac{i\sqrt{2}e(\hbar\omega_{LO})^{1/2}}{\sqrt{L}(\chi_m^l + k_z^2 R^2)^{1/2} J_{m+1}(\chi_m^l)} \left(\frac{1}{\epsilon_0} - \frac{1}{\epsilon_\infty} \right)^{1/2}, \quad (8)$$

where $m = 0, \pm 1, \pm 2, \dots$, $l = 1, 2, 3, \dots$, where L is the length of the quantum wire along the z -axis and J_m is the m th order Bessel function of the first order. χ_m^l is the l th root of J_m .

We follow the variational method developed by Lee-Low Pines [15, 16] using the expression for unitary transformation as

$$U_0 = \exp \left\{ \left[\sum_{m,l,q_z} (a_{\vec{q}}^\dagger + a_{\vec{q}}) \left[\frac{V_{LO}(\rho)}{\hbar\omega_{LO}} + \frac{V_{TO}(\rho)}{\hbar\omega_{TO}} \right] \right] \right\},$$

$$U_1 = \exp \left\{ i \left[K_z - \sum_{m,l,q_z} q_z Z a_{\vec{q}}^\dagger a_{\vec{q}} - \sum_{n,k_{zz}} q_z Z b_{\vec{q}}^\dagger b_{\vec{q}} \right] \right\}, \quad (9)$$

$$U_2 = \exp \left[\sum_{m,l,q_z} f_{ml}^{LO}(q_z, z) a_{\vec{q}}^\dagger - \text{h.c.} \right] + \exp \left[\sum_{n,k_{zz}} f_n^{TO}(q_z, z) b_{\vec{q}}^\dagger - \text{h.c.} \right]$$

where f_{ml}^{LO} are the f_n^{TO} are the parameters to be determined by minimizing the expectation of the bound polaron Hamiltonian. Thus, the effective Hamiltonian for the bound polaron in the phonon vacuum state can be derived as

$$H_{\text{eff}} = \langle 0 | U_2^{-1} U_1^{-1} \hat{H} U_1 U_2 | 0 \rangle. \quad (10)$$

The trial wave function for the taken system is the product of the wave function chosen as $\psi(r)$ and the phonon vacuum state $|0\rangle$. The trial wave function is chosen as

$$\psi_{nlk}(\rho, \phi, z) = \begin{cases} N_1 \exp(ikz) \exp(\pm il\phi) J_l(r_{nl}\rho), & \rho < R, \\ N_1 \frac{J_l(r_{nl}R)}{k_l(b_{nl}R)} \exp(\pm il\phi) K_l(b_{nl}\rho), & \rho \geq R, \end{cases} \quad (11)$$

where N_1 is the normalization constant and r_{nl} and b_{nl} are given by

$$r_{nl} = \sqrt{\frac{2m_e^* E_{nlk}}{\hbar^2}}, \quad (12)$$

$$b_{nl} = \sqrt{\frac{2m_e^* [V_0 - E_{nlk}]}{\hbar^2}},$$

where E_{nlk} is the ground state lowest binding energy which is obtained as the first root of the transcendental equation.

The trial wave function, considering the Coulomb interaction, is given by

$$\psi_{nlk}(\rho, \phi, z) = \begin{cases} N_2 \exp(ikz) \exp(\pm il\phi) J_l(r_{nl}\rho) \exp\left(-\delta(\rho^2 + z^2)^{1/2}\right), & \rho < R, \\ N_2 \frac{J_l(r_{nl}R)}{k_l(b_{nl}R)} \exp(\pm il\phi) K_l(b_{nl}\rho) \exp\left(-\delta(\rho^2 + z^2)^{1/2}\right), & \rho > R, \end{cases} \quad (13)$$

where N_2 is the normalization constant and α is the variation parameter.

The binding energy of the donor is defined as

$$E_b = E_0 - \langle H(\rho, \phi, z) \rangle_{\min}, \quad (14)$$

where E_0 is the free polaron energy and $\langle H(\rho, \phi, z) \rangle$ is obtained by minimizing the Hamiltonian (1) with respect to the variational parameter, δ . The Schrödinger equation is solved variationally by finding $\langle H(\rho, \phi, z) \rangle$ and the binding energy of the donor in a quantum well wire is given by the difference between the energy with and without the Coulomb interaction.

In general, the photoionization cross section, in any low dimensional semiconductor system, is described as the optical transition of an electron from the impurity ground state to any one of the final subband states. In fact, it requires an adequate energy for the transition from one level to another level. The distribution of wave function is explained by this process. The expression for the photoionization process in the standard dipole approximation is given by [17]

$$\sigma(\hbar\omega) = \left(\frac{E_{\text{eff}}}{E}\right)^2 \frac{n}{\epsilon} \frac{4\pi^2}{3} \eta \hbar \omega \sum_f |\langle \psi_i | \vec{r} | \psi_f \rangle|^2 \delta(E_f - E_i - \hbar\omega), \quad (15)$$

where E_{eff}/E is the effective field ratio taken as unity for simplicity, n is the refractive index of the semiconductor, ϵ is the dielectric constant of GaAs, η is the fine structure constant, and $\hbar\omega$ is the photon energy. The energy conserving delta function by the Lorentzian is given by

$$\delta(E_f - E_i - \hbar\omega) \rightarrow \frac{\Gamma}{\pi [(E_f - E_i - \hbar\omega)^2 + \Gamma^2]}, \quad (16)$$

where Γ is the line width of the hydrogenic impurity for which the value is taken as 1 meV. The final state may be taken as

$$\psi_f = A_4 \left(\frac{2}{LS}\right)^2 \exp(i\vec{k}_\perp \cdot \vec{\rho}) \sin(k_{11}\rho), \quad \rho < R, \quad (17)$$

where L is the length of the wire, S is the surface area, A_4 is the normalization constant, and

$$\exp(i\vec{k}_\perp \cdot \vec{\rho}) = J_0(k_\perp \rho) + 2 \sum_{m=1}^{\infty} i^m J_m(k_\perp \rho) \cos(m[\theta - \theta_k]), \quad (18)$$

J_0, J_m are Bessel functions, and θ_k is the direction of vector \vec{k}_\perp . For light polarized in the z -direction, the transition from the impurity ground state to the final state is obtained as

$$\begin{aligned} & \langle \psi_f | \rho | \psi_i \rangle \\ &= \hbar^2 \times \left(2m^* (E_i - E_f) \right) \\ & \times \left\{ \left\langle \psi_f \left| \frac{\partial}{\partial \rho} \right| \psi_i \right\rangle_{\rho < R} + \left\langle \psi_f \left| \frac{\partial}{\partial \rho} \right| \psi_i \right\rangle_{\rho > R} \right\}^{-1}, \end{aligned} \quad (19)$$

where ω is the angular frequency of the incident photon energy and E_i and E_f are the confined energies of initial and final states.

For any electronic system transitions, these calculations are important to compute the different linear and nonlinear optical properties. However, the dipole transitions are allowed using the selection rules $\Delta l = \pm 1$, where l is the angular momentum quantum number. In addition to that the oscillator strength, which is related to the dipole transition, is expressed as

$$P_{fi} = \frac{2m^*}{\hbar^2} \Delta E_{fi} |M_{fi}|^2, \quad (20)$$

where $\Delta E_{fi} = E_f - E_i$ refers to the difference of the energy between the lower and upper states. $M_{fi} = 2\langle \psi_f | er | \psi_i \rangle$ is the electric dipole moment of the transition from i state to f state in the quantum wire. The matrix element is important for the calculation of different optical properties of the system related to the electronic transitions. The observation of oscillator strength is essential especially in the study of optical properties and they are related to the electronic dipole allowed absorptions. Moreover, the outcome of the results will be viewed on the fine structure of the optical absorption.

The third-order nonlinear optical susceptibility $\chi^{(3)}$ which is related to the optical mixing between two incident light beams with different frequencies ω_1 and ω_2 is expressed as [18, 19]

$$\chi^{(3)}(-2\omega_1 + \omega_2, \omega_1, -\omega_2) = \frac{-2i\sigma_s e^4 \left| \langle \psi_i | \vec{r} | \psi_f \rangle \right|^4}{\epsilon_0 \hbar^3 [i(\omega_0 - 2\omega_1 + \omega_2) + \Gamma] [i(\omega_2 - \omega_1) + \Gamma]} \quad (21)$$

$$\times \left[\frac{1}{i(\omega_0 - \omega_1) + \Gamma} + \frac{1}{i(\omega_2 - \omega_0) + \Gamma} \right],$$

where σ_s is the density of electrons in the quantum well wire, ϵ_0 is the vacuum permittivity, $\Gamma = 1/\tau$ is the relaxation rate for states 1 and 2, and $\hbar\omega$ is the photon energy. We have taken the relaxation rate as 1 ps and the electron density is taken as $1 \times 10^{24} \text{ m}^{-3}$. The above equation gives the expression for the third-order susceptibility of third-order harmonic generation which has been done by the compact-density-matrix approach.

3. Results and Discussion

All material parameters are considered in atomic units in which \hbar and e^2 are taken as unity. With the introduction of Rydberg scale, the effective Rydberg energy is defined as $R^* = m_e^* e^4 / 2\hbar^2 \epsilon_0^2$ and the effective Bohr radius as $R_B^* = \hbar^2 \epsilon_0 / m_e^* e^2$, and hence, the values of these quantities, for GaAs semiconductor, become $R^* = 5.28 \text{ meV}$, $R_B^* = 103 \text{ \AA}$. The parameters used in our calculations are $m_e^* = 0.067m_0$, where m_0 is the free electron mass, $\hbar\omega_{LO} = 36.75 \text{ meV}$, $\epsilon_0 = 13.16$, $\epsilon_\infty = 10.89$, and the barrier height, V_0 , is taken as 168.8 meV. The effective field ratio, E_{eff}/E , is assumed to be unity since the wave function is extended far from the impurity.

Figure 1 shows the donor binding energy of an impurity as a function of wire radius in a GaAs/Ga_{0.8}Al_{0.2}As quantum well wire with and without the polaron effects. Curve (1) represents with LO phonon contribution and curve (2) contributes to the phonon corrections. And the insert figure shows the corresponding polaronic shift due to LO phonons. It is observed that the donor binding energy monotonically increases with decreasing wire radius due to the geometrical confinement. When the wire radius decreases the electron wave function is more compressed in the quantum wire leading to an enhancement of binding energy. It is also observed that the coupling between the electron and phonon enhances the donor binding energy and this enhancement of binding energy is more pronounced for smaller wire radius. Thus, the ground state polaron energies increase with decreasing wire radius rapidly for narrow wires but slowly for larger wire radius. As a result the total binding energy incorporating the contributions of electron interaction with the LO phonon also enhances. The results are in good agreement with other investigators [20, 21]. It is found out from the insert figure that both the contributions of LO phonon with the polaron energy increase when the wire radius is decreased and this effect is more pronounced when the wire radius is decreased.

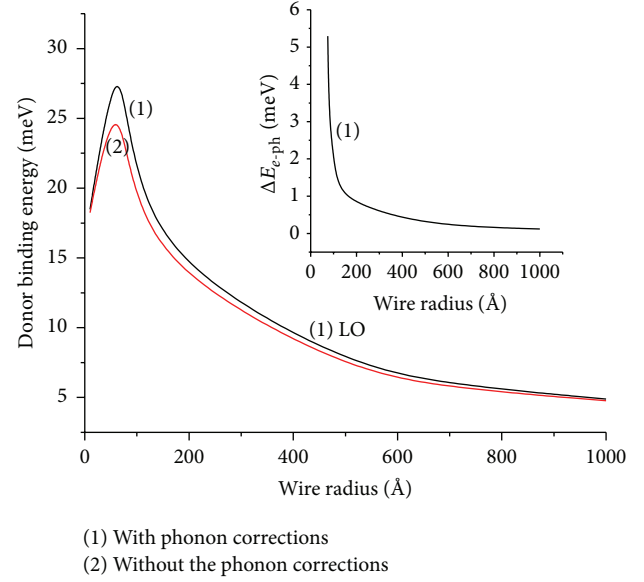


FIGURE 1: Binding energy of an impurity as a function of wire radius in a GaAs/Ga_{0.8}Al_{0.2}As quantum well wire with and without the polaron effects. Curve (1) represents for the LO phonon contribution and curve (2) contributes for the phonon corrections. The insert figure shows the corresponding polaronic shift due to LO phonons.

The phonon correction is found to have more influence for narrow wire in which the maximum binding energy is obtained. This is due to the fact that as the radius of the wire is reduced, the electron wave function becomes more localized and eventually the electron-phonon interaction is enhanced. Hence, it is concluded that the phonon contribution should not be neglected for any low dimensional semiconductor system.

In Figure 2, we represent the variation of oscillator strength as a function of wire radius in a GaAs/Ga_{0.8}Al_{0.2}As quantum well wire with and without the polaron effects. Curve (1) denotes with LO phonon contribution and curve (2) represents without the phonon. It is observed that the phonon induced oscillator strength of the hydrogenic impurity decreases with the decrease in wire radius and the oscillator strength increases when the effects of phonon contribution are included. This is because the hydrogenic binding energy increases when the phonon contribution is included as seen earlier. The enhancement of energy difference of two different electronic states, due to the small transition probability between initial and final states, is observed with the inclusion of effects of phonon. Also, the reduction of recombination rate of the hydrogenic donor and the transition energy are observed when the wire radius is increased and further, the decay time also decreases when the geometrical confinement is reduced. The electron is more confined when the wire radius is decreased due to the pronounce effects of geometrical confinement. Eventually, the recombination rate is reduced [22].

In Figure 3, we display the variation of photoionization cross section as a function of normalized photon energy with and without the polaron effect for a 50 Å wire radius

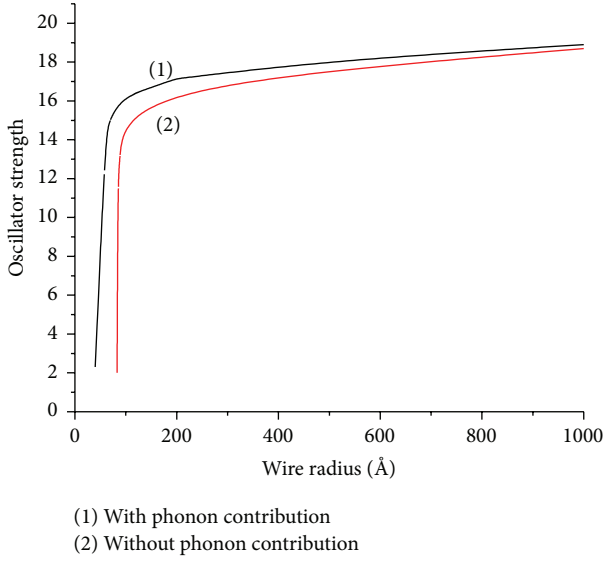


FIGURE 2: Variation of oscillator strength as a function of wire radius in a GaAs/Ga_{0.8}Al_{0.2}As quantum well wire with and without the polaron effects. Curve (1) denotes with LO phonon contribution and curve (2) represents without the phonon contribution.

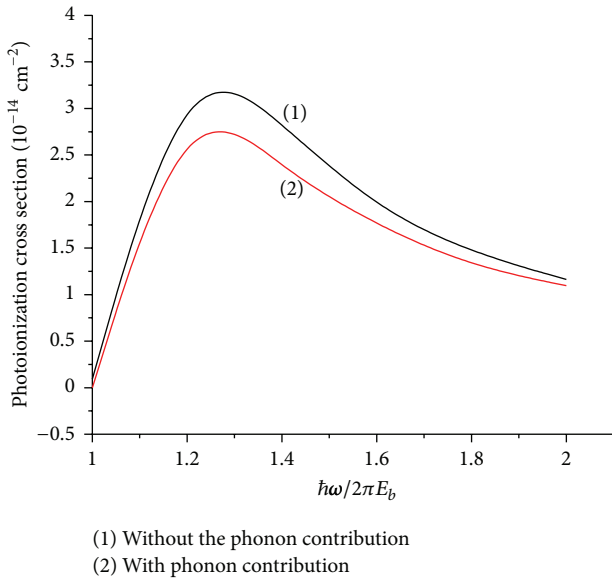


FIGURE 3: Variation of photoionization cross section as a function of normalized photon energy with and without the polaron effect for a 50 Å wire radius in a GaAs/Ga_{0.8}Al_{0.2}As quantum well wire.

in a GaAs/Ga_{0.8}Al_{0.2}As quantum well wire. The photoionization cross section rises at lower energies whereas it decreases smoothly for larger photon energies [23]. It is because both the subband energies and the impurity binding energy increase with decreasing wire radius, the frequency at which the photoionization cross section peaks, increases with decreasing wire size. This figure clearly brings out the quantum size effect. Further, it is found that the magnitude of the photoionization cross section becomes higher and shifts

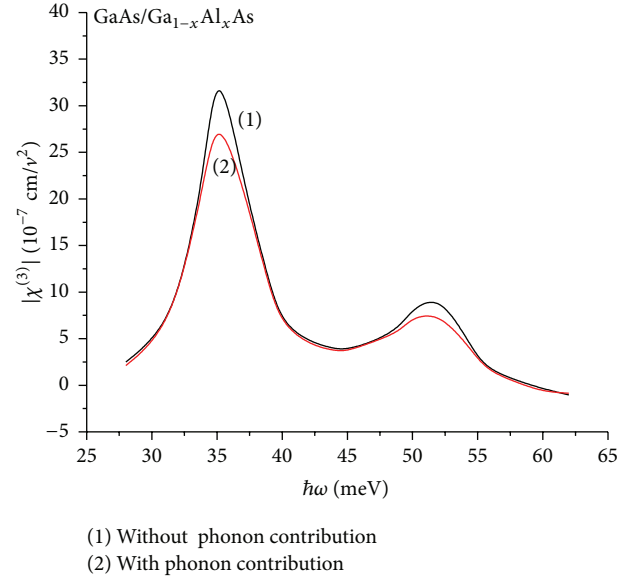


FIGURE 4: Variation of third-order susceptibility of third harmonic generation as a function of photon energy with and without the polaron effects in a GaAs/Ga_{0.8}Al_{0.2}As quantum well wire.

towards the higher photon energies when the polaronic effect is included. It is due to the enhancement of optical matrix element between the initial and final states. It results in the increase of magnitude of the photoionization cross section.

Figure 4 shows the plot of variation of third-order susceptibility of third harmonic generation as a function of photon energy with and without considering the effects of electron-phonon interactions. In this figure, curve (1) refers to without the phonon contribution and curve (2) denotes LO phonon contribution. 50 Å wire radius of a GaAs/Ga_{0.8}Al_{0.2}As quantum well wire is taken with $\hbar\omega_0 = 50$ meV. It is observed that the susceptibility has two peaks and the contribution of phonon makes the resonant peak towards higher region of energies [24, 25]. Further, it is noted that the magnitude of the resonant peak moves towards the higher energies with the increase of phonon effects. The coefficient of third-order susceptibility of third harmonic generation has been enhanced with the polaronic effects [25]. The relaxation time has more influence on the third-order susceptibility. It is found that the coefficient of third-order susceptibility with considering the polaron effect is 1.5 times larger than obtained without considering the electron-phonon interaction. It is due to the enhancement of matrix element. LO phonons enhance third-order nonlinear optical susceptibilities of third harmonic generation. And hence, it is concluded that the contribution of phonon has more influence on the resonant peak of third-order susceptibility of third harmonic generation.

In conclusion, the polaron-induced binding energy has been computed in a GaAs/Ga_{1-x}Al_xAs quantum well wire. Numerical calculations have been carried out using variational method within the single band effect mass approximation and Lee-Low Pines approach. The effects on oscillator strength with the spatial confinement have been dealt with.

The polaron-induced photoionization cross section as a function of normalized photon energy for on-centre donor impurity in the quantum wire has been investigated. The polaron-induced third-order susceptibility of third harmonic generation has been investigated. The results show that the donor binding energy is enhanced by the electron-phonon interactions, the effect of phonon contribution is pronounced for smaller wire radii, and the coefficient of third-order susceptibility of third harmonic generation has been enhanced with the polaronic effects. The effects of phonon should be taken into account for narrow wires. We hope that the present work would stimulate further investigations on nonlinear optical properties in a weak polar material and the lattice dynamic properties in the near future.

Conflict of Interests

The authors declare that there is no conflict of interests regarding the publication of this paper.

References

- [1] G. Rezaei, M. J. Karimi, and A. Keshavarz, "Excitonic effects on the nonlinear intersubband optical properties of a semi-parabolic one-dimensional quantum dot," *Physica E*, vol. 43, no. 1, pp. 475–481, 2010.
- [2] W. Xie, "Dipole-allowed optical absorption of an exciton in a spherical parabolic quantum dot," *Optics Communications*, vol. 282, no. 13, pp. 2604–2607, 2009.
- [3] M. Şahin, "Third-order nonlinear optical properties of a one- and two-electron spherical quantum dot with and without a hydrogenic impurity," *Journal of Applied Physics*, vol. 106, Article ID 063710, 2009.
- [4] I. Karabulut and S. Baskoutas, "Linear and nonlinear optical absorption coefficients and refractive index changes in spherical quantum dots: effects of impurities, electric field, size, and optical intensity," *Journal of Applied Physics*, vol. 103, no. 7, Article ID 073512, 2008.
- [5] S. Winter, M. Zielinski, D. Chauvat, J. Zyss, and D. Oron, "The second order nonlinear susceptibility of quantum confined semiconductors—a single dot study," *Journal of Physical Chemistry C*, vol. 115, no. 11, pp. 4558–4563, 2011.
- [6] F.-Q. Zhao and Z.-Z. Guo, "Electric field effects on polarons with spatially dependent mass in parabolic quantum wells," *International Journal of Modern Physics B*, vol. 18, no. 22, pp. 2991–2999, 2004.
- [7] Z. Zhao and X. Liang, "Effects of electron-and impurity-ion-LO phonon couples on the impurity states in cylindrical quantum wires," *Journal of Semiconductors*, vol. 30, no. 6, Article ID 062002, 2009.
- [8] B. Zhang, Z. Yan, and M. Zhang, "Bound polaron in a strained wurtzite $\text{GaN}/\text{Al}_x\text{Ga}_{1-x}\text{N}$ cylindrical quantum dot," *Journal of Semiconductors*, vol. 32, no. 6, Article ID 062003, 2011.
- [9] C.-H. Liu, K.-X. Gao, C.-Y. Chen, and B.-K. Ma, "Polaron effects on the third-order nonlinear optical susceptibility in a quantum disk," *Physica E*, vol. 15, no. 4, pp. 217–228, 2002.
- [10] S.-D. Liang, C. Y. Chen, S. C. Jiang, and D. L. Lin, "Size effect on exciton-phonon scattering in quantum wires," *Physical Review B*, vol. 53, no. 23, pp. 15459–15461, 1996.
- [11] Q. H. Chen, Z. B. Wang, F. L. Wu et al., "Variational path-integral study on bound polarons in parabolic quantum dots and wires," *Chinese Physics Letters*, vol. 18, no. 5, p. 668, 2001.
- [12] M. I. Vasilevskiy, R. P. Miranda, E. V. Anda, and S. S. Makler, "Polaron effect on Raman scattering in semiconductor quantum dots," *Semiconductor Science and Technology*, vol. 19, no. 4, pp. S312–S315, 2004.
- [13] C. Bosio, J. L. Staehli, M. Guzzi, G. Burri, and R. A. Logan, "Direct-energy-gap dependence on Al concentration in $\text{Al}_x\text{Ga}_{1-x}\text{As}$," *Physical Review B*, vol. 38, no. 5, pp. 3263–3268, 1988.
- [14] P. M. Platzman, "Ground-state energy of bound polarons," *Physical Review*, vol. 125, no. 6, pp. 1961–1965, 1962.
- [15] W. J. Huybrechts, "Internal excited state of the optical polaron," *Journal of Physics C*, vol. 10, no. 19, p. 3761, 1977.
- [16] T. Lu and Y. Zheng, "Polaron properties in quantum wells," *Physical Review B*, vol. 53, no. 3, pp. 1438–1445, 1996.
- [17] M. Lax, "Photoconductivity," in *Proceedings of the Atlantic City Conference on Photoconductivity*, R. G. Breckenridge, B. R. Russell, and E. E. Hahn, Eds., p. 111, John Wiley & Sons, New York, NY, USA, 1954.
- [18] W. Xie, "Third-order nonlinear optical susceptibility of a donor in elliptical quantum dots," *Superlattices and Microstructures*, vol. 53, pp. 49–54, 2013.
- [19] T. Takagahara, "Excitonic optical nonlinearity and exciton dynamics in semiconductor quantum dots," *Physical Review B*, vol. 36, no. 17, pp. 9293–9296, 1987.
- [20] Z. Zengru and L. Xixia, "Effects of electron- and impurity-ion-LO phonon couples on the impurity states in cylindrical quantum wires," *Journal of Semiconductors*, vol. 30, no. 6, Article ID 062002, 2009.
- [21] R.-Q. Wang, H.-J. Xie, K.-X. Guo, Y.-B. Yu, and Y.-Q. Deng, "Polaronic effects of an exciton in a cylindrical quantum wire," *Communications in Theoretical Physics*, vol. 43, no. 1, pp. 169–174, 2005.
- [22] J. H. You, J. T. Woo, D. U. Lee, T. W. Kim, K. H. Yoo, and H. L. Park, "Dependence of optical gain and interband transitions on the CdTe well width and temperature for CdTe/ZnTe single quantum wells," *Optical and Quantum Electronics*, vol. 41, no. 7, pp. 559–565, 2009.
- [23] A. Sali, M. Fliyou, H. Satori, and H. Loumrhari, "The effect of a strong magnetic field on the binding energy and the photoionization process in quantum-well wires," *Journal of Physics and Chemistry of Solids*, vol. 64, no. 1, pp. 31–41, 2003.
- [24] Y.-B. Yu, S.-N. Zhu, and K.-X. Guo, "Polaron effects on third-harmonic generation in cylindrical quantum-well wires," *Solid State Communications*, vol. 132, no. 10, pp. 689–692, 2004.
- [25] Z. Chen, D. Yao, X. Zhang, and T. Fang, "Polaron effect-dependent third-order optical susceptibility in a ZnS/CdSe quantum dot quantum well," *Microelectronics Journal*, vol. 39, no. 12, pp. 1654–1658, 2008.

Research Article

Preparation and Characterization of Graphene Oxide

Jianguo Song,¹ Xinzhi Wang,¹ and Chang-Tang Chang²

¹ College of Environment and Materials Engineering, Yantai University, 30 Qingquan Road, Laishan District, Yantai 264005, China

² Department of Environmental Engineering, Ilan University, No. 1, Section 1 Shen-Lung Road, Yilan City 26047, Taiwan

Correspondence should be addressed to Jianguo Song; songjianguo@126.com and Chang-Tang Chang; ctchang@niu.edu.tw

Received 11 December 2013; Accepted 9 February 2014; Published 11 March 2014

Academic Editor: Wen Lei

Copyright © 2014 Jianguo Song et al. This is an open access article distributed under the Creative Commons Attribution License, which permits unrestricted use, distribution, and reproduction in any medium, provided the original work is properly cited.

Graphene oxide (GO) films with two-dimensional structure were successfully prepared via the modified Hummer method. It is proven that redox method is a promising way to synthesize GO films on a large scale. Comprehensive characterizations of the properties of GO films were conducted. TEM and DFM analyses showed that GO sheets prepared in this study had single and double lamellar layer structure and a thickness of 2~3 nm. X-ray diffraction (XRD) was selected to measure the crystal structure of GO sheet. Fourier-transform infrared spectra analyzer (FT-IR) was used to certify the presence of oxygen-containing functional groups in GO films. The tests of UV-VIS spectrometer and TGA analyzer indicated that GO sheet possessed excellent optical response and outstanding thermal stability. Elemental analyzer (EA) and X-ray photoelectron spectroscopy (XPS) analyzed the components synthetic material. Simultaneously, chemical structure of GO sheet was described in this study. Discussion and references for further research on graphene are provided.

1. Introduction

As early as 1947, Wallace [1] first proposed the concept of graphene and studied the electronic properties of graphene using tight-binding model. It is concluded that graphite is a semiconductor without activation energy, because of the small portion of valence band of graphite extended to the conduction band, in which data established a foundation for the use of the physical properties of graphite. However, since several decades, the study of graphene is still just staying at the level of theory [2–5].

Until 2004, Novoselov and Geim [6] in the University of Manchester firstly separated the single graphene from graphite through simple mechanical peeling method. Graphene was increasing more and more attention in various areas of science and technology due to its remarkable physicochemical properties.

As a one-atom-thick, two-dimensional crystal, graphene has been considered as basic building block for all sp² graphitic materials including fullerenes, carbon nanotubes, and graphite [6]. Owing to the special two-dimensional structure, graphene possessed many unique properties different than carbon materials, including a high specific surface area (theoretically 2630 m²/g for single-layer graphene)

[7], extraordinary electronic properties and electron transport capabilities [8–10], and high thermal conductivity ($\approx 5000 \text{ W m}^{-1} \text{ K}^{-1}$) [11, 12].

Currently, many methods had been explored to prepare graphene. Novoselov and Geim [6] firstly observed a single layer of graphene from highly oriented pyrolytic graphite using micromechanical exfoliation method. It is a simple way to prepare graphene, but the yield of graphene was very low, and you cannot achieve high-quality industrial production. Srivastava et al. [13] prepared “petal” graphite sheet with ~20 nm thickness by chemical vapor deposition (CVD). Even though thickness of graphite sheet prepared by CVD method significantly decreased than ever, more impurities Ni element in graphite sheet was another new problem. Solvent stripping method [14] is a new approach that emerged in recent years. Its principle is destroying Van Der Waals Force between the graphite layers in a solvent to obtain graphene sheets. Method of solvent stripping did not destroy the structure of the graphene and presented no surface defects in the graphene sheet. However, the low yield of graphene was still. Redox method [15–21] is the most popular method to prepare graphene and graphite oxide. During the oxidation process, graphite crystal was treated with strong oxidizing

agents and carried oxygen-containing functional groups into graphite oxide sheet. After thermal or ultrasonic treatment, the oxygen-containing functional groups were removed and obtained the graphene sheet. Production of graphene can be very high using redox method, and introduction of functional groups in the oxidation process provided advantages of combining the compound to improve the compatibility of matrix composite. Therefore, redox method was suitable for the preparation of graphene-based composite materials. Finally, chemical structure of GO sheet was also described in this study.

In summary, in order to turn graphene applications into reality, one must fabricate the material. The redox method is considered to be a very promising way to prepare graphene, and graphite oxide (GO), as intermediate product of preparation process has a crucial influence on the quality of graphene. Therefore, exploration for properties of graphite oxide is essential and imminent.

In view of these issues, this study successfully synthesized graphene oxide (GO) by the modified Hummers method, as the precursor for preparing graphene. The microscopic morphologies of GO sheets were characterized by transmission electron microscopy (TEM) and dynamic force microscope (DFM). The structures of the GO sheets were measured by Fourier-transform infrared spectra analyzer (FT-IR) and X-ray diffraction (XRD). A UV spectrometer (UV-VIS) was used to measure the optical absorption properties of the GO sheet. Thermal stability of GO sheets was determined through the thermal gravimetric analyzer (TGA). An elemental analyzer (EA) was used to analyze the elements in the GO sheet, including C and H.

2. Experiment and Methods

2.1. Chemicals and Materials. Graphite flake (natural, -325 mesh) with a purity of 99.8% was purchased from Alfa Aesar. All chemicals were of analytical grade and used as received.

2.2. Synthesis of Graphene Oxide (GO). GO was prepared according to the modified Hummer method [18, 22]. In detail, 5 g of graphite and 2.5 g of NaNO_3 were mixed with 108 mL H_2SO_4 and 12 mL H_3PO_4 and stirred in an ice bath for 10 min. Next, 15 g of KMnO_4 were slowly added so that the temperature of the mixture remained below 5°C . The suspension was then reacted for 2 h in an ice bath and stirred for 60 min before again being stirred in a 40°C water bath for 60 min. The temperature of the mixture was adjusted to a constant 98°C for 60 min while water was added continuously. Deionized water was further added so that the volume of the suspension was 400 mL. 15 mL of H_2O_2 was added after 5 min. The reaction product was centrifuged and washed with deionized water and 5% HCl solution repeatedly. Finally, the product was dried at 60°C .

2.3. Characterization. The microscopic morphologies of samples were characterized by transmission electron microscopy (TEM; JEOL inc., EM2100) and dynamic

force microscope (DFM, Seiko Instruments Inc., SPA-300 HV). The structures of materials were measured by Fourier-transform infrared spectra analyzer (FT-IR; Thermo Scientific inc., NICOLET iS10) and X-ray diffraction (XRD; Rigaku inc., Ultima IV). UV spectrometer (UV-VIS; Hitachi inc., U-3900) was used to measure the optical absorption properties of GO. Thermo gravimetric analyzer (TGA; Perkin Elmer Inc., STA6000) was used to determine the thermal stability of samples. Elemental analyzer (EA; German Elementar Analysensysteme inc., D-63452 Hanau) and X-ray Photoelectron Spectroscopy (XPS; England Thermo VG-Scientific inc., Sigma Probe) were used to analyze elements in GO sheet.

3. Results and Discussion

3.1. The Morphologies of GO Sheet. Figure 1(a) showed the GO product prepared in the present study. It indicated that the GO sheet exhibited brown and very thin lamellar structure on the macrolevel, and the yellow performance was more significant in relatively low concentrations. Meanwhile, GO sheets prepared in this study were very slim and had certain toughness, not easy to grind. GO product was dispersed in anhydrous ethanol and supported on the copper mesh and Si chip for the TEM and DFM tests, respectively. The results are shown in Figures 1(b) and 1(c). Single and double lamellar layer structure GO sheets were observed in the TEM image, while the size of the lamellar structure was about 3 μm and slight wrinkles were observed. The DFM image shows that the GO sheet layers have a thickness of $2 \sim 3 \text{ nm}$, which was slightly thicker than single layer graphene. The increased thickness is largely attributed to the insertion of oxygen-containing functional groups which make it thicker and change the surface of the GO sheet. Moreover, since the oxygen-energy groups were mainly combined with edges part of GO sheets, resulting in the phenomenon that the thickness of GO sheets was high in the edge portion and low in the middle portion.

3.2. The Structures of GO Sheet. XRD analysis was used to determine the average crystalline properties of the GO sheet. Results are shown in Figure 2(a). The GO sheet prepared showed a very strong peak at $2\theta = 10.2^\circ$, which is in good agreement with the literatures [23, 24]. The results of XRD initially proved the successful synthesis of GO sheet.

FTIR spectra analysis was performed to investigate the structure and functional groups of the materials, as shown in Figure 2(b). The GO sheet showed apparent adsorption bands for the carboxyl $\text{C}=\text{O}$ (1723 cm^{-1}), aromatic $\text{C}=\text{C}$ (1621 cm^{-1}), epoxy $\text{C}-\text{O}$ (1220 cm^{-1}), alkoxy $\text{C}-\text{O}$ (1043 cm^{-1}), and hydroxy $-\text{OH}$ (3391 cm^{-1}) groups. The presentation of oxygen-containing functional groups, such as $\text{C}=\text{O}$ and $\text{C}-\text{O}$, further confirmed that the graphite indeed was oxidized into GO and was consistent with the literatures [25–27]. The presentation of $\text{C}=\text{C}$ groups showed that even graphite had been oxidized into GO; the main structure of layer graphite was still retained. The results of XRD and FT-IR

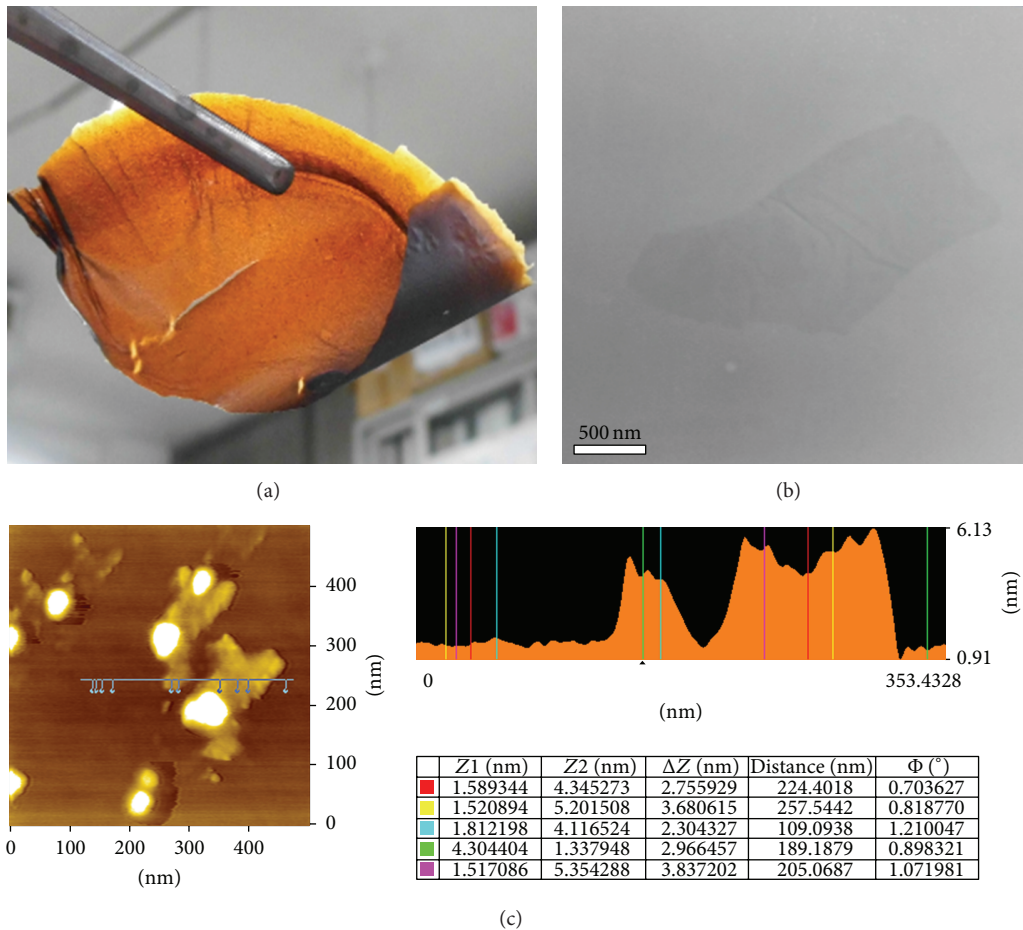


FIGURE 1: (a) The picture of GO product; (b) TEM; and (c) DFM pictures of GO sheet.

synthesis both further demonstrated the successful synthesis of GO sheet.

3.3. The Optical Absorption Properties of GO Sheet. The analysis of UV-VIS diffuse reflectance spectra of the GO sheet was shown in Figure 3(a). It is indicated that graphene oxide possessed a good absorption in the visible range (380~800 nm), but absorption in the ultraviolet range was also slightly decreased. The results showed the good photoresponse of GO sheet not only in ultraviolet range but also in visible range, which implied the enormous potential for application of light.

3.4. The Thermal Stability of GO Sheet. TGA analysis was conducted to test the thermal stability of GO sheet. Results were shown in Figure 3(b). Three stages were observed in the quality loss cure of the GO sheet. Firstly, a roughly 2% quality loss occurred at the temperature of 100°C, primarily due to the loss of H₂O molecules in the GO sheet layers. Secondly, the thermal decomposition of instable oxygen-containing functional groups showed a roughly 32% quality loss, occurring at a temperature of 225°C. Finally, a 45% quality loss occurred at 620°C was mainly due to the combustion of the carbon skeleton. The analysis results indicated the excellent

TABLE 1: The EA results of GO sheet.

Element%	C%	H%	S%	N%
GO	44.2	3.0	0.9	0.00

thermal stability of GO sheet. Graphite oxide was very stable substance in the normal state.

3.5. The Elementals Synthesis of GO Sheet. During the process of preparing the GO sheet via the modified Hummer method, the added mass of pure graphite was 5.0 g, and the final quantity of the obtained GO sheet was about 11.1 g. From this, we can theoretically infer that the content of C element in GO sheet was about 45.0%, which was consistent with the experimental results of the EA analysis, as shown in Table 1. In addition, H (3%) and S (0.9%) were observed in the GO sheet, primarily due to the presence of oxygen-containing functional groups embedded in the GO sheet. Meanwhile, based on the results of the EA, the O element content in the GO film was about 51%.

3.6. The XPS Analysis of GO Sheet. In order to further demonstrate the presentation of oxygen-containing functional groups, XPS analysis was conducted. The result was

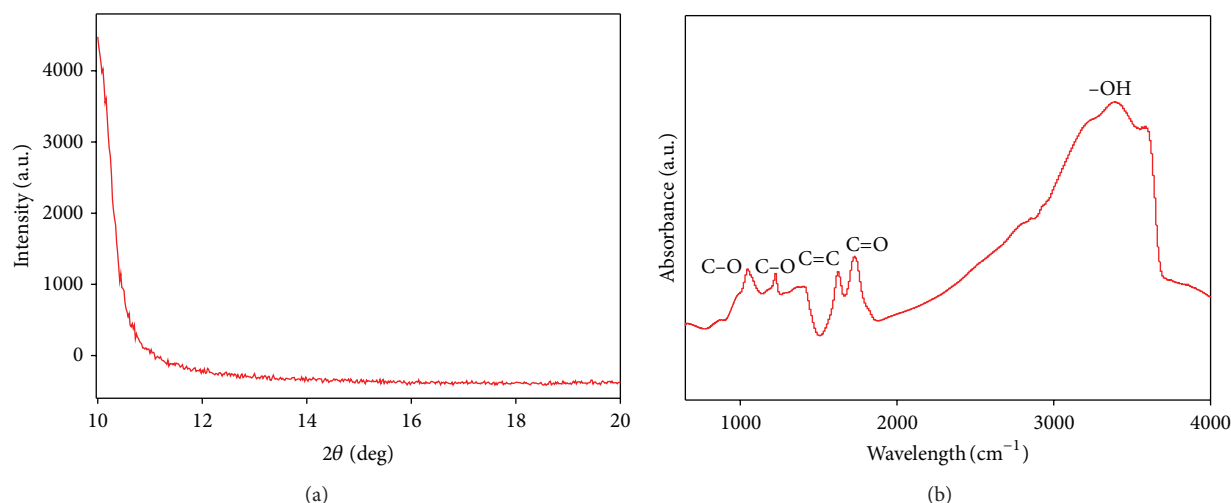


FIGURE 2: The (a) XRD and (b) FT-IR patterns of GO sheet.

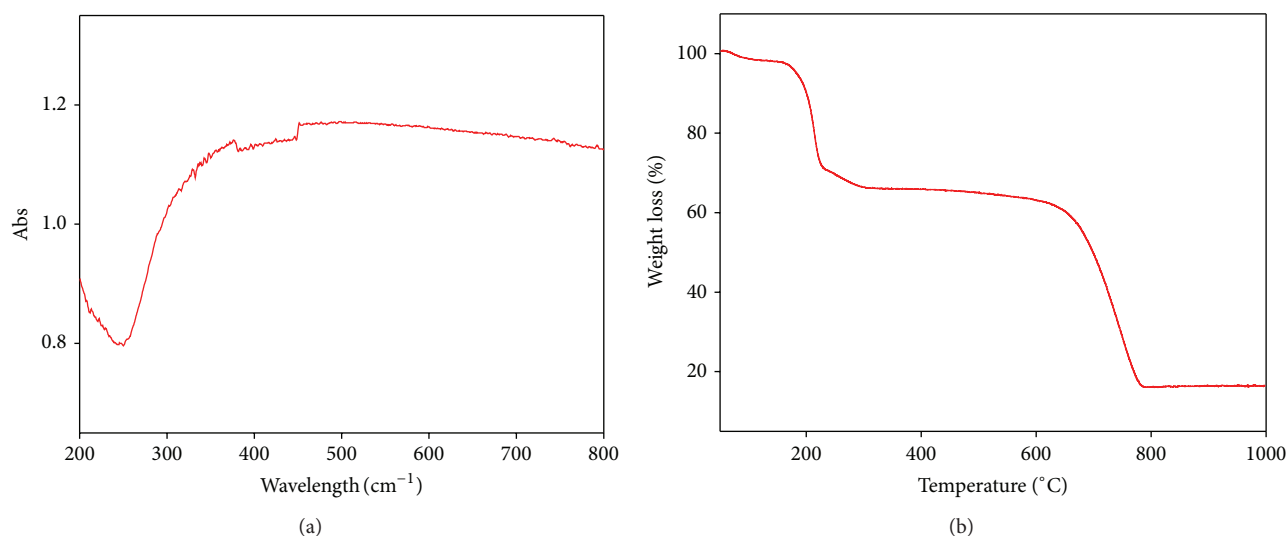


FIGURE 3: (a) The UV-VIS spectra of GO sheet; (b) the thermal gravimetric analysis diagram of GO sheet.

shown in Figure 4. XPS of GO showed significant C and O signals corresponding to the binding energy of GO. Figure 4(a) showed the significant peak of C signal with a binding energy of 285.0 eV, which can be attributed to the C=C, C-C and C-H functional groups. The peak centered at the binding energies of 532.1 eV can be assigned to the C-O and C=O bonds, as shown in Figure 4(b) [28]. This result suggested that GO sheet contains large numbers of functional groups on its surface, such as C-O and C=O, which also was in accordance with the XRD, FTIR, and EA analyses.

3.7. Structural Analysis of Graphite Oxide (GO). Graphene oxide (GO) was a specific branch of graphene research. It can be considered as a precursor for graphene synthesis by either thermal or chemical reduction processes. The schematic structure of graphite oxide (GO) was shown in Figure 5. It is indicated that GO sheet can be regarded as the combined

structure of oxygen-containing functional groups, such as C-O, C=O, and -OH, supported on the surface of a single layer graphene sheet [7, 29]. The addition of oxygen-containing functional groups changed the structure and properties of GO sheet.

Compared with single-layer graphene, on the one hand, the presence of oxygen-containing functional groups indeed greatly increased defectiveness of GO sheet. This may lead to some loss in electrical conductivity [29], which possibly limits the direct application of GO in many areas. On the other hand, the presence of these oxygen-containing functional groups also provided potential advantages for using GO in numerous other applications. For example, the polar oxygen functional groups in GO sheet render it strongly hydrophilic, which gave GO good dispersibility in many solvents, particularly in water [16, 30–32]. This also provided the conditions to synthesize composite materials.

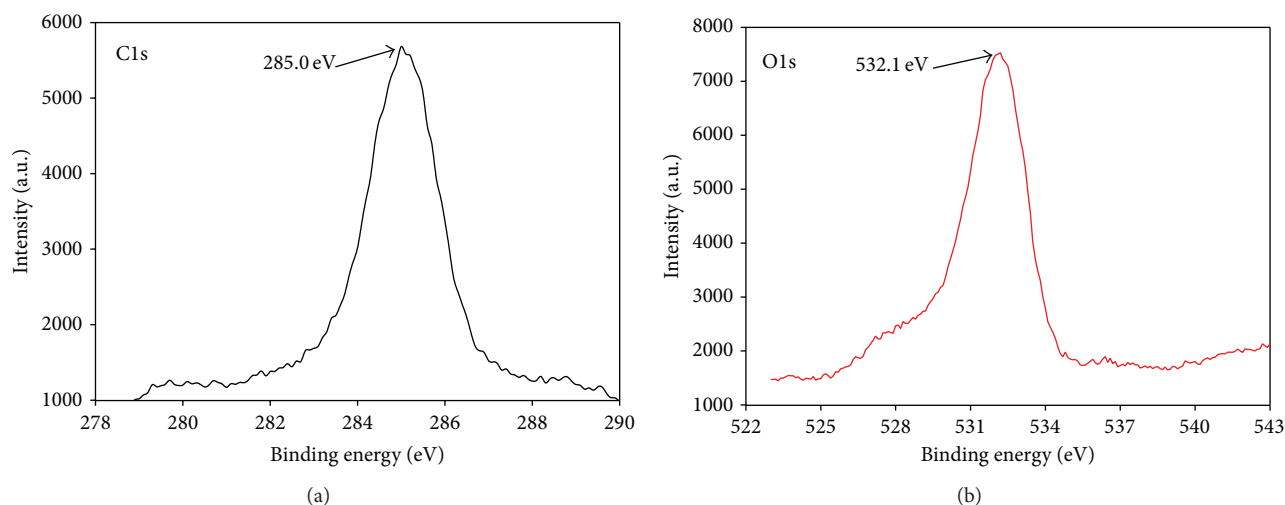


FIGURE 4: The C 1s (a) and O 1s (b) core-level XPS spectra of GO sheet.

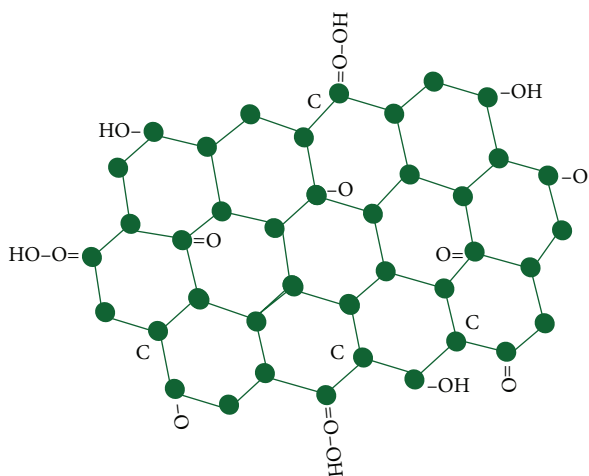


FIGURE 5: The schematic structure of graphite oxide (GO).

Simultaneously, these functional groups can be served as sites for chemical modification or functionalization of GO sheet, in order to easily apply in many other aspects.

4. Conclusions

GO films were successfully prepared via modified Hummer method. The TEM and DFM analyses showed successful preparation of GO films on microscopic morphology. The thickness of the monolayer GO sheet was between 2–3 nm.

The presence of oxygen-containing groups and characteristic peaks in FT-IR and XRD analysis further determined the successful preparation of GO sheets. Finally, EA indicated the component of O elements in GO films was about 51%; elements of C, H, and S were also observed. The presence of oxygen-containing functional groups provided more opportunities for potential applications of GO in many areas. These data will provide a reference to further study the nature of graphene and graphene oxide.

Conflict of Interests

The authors declare that there is no conflict of interests regarding the publication of this paper.

References

- [1] P. R. Wallace, "The band theory of graphite," *Physical Review*, vol. 71, no. 9, pp. 622–634, 1947.
- [2] H. P. Boehm, A. Clauss, G. O. Fischer, and U. Hofmann, "Dünne kohlenstoff-folien," *Verlag der Zeitschrift für Naturforschung B*, vol. 17, pp. 150–153, 1962.
- [3] A. J. van Bommel, J. E. Crombeen, and A. van Tooren, "LEED and Auger electron observations of the SiC(0001) surface," *Surface Science*, vol. 48, no. 2, pp. 463–472, 1975.
- [4] I. Forbeaux, J.-M. Themlin, and J.-M. Debever, "Heteroepitaxial graphite on 6H-SiC(0001): interface formation through conduction-band electronic structure," *Physical Review B*, vol. 58, no. 24, pp. 16396–16406, 1998.
- [5] C. Oshima, A. Itoh, E. Rokuta, T. Tanaka, K. Yamashita, and T. Sakurai, "Hetero-epitaxial-double-atomic-layer system of monolayer graphene/monolayer *h*-BN on Ni(111)," *Solid State Communications*, vol. 116, no. 1, pp. 37–40, 2000.
- [6] K. S. Novoselov, A. K. Geim, S. V. Morozov et al., "Electric field in atomically thin carbon films," *Science*, vol. 306, no. 5696, pp. 666–669, 2004.
- [7] M. D. Stoller, S. Park, Z. Yanwu, J. An, and R. S. Ruoff, "Graphene-based ultracapacitors," *Nano Letters*, vol. 8, no. 10, pp. 3498–3502, 2008.
- [8] X. Li, G. Zhang, X. Bai et al., "Highly conducting graphene sheets and Langmuir-Blodgett films," *Nature Nanotechnology*, vol. 3, no. 9, pp. 538–542, 2008.
- [9] K. S. Novoselov, A. K. Geim, S. V. Morozov et al., "Two-dimensional gas of massless Dirac fermions in graphene," *Nature*, vol. 438, no. 7065, pp. 197–200, 2005.
- [10] K. S. Novoselov, Z. Jiang, Y. Zhang et al., "Room-temperature quantum hall effect in graphene," *Science*, vol. 315, no. 5817, pp. 1379, 2007.

- [11] A. A. Balandin, S. Ghosh, W. Bao et al., "Superior thermal conductivity of single-layer graphene," *Nano Letters*, vol. 8, no. 3, pp. 902–907, 2008.
- [12] S. Ghosh, I. Calizo, D. Teweldebrhan et al., "Extremely high thermal conductivity of graphene: prospects for thermal management applications in nanoelectronic circuits," *Applied Physics Letters*, vol. 92, no. 15, Article ID 151911, 2008.
- [13] S. K. Srivastava, A. K. Shukla, V. D. Vankar, and V. Kumar, "Growth, structure and field emission characteristics of petal like carbon nano-structured thin films," *Thin Solid Films*, vol. 492, no. 1–2, pp. 124–130, 2005.
- [14] C. E. Hamilton, J. R. Lomeda, Z. Sun, J. M. Tour, and A. R. Barron, "High-yield organic dispersions of unfunctionalized graphene," *Nano Letters*, vol. 9, no. 10, pp. 3460–3462, 2009.
- [15] H. Jiang, "Chemical preparation of graphene-based nanomaterials and their applications in chemical and biological sensors," *Small*, vol. 7, no. 17, pp. 2413–2427, 2011.
- [16] S. Park and R. S. Ruoff, "Chemical methods for the production of graphenes," *Nature nanotechnology*, vol. 4, no. 4, pp. 217–224, 2009.
- [17] D. A. Dikin, S. Stankovich, E. J. Zimney et al., "Preparation and characterization of graphene oxide paper," *Nature*, vol. 448, no. 7152, pp. 457–460, 2007.
- [18] W. S. Hummers Jr. and R. E. Offeman, "Preparation of graphitic oxide," *Journal of the American Chemical Society*, vol. 80, no. 6, p. 1339, 1958.
- [19] S. Guo and S. Dong, "Graphene nanosheet: synthesis, molecular engineering, thin film, hybrids, and energy and analytical applications," *Chemical Society Reviews*, vol. 40, no. 5, pp. 2644–2672, 2011.
- [20] C. Zhu, S. Guo, Y. Fang, and S. Dong, "Reducing sugar: new functional molecules for the green synthesis of graphene nanosheets," *ACS Nano*, vol. 4, no. 4, pp. 2429–2437, 2010.
- [21] C. N. R. Rao, K. S. Subrahmanyam, H. S. S. Ramakrishna Matte, U. Maitra, K. Moses, and A. Govindaraj, "Graphene: synthesis, functionalization and properties," *International Journal of Modern Physics B*, vol. 25, no. 30, pp. 4107–4143, 2011.
- [22] S. D. Perera, R. G. Mariano, K. Vu et al., "Hydrothermal synthesis of graphene-TiO₂ nanotube composites with enhanced photocatalytic activity," *ACS Catalysis*, vol. 2, no. 6, pp. 949–956, 2012.
- [23] D. C. Marcano, D. V. Kosynkin, J. M. Berlin et al., "Improved synthesis of graphene oxide," *ACS Nano*, vol. 4, no. 8, pp. 4806–4814, 2010.
- [24] Z. J. Fan, K. Wang, T. Wei, J. Yan, L. P. Song, and B. Shao, "An environmentally friendly and efficient route for the reduction of graphene oxide by aluminum powder," *Carbon*, vol. 48, no. 5, pp. 1670–1692, 2010.
- [25] K. Zhou, Y. Zhu, X. Yang, X. Jiang, and C. Li, "Preparation of graphene-TiO₂ composites with enhanced photocatalytic activity," *New Journal of Chemistry*, vol. 35, no. 2, pp. 353–359, 2011.
- [26] Y. Zhang and C. Pan, "TiO₂/graphene composite from thermal reaction of graphene oxide and its photocatalytic activity in visible light," *Journal of Materials Science*, vol. 46, no. 8, pp. 2622–2626, 2011.
- [27] J. Shen, M. Shi, B. Yan, H. Ma, N. Li, and M. Ye, "Ionic liquid-assisted one-step hydrothermal synthesis of TiO₂-reduced graphene oxide composites," *Nano Research*, vol. 4, no. 8, pp. 795–806, 2011.
- [28] D. Mo and D.-Q. Ye, "Surface study of composite photocatalyst based on plasma modified activated carbon fibers with TiO₂," *Surface and Coatings Technology*, vol. 203, no. 9, pp. 1154–1160, 2009.
- [29] D. R. Dreyer, S. Park, C. W. Bielawski, and R. S. Ruoff, "The chemistry of graphene oxide," *Chemical Society reviews*, vol. 39, no. 1, pp. 228–240, 2010.
- [30] R. Bissessur and S. F. Scully, "Intercalation of solid polymer electrolytes into graphite oxide," *Solid State Ionics*, vol. 178, no. 11–12, pp. 877–882, 2007.
- [31] J. I. Parades, S. Villar-Rodil, A. Martínez-Alonso, and J. M. D. Tascón, "Graphene oxide dispersions in organic solvents," *Langmuir*, vol. 24, no. 19, pp. 10560–10564, 2008.
- [32] O. C. Compton and S. T. Nguyen, "Graphene oxide, highly reduced graphene oxide, and graphene: versatile building blocks for carbon-based materials," *Small*, vol. 6, no. 6, pp. 711–723, 2010.

Research Article

Second-Order Nonlinearity Assisted by Dual Surface Plasmon Resonance Modes in Perforated Gold Film

Renlong Zhou, Guozheng Nie, Lingxi Wu, Qiong Liu, Suxia Xie, Mengxiong Wu, Lisan Zeng, and Yingyi Xiao

School of Physics and Electronic Science, Hunan University of Science and Technology, Xiangtan 411201, China

Correspondence should be addressed to Renlong Zhou; rlzhou@mail.sitp.ac.cn

Received 29 November 2013; Accepted 12 January 2014; Published 20 February 2014

Academic Editor: Wen Lei

Copyright © 2014 Renlong Zhou et al. This is an open access article distributed under the Creative Commons Attribution License, which permits unrestricted use, distribution, and reproduction in any medium, provided the original work is properly cited.

We have studied analytically the reflection assisted with surface plasmon through the square lattice perforated gold film. Under the excitation of the external electromagnetic field with one or two different frequencies, the second-order nonlinearity exists in this noncentrosymmetric metal-based metamaterial. We employed the two surface plasmon resonances modes with different lattice periods. With the excitation of two different plasmon resonances modes, the strong local field induces an expected increase of the second-order nonlinearity including second harmonic generation as well as the sum (difference) frequency generation. The field distributions results also indicate that the enhancement of sum frequency signals and difference frequency signals strongly depends on surface plasmon resonance effect.

1. Introduction

The optical second harmonic generation (SHG) was first observed for the one-dimensional metal surfaces in 1965 [1]. The optical transmission of light through metal film has been shown to be orders of magnitude higher than that expected by the classical aperture theory due to the surface plasmon (SP) resonances [2–5]. The SHG in such a perforated metal film with different topographical nanoscale apertures has also been the focus of many researchers [6, 7]. Zeng et al. has found that the SHG effect mainly results from the convective derivative of the continuous electron current [7]. The enhanced linear fundamental field gives rise to the local SHG at the tip surface, thereby creating a highly confined photon source of SHG. The SHG efficiency has been enhanced in a circularly symmetric structure. It has been shown that the SHG is a symmetry-sensitive process. The arrangement of the nanoholes in a random way can break out the symmetry and has been found to favor SHG [8]. In addition, the less-symmetric double-hole array has been studied experimentally and found to cause the enhancement of SHG when the sharp tips are formed by folding the double holes [6]. The SHG has been also investigated in geometric

configurations such as split-ring resonators, T-shaped, and L-shaped nanoparticles [9–13].

For the ideally infinite metal surfaces, it is well known that the dominant second harmonic electric dipole source occurs only at the interface between centrosymmetric media, in which the inversion symmetry is broken. The higher order multipole sources merely provide a relatively small bulk SHG polarization density. On the other hand, for low-symmetric or even asymmetric nanoparticles, such as gold split-ring resonators, SHG dipolar polarizability may be presented in the whole volume and not limited at the interface. Consequently, the overall shape of the nanoparticles plays a significant role in determining the second harmonic response [14, 15]. In this paper, we have investigated the SHG, sum frequency generation (SFG), and difference frequency generation (DFG) from gold film with a periodic subwavelength air nanohole patterns by means of the three-dimensional (3D) finite-difference time-domain (FDTD) algorithm. The enhanced linear fundamental field causes the local second-order nonlinearity. Thereby the local SFG, DFG, and SHG can act as highly confined photon sources. The main results are shown as follows: (1) the reflection of the fundamental light results from the enhancement of the local field due to the SP

resonance effect and the strong local field induces an expected increase of second-order nonlinearity; (2) the electric field distributions of fundamental light and the nonlinear signals are different for different SP resonance modes.

2. Structure and Calculation Method

In the second-order nonlinearity of gold nanostructures, the classical theoretical method of the second-order nonlinearity calculation has been proposed in [7]. The interaction between light and Drude-type metal is generally described by the time-dependent Maxwell equations which are coupled to an equation that describes the light induced oscillation of quasifree electrons in the metal. The linear response of the gold nanostructures is given by [15]:

$$\begin{aligned} \frac{\partial B^{(1)}}{\partial t} &= -\nabla \times E^{(1)}, \\ \frac{\partial E^{(1)}}{\partial t} &= c^2 \nabla \times B^{(1)} - \frac{1}{\epsilon_0} j^{(1)}, \\ j^{(1)} &= -i\omega p^{(1)} = -i\omega \epsilon_0 (\epsilon_r - 1) E^{(1)}, \\ \frac{\partial j^{(1)}}{\partial t} &= -\gamma j^{(1)} + \frac{e^2 n_0}{m_e} E^{(1)}. \end{aligned} \quad (1)$$

The second-order nonlinearity of the gold film can be considered as follows:

$$\begin{aligned} \frac{\partial B^{(2)}}{\partial t} &= -\nabla \times E^{(2)}, \\ \frac{\partial E^{(2)}}{\partial t} &= c^2 \nabla \times B^{(2)} - \frac{1}{\epsilon_0} j^{(2)}, \\ j^{(2)} &= -i\omega p^{(2)} = -i\omega \epsilon_0 (\epsilon_r - 1) E^{(2)} + S^{(2)}, \\ \frac{\partial j^{(2)}}{\partial t} &= -\gamma j^{(2)} + \frac{e^2 n_0}{m_e} E^{(2)} + S^{(2)}, \\ S^{(2)} &= \sum_k \frac{\partial}{\partial r_k} \left(\frac{j^{(1)} j^{(1)}_k}{e n_0} \right) \\ &\quad - \frac{e}{m_e} \left[\epsilon_0 (\nabla \cdot E^{(1)}) E^{(1)} + j^{(1)} \times B^{(1)} \right]. \end{aligned} \quad (2)$$

Here, k represents the x , y , and z coordinates. $J^{(1)}$ and $J^{(2)}$ represent the current density vectors of fundamental and harmonic waves, respectively. $E^{(1)}$ and $E^{(2)}$, $B^{(1)}$ and $B^{(2)}$ are the electric field and magnetic flux intensity vectors of fundamental and harmonic waves, respectively. n_0 is the ion density, m_e is the electron mass, c the light speed in vacuum air, e is the elementary charge, and $S^{(2)}$ is the nonlinear source of the plasma for second-order nonlinearity, respectively. It includes three terms of different physical mechanisms. The first term represents a generalized divergence originating from the convective time derivative of the electron velocity field. The second and third terms are the electric and magnetic components of the Lorentz force, respectively [7].

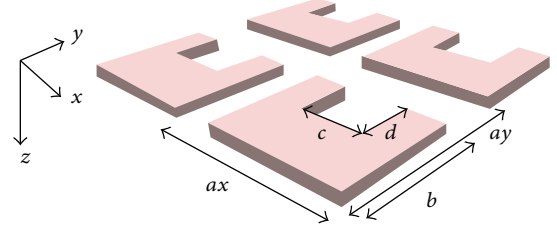


FIGURE 1: The structure of a perforated gold film with the thickness $h = 30.5$ nm and the lattice periods $a = ax = ay = 305$ nm. There has the unit cell shape with $b = 219$ nm, $c = 131$ nm, and $d = 97$ nm. The input light wave is polarized along the x direction and propagates along the z direction.

The permittivity $\epsilon_r(\omega)$ of the gold nanostructures has the form

$$\epsilon_r(\omega) = 1 - \frac{\omega_p^2}{\omega(\omega + i\gamma)}. \quad (3)$$

In the expression, the γ is the phenomenological collision frequency, and $\omega_p = \sqrt{e^2 n_0 / m_e \epsilon_0}$ is the bulk plasma frequency according to the well-known Drude model of gold. The bulk plasma frequency and phenomenological collision frequency of gold are taken as $\omega_p = 1.367 \times 10^{16} \text{ s}^{-1}$ and $\gamma = 6.478 \times 10^{13} \text{ s}^{-1}$, respectively. The permittivity $\epsilon_r(\omega)$ can become negative at frequencies below ω_p . The n_0 is the charge carrier concentration; m is the effective mass of the charge carriers.

The FDTD approach is applied for the numerical calculation of the above first-order and second-order equations. There are two computational loops for the calculations of the fundamental and second harmonic fields in the program. Yee's discretization scheme is utilized so that all electric and magnetic components can be defined in a cubic grid. The fields are temporally separated by a half time step and spatially interlaced by a half grid cell. The perfectly matched absorbing boundary conditions are employed at the below and top of the computational space along the z direction, and the periodic boundary conditions are used on the boundaries of x and y directions. Only one unit cell of the periodic holes array is considered in our computational space.

The structure of a perforated gold film is shown in Figure 1. The incident wave, polarized along the x direction, propagates along the z -axis which is generated by a total field/scattering field technique. Then, we calculate the temporal reflection of the fundamental light and second-order nonlinearity by considering the normal incident light on the perforated semiconductor film.

In our calculation, the size of the spatial cell is set as 3.05 nm. We consider the structure of a perforated gold film with the thickness $h = 30.5$ nm. The structure of a perforated gold film has a lattice constant $a = 305$ nm. The lattice constant is $ax = ay = 305$ nm along the x -axis and y -axis directions, respectively. There has the unit cell shape with $b = 219$ nm, $c = 131$ nm, and $d = 97$ nm. Each unit of the perforated gold film is noncentrosymmetric as shown

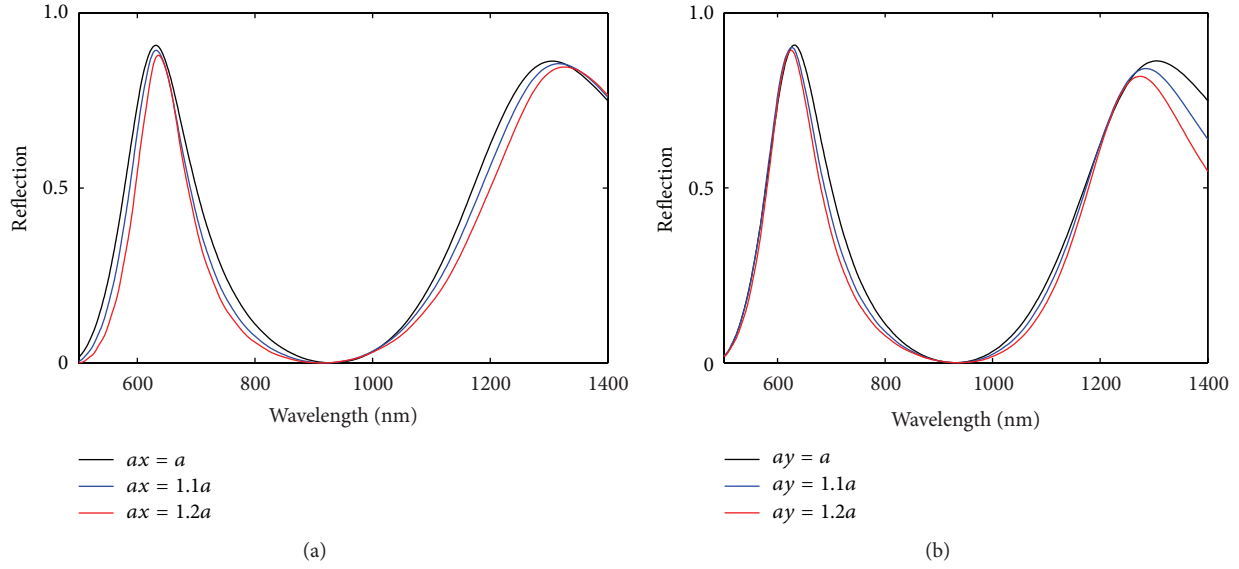


FIGURE 2: Reflection of FFW through a square lattice perforated gold film for lattice constant (a) along x direction $ax = a$ (black line), $1.1a$ (blue line), and $1.2a$ (red line), (b) along y direction $ay = a$ (black line), $1.1a$ (blue line), and $1.2a$ (red line), respectively.

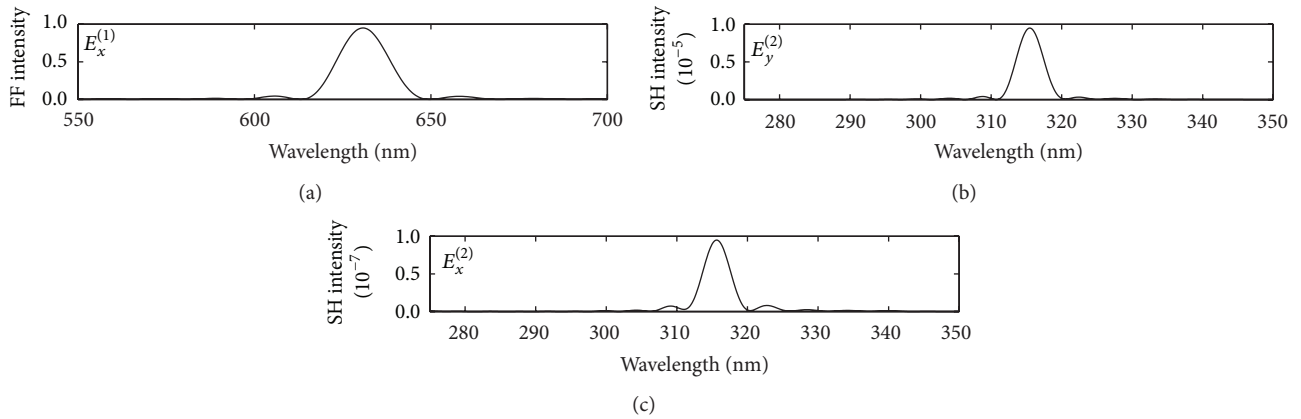


FIGURE 3: (a) The spectrum for $E_x^{(1)}$ component of FFW with wavelength 630 nm. The spectrum for (b) $E_y^{(2)}$ and (c) $E_x^{(2)}$ component of SHG with wavelength 315 nm.

in Figure 1. The input plane wave is polarized along the x direction by exciting a plane of identical dipoles in phase and propagates along the z direction.

3. Results and Discussions

First, the normalized reflection of fundamental frequency wave (FFW) through the square lattice perforated gold film for different lattice constants along x direction $ax = a$ (black line), $1.1a$ (blue line), and $1.2a$ (red line) is investigated here, and the calculation results are shown in Figure 2(a). There are two different SP resonance modes at the wavelengths 630 nm and 1295 nm for lattice constants $ax = a$ (black line). When the lattice constant along x direction increases while the holes shape is fixed, the short-wavelength SP resonance mode does not move significantly while the long-wavelength SP

resonance mode is blue-shifted dramatically. The normalized fundamental frequency wave reflection for different lattice constants along y direction $ay = 1.0a$, $1.1a$, and $1.2a$ is also shown in Figure 2(b). When the lattice constant along the y direction increases, the short-wavelength SP resonance mode does not move significantly while the long-wavelength SP resonance mode red-shifts slightly.

To obtain the SHG of the gold film with a periodic subwavelength air nanohole patterns, the incident FFW $E_x^{(1)}$ with wavelengths λ has the form $E_x^{(1)} = E_0 \sin(2\pi ct/\lambda)$, where E_0 is amplitude.

Under the continuous incident FFW $E_x^{(1)}$ with wavelengths $\lambda = 630$ nm, one can see spectrum of FFW with the resonance wavelength 630 nm in Figure 3(a). It is also shown that the SHG spectrum of the $E_y^{(2)}$ and $E_x^{(2)}$ with the wavelength 315 nm is shown in Figures 3(b)-3(c),

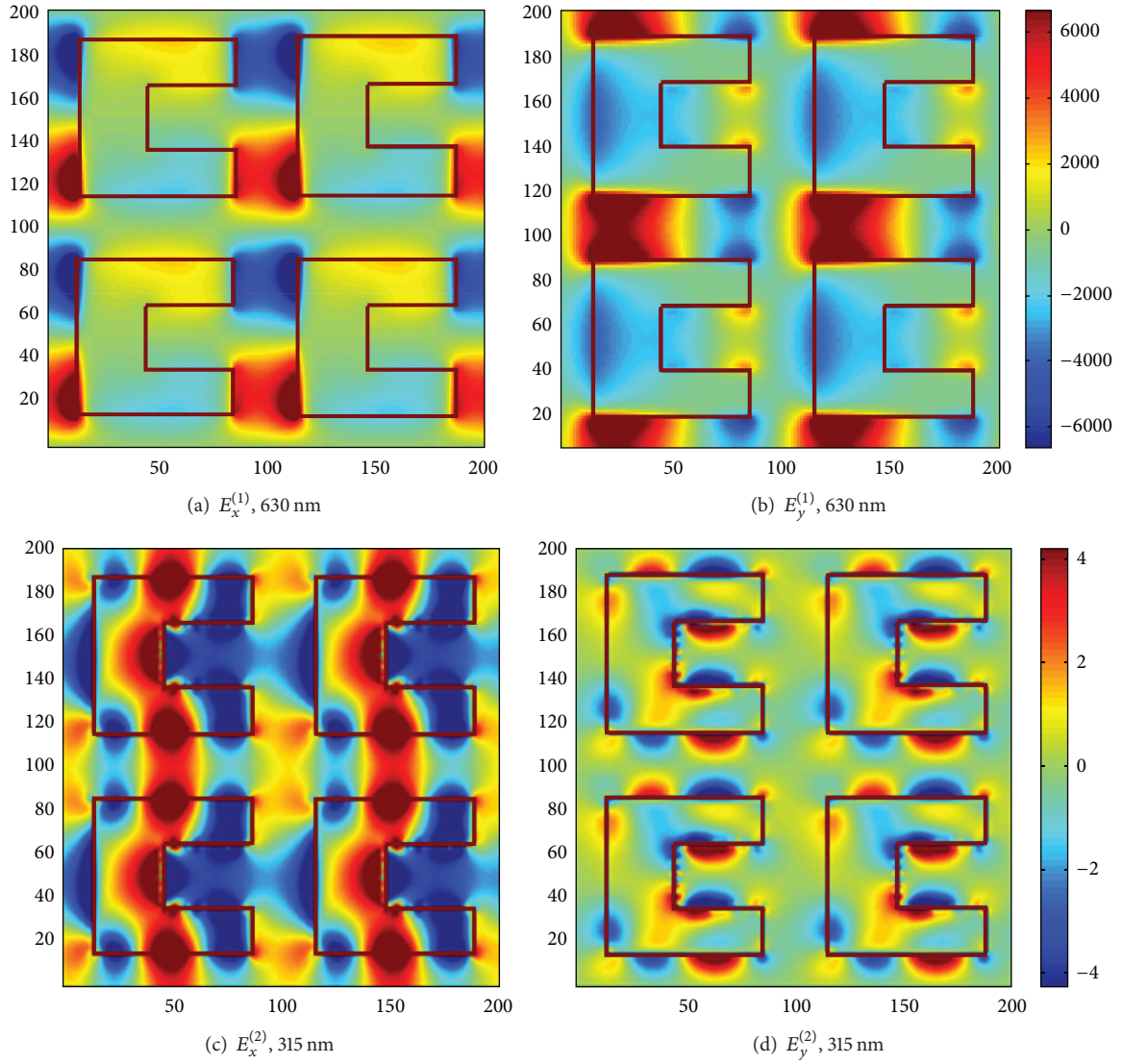


FIGURE 4: The electric field distribution of FFW (a) $E_x^{(1)}$ and (b) $E_y^{(1)}$, and electric field distribution of SHG (c) $E_x^{(2)}$ and (d) $E_y^{(2)}$ at wavelengths 630 nm and 315 nm, respectively.

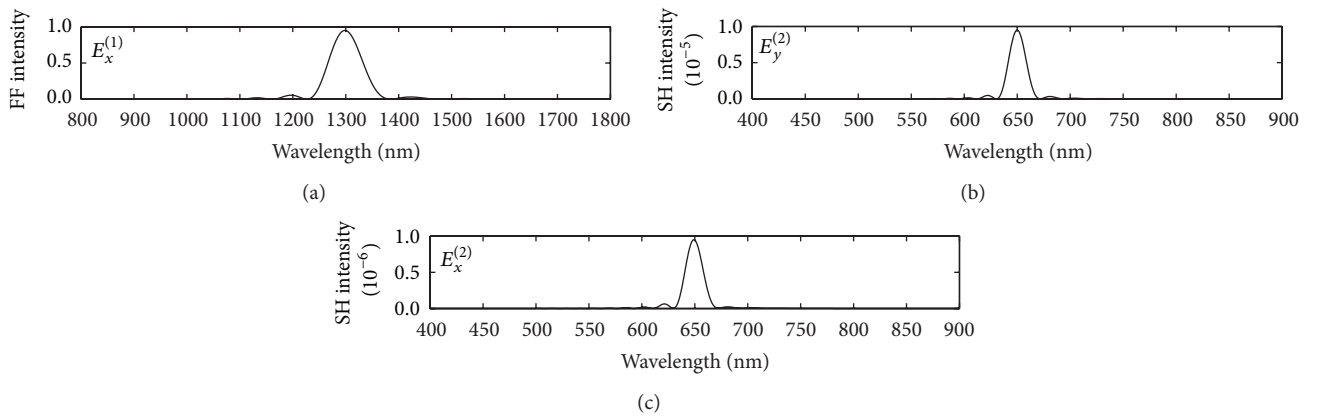


FIGURE 5: (a) The spectrum for $E_x^{(1)}$ component of fundamental frequency wave at the wavelength 1295 nm. Spectrum for (b) $E_y^{(2)}$ and (c) $E_x^{(2)}$ component of SHG at the wavelength 648 nm.

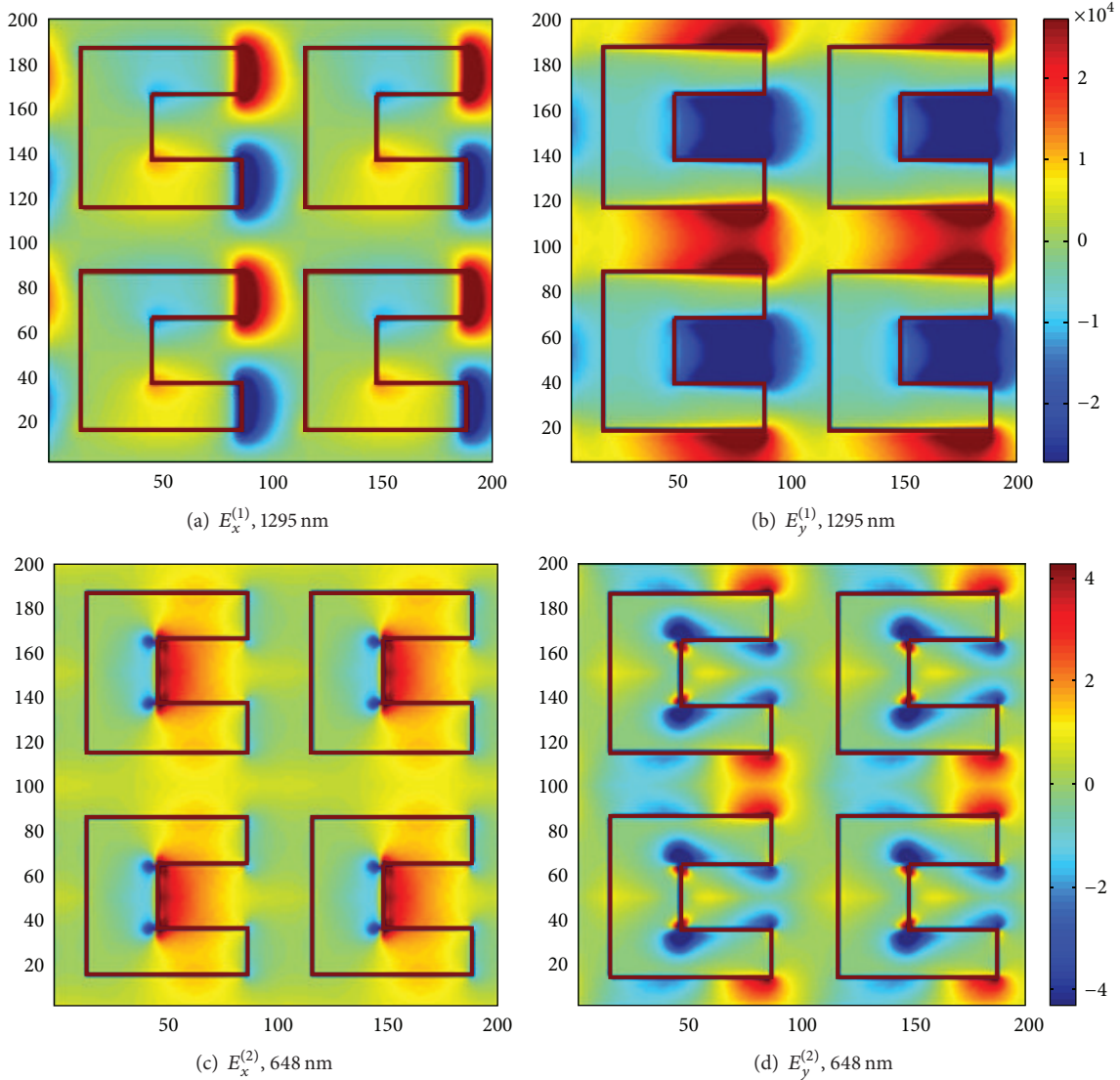


FIGURE 6: The electric field distribution of fundamental frequency field and second harmonic field above the gold film region at wavelengths 1295 nm and 648 nm, respectively.

respectively. The SHG conversion efficiencies η are defined in the second-order nonlinear optical process as the expression $|E^{(2)}(2\omega_0)/E^{(1)}(\omega_0)|^2$. Where ω_0 is the frequency of the incident FFW. The y -polarized SHG conversion efficiencies are about 10^{-5} while the x -polarized SHG conversion efficiencies is about 10^{-7} for the FFW at the wavelength 630 nm as shown in Figures 3(b)-3(c).

The transmission of the FFW results from an enhancement of the local field. The strong local field and non-centrosymmetry induces an increase of second harmonic nonlinearity signals. The electric field distribution of $E_x^{(1)}$ and $E_y^{(1)}$ for FFW above the gold film region at wavelengths 630 nm is also shown in Figures 4(a)-4(b), respectively. And the electric field distribution of $E_x^{(2)}$ and $E_y^{(2)}$ for SHG above the gold film region at wavelengths 315 nm is also shown in Figures 4(c)-4(d). It is noted that the different distribution

of fundamental frequency and second harmonic is shown in Figures 4(a)-4(d).

Under the continuous incident wave $E_x^{(1)}$ with wavelengths $\lambda = 1295$ nm, one can see spectrum of FFW at wavelength 648 nm is in Figure 5(a). It is also shown that the spectrum of the $E_y^{(2)}$ and the $E_x^{(2)}$ component of SHG at wavelength 648 nm in Figures 5(b)-5(c), respectively. The SHG conversion efficiencies for y polarization are about 10^{-5} while they are about 10^{-6} for x polarization at wavelength 1295 nm in Figures 6(b)-6(c). The electric field distribution of $E_x^{(1)}$ and $E_y^{(1)}$ for FFW above the gold film region at wavelengths 1295 nm is also shown in Figures 6(a)-6(b), respectively. The electric field distribution of $E_x^{(2)}$ and $E_y^{(2)}$ for SHG above the gold film region at wavelengths 648 nm is also shown in Figures 6(c)-6(d).

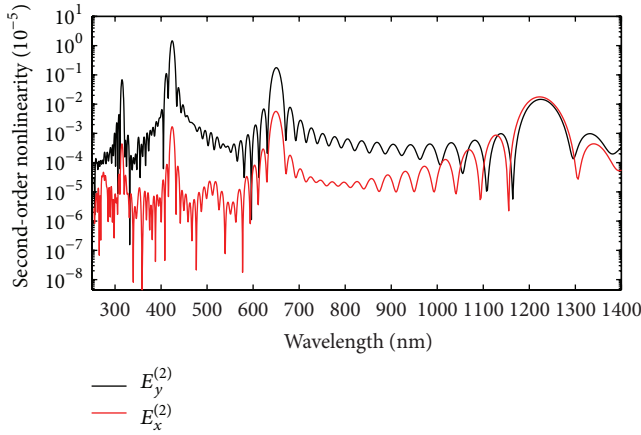


FIGURE 7: The spectrum of second-order nonlinearity signals at the wavelength 315 nm, 424 nm, 650 nm, and 1226 nm for the continuous incident wave $E_x^{(1)}$ with wavelengths $\lambda_1 = 630$ nm and $\lambda_2 = 1295$ nm, respectively.

Under the continuous incident wave $E_x^{(1)}$ with two different wavelengths $\lambda_1 = 630$ nm and $\lambda_2 = 1295$ nm, $E_x = E_0 \sin(2\pi ct/\lambda_1) + E_0 \sin(2\pi ct/\lambda_2)$, we can obtain the second-order nonlinearity including SHG as well as the sum (difference) frequency generation.

When continuous wave $E_x^{(1)}$ with two different wavelengths 630 nm and 1295 nm is incident, it is noted that there are four peaks for second-order nonlinearity at the wavelengths 315 nm, 424 nm, 650 nm, and 1226 nm in Figure 7, respectively. We find that the second-order nonlinearity modes at wavelengths 315 nm and 650 nm are obtained from the two incident continuous waves with wavelengths 630 nm and 1295 nm due to the SHG effect, respectively. The second-order nonlinearity mode at wavelength 424 nm is the sum frequency field signals for two incident continuous waves with wavelengths 630 nm and 1295 nm. And the SHG conversion efficiencies of sum frequency field signal for two FFW incidences are about 10^{-5} . The second-order nonlinearity mode at wavelength 1226 nm is the difference frequency field for two FFW waves with wavelengths 630 nm and 1295 nm. The transmission of the fundamental light results from an enhancement of the local field. The strong local field induces an increase of the four second-order nonlinearity signals.

According to the fundamental wave field and the second-order harmonic field analysis, it can be found that a significant interaction of light with the perforated gold film is the strong enhancement of localized field amplitude due to the SP resonance effect. The light propagation through the holes results in the enhancement of the second-order nonlinearity including second harmonic generation as well as the sum (difference) frequency generation.

4. Conclusions

We have investigated transmission assisted with surface plasmon through a perforated gold film. The enhanced transmission of the fundamental light results from an enhancement of

the local field. The strong local field induces a desired increase of the second-order nonlinearity including second harmonic generation as well as the sum (difference) frequency generation signals. The field distributions results also indicate that the enhancement of difference frequency signals strongly depends on the SP resonance effect. Importantly, we find that the SHG conversion efficiencies of SHG signal for one fundamental frequency wave incidence are about 10^{-5} . And we also find that the SHG conversion efficiencies of sum frequency field signal for two fundamental frequency wave incidences are about 10^{-5} .

Conflict of Interests

The authors declare that there is no conflict of interests regarding the publication of this paper.

Acknowledgments

This work was supported by the National Natural Science Foundation of China under Grant (11247003, 51175172) and Scientific Research Fund of Hunan Provincial Education Department (13C323). The authors would especially like to thank Dr. Yong Zeng of University of Arizona for the discussion of FDTD simulations.

References

- [1] F. Brown, R. E. Parks, and A. M. Sleeper, "Nonlinear optical reflection from a metallic boundary," *Physical Review Letters*, vol. 14, no. 25, pp. 1029–1031, 1965.
- [2] N. Guo, W. D. Hu, X. S. Chen, L. Wang, and W. Lu, "Enhanced plasmonic resonant excitation in a grating gated field-effect transistor with supplemental gates," *Optics Express*, vol. 21, no. 2, pp. 1606–1614, 2013.
- [3] L. Wang, W. Hu, J. Wang et al., "Plasmon resonant excitation in grating-gated AlN barrier transistors at terahertz frequency," *Applied Physics Letters*, vol. 100, no. 12, Article ID 123501, 2012.
- [4] W. D. Hu, L. Wang, X. S. Chen et al., "Room-temperature plasmonic resonant absorption for grating-gate GaN HEMTs in far infrared terahertz domain," *Optical and Quantum Electronics*, vol. 45, no. 7, pp. 713–720, 2013.
- [5] G. Li, X. Chen, B. Ni et al., "Fractal H-shaped plasmonic nanocavity," *Nanotechnology*, vol. 24, no. 20, Article ID 205702, 2013.
- [6] G. Li, X. Chen, O. Li et al., "A novel plasmonic resonance sensor based on an infrared perfect absorber," *Journal of Physics D*, vol. 45, no. 20, Article ID 205102, 2012.
- [7] Y. Zeng, W. Hoyer, J. Liu, S. W. Koch, and J. V. Moloney, "Classical theory for second-harmonic generation from metallic nanoparticles," *Physical Review B*, vol. 79, no. 23, Article ID 235109, 2009.
- [8] A. Nahata, R. A. Linke, T. Ishi, and K. Ohashi, "Enhanced nonlinear optical conversion from a periodically nanostructured metal film," *Optics Letters*, vol. 28, no. 6, pp. 423–425, 2003.
- [9] F. B. P. Niesler, N. Feth, S. Linden et al., "Second-harmonic generation from split-ring resonators on a GaAs substrate," *Optics Letters*, vol. 34, no. 13, pp. 1997–1999, 2009.
- [10] M. W. Klein, M. Wegener, N. Feth, and S. Linden, "Experiments on second- and third-harmonic generation from magnetic

- metamaterials: erratum,” *Optics Express*, vol. 16, no. 11, p. 8055, 2008.
- [11] M. W. Klein, C. Enkrich, M. Wegener, and S. Linden, “Second-harmonic generation from magnetic metamaterials,” *Science*, vol. 313, no. 5786, pp. 502–504, 2006.
- [12] S. Kujala, B. K. Canfield, M. Kauranen, Y. Svirko, and J. Turunen, “Multipole interference in the second-harmonic optical radiation from gold nanoparticles,” *Physical Review Letters*, vol. 98, no. 16, Article ID 167403, 2007.
- [13] B. K. Canfield, H. Husu, J. Laukkanen et al., “Local field asymmetry drives second-harmonic generation in noncentrosymmetric nanodimers,” *Nano Letters*, vol. 7, no. 5, pp. 1251–1255, 2007.
- [14] J. Nappa, G. Revillod, I. Russier-Antoine, E. Benichou, C. Jonin, and P. F. Brevet, “Electric dipole origin of the second harmonic generation of small metallic particles,” *Physical Review B*, vol. 71, no. 16, Article ID 165407, 2005.
- [15] Y. Zeng and J. V. Moloney, “Volume electric dipole origin of second-harmonic generation from metallic membrane with none centro symmetric patterns,” *Optics Letters*, vol. 34, no. 18, pp. 2844–2846, 2009.

Research Article

The Formation Site of Noninterfacial Misfit Dislocations in InAs/GaAs Quantum Dots

Shuai Zhou, Yumin Liu, Pengfei Lu, Lihong Han, and Zhongyuan Yu

State Key Laboratory of Information Photonics and Optical Communications, Institute of Information Photonics and Optical Communications, Beijing University of Posts and Telecommunications, P.O. Box 49 (Room 339), Beijing 100876, China

Correspondence should be addressed to Yumin Liu; microluiyumin@hotmail.com

Received 30 November 2013; Revised 7 January 2014; Accepted 7 January 2014; Published 16 February 2014

Academic Editor: Wen Lei

Copyright © 2014 Shuai Zhou et al. This is an open access article distributed under the Creative Commons Attribution License, which permits unrestricted use, distribution, and reproduction in any medium, provided the original work is properly cited.

Taking elastic anisotropy into consideration, we use a dislocation position dependent model to calculate the preferential formation site of noninterfacial 60° mixed dislocation segment in ellipsoid shaped InAs/GaAs quantum dots (QDs) which is observed in the experiment. From the result, it is clear that the positions near the right edge of the quantum dot are the energy favorable areas for the noninterfacial 60° mixed dislocations.

1. Introduction

In recent years, InAs/GaAs quantum dots have attracted tremendous attention in the field of nanosemiconductor [1–7] because of their great potential for device applications. The two most popular methods to fabricate such quantum dots are classical Stranski-Krastanow (S-K) growth [8] and droplet epitaxy growth [9, 10]. But for both the S-K growth and the droplet epitaxy, with the increasing deposition of InAs on GaAs(001) substrates, the quantum dots begin to release the elastic strain energy by misfit dislocations when their sizes reach a critical value. Because of the harmful effects of dislocations on device performance and reliability, the onset of dislocations in quantum dots must be understood so that devices can be fabricated in fully coherent regimes. The preferential formation sites of interfacial edge and mixed misfit dislocations have been considered theoretically [11]. However, recent reports presented evidence of misfit dislocations located above the island/substrate interface in both S-K-grown GaSb/GaAs(001) system and droplet epitaxy grown InAs/GaAs(001) quantum dots system [12, 13].

In this work, taking elastic anisotropy into consideration, the Finite Element Method (FEM) is used to simulate 3D dislocation position dependent models of noninterfacial dislocated InAs/GaAs quantum dots. The FEM is by far the most widely used numerical technique in science and engineering. It has been proved to be a useful tool in the

analysis of the strain and stress state, even for nanoscale materials [14–17]. The stress/strain field and the total elastic energy of InAs/GaAs quantum dots with interfacial and noninterfacial dislocations in different positions are calculated. Comparing the overall energy stored in the quantum dots with dislocations in different positions, we obtain the first nucleation place for the 60° mixed dislocation in quantum dots.

2. Model and Method

The isolated uncapped InAs/GaAs quantum dot heterostructure considered in this paper is shown in Figure 1. The reference point is set to be the left endpoint of the quantum dot in Figure 1. And dislocation positions at the plane perpendicular to the QD growth direction are expressed by “relative distance” ($=L/S$) which is a ratio of the distance from the reference point to dislocation with respect to the quantum dot base. In the calculation, the base diameter is set as constant which equals 20 nm and the height of the QD is 5 nm. The substrate is large enough compared to the QD. In our simulation, the Descartes coordinate is adopted. The x and y axis correspond to the $[-1-10]$ and $[1-10]$ directions, respectively, while QD growth is along the $[001]$ direction. The InAs quantum dot is assumed to be an ellipsoid shaped quantum dot which has been shown in Figure 1, respectively. Dislocation with line vector $[1-10]$ and the Burger's vector

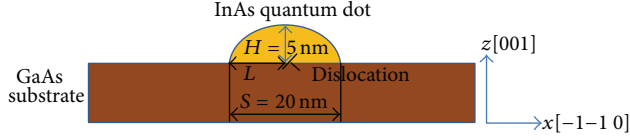


FIGURE 1: The cross section of ellipsoid shaped InAs quantum dots with GaAs substrate.

[01 - 1] for 60° mixed dislocation is produced when the quantum dot was big enough [15, 16]. The stiffness matrixes of InAs and GaAs materials in this case can be derived by tensor transformation [18] which has been shown in Tables 1 and 2.

In order to confirm the accuracy of the Finite Element Method, Gatti et al. [19] have already compared the elastic field of a dislocated island as found by FEM methodology with the same result calculated via atomistic simulations. And the good qualitative and quantitative correspondence is evident. So we use the FEM in this work directly and have not compared our results with the ones calculated via atomistic simulations.

We first consider the strain sources in the InAs quantum dot. After the onset of misfit dislocation, the strain from lattice mismatch and dislocation segment are exit simultaneously in the quantum dot. So we set both of them to be the initial strains in InAs quantum dot. The strain obtained from lattice mismatch can be expressed as $\epsilon_{ij}^0 = ((a_{\text{QD}} - a_{\text{sub}})/a_{\text{QD}})\delta_{ij}$ ($i, j = x, y, z$), where a_{QD} and a_{sub} are the lattice constants of the QD and substrate, respectively. For the strain $\epsilon_{ij}^{\text{dis}}$ from dislocation segment, nonsingular, self-consistent formulas [20] are used to simulate the strain field of dislocation segment which makes the strain remain finite everywhere, including on the dislocation lines themselves.

We then move on to the strain sources in GaAs substrate. Because the substrate is big enough, the strain from lattice mismatch can be ignored totally. The initial strain in GaAs substrate only comes from the dislocation segment.

In the calculation, the positions of the dislocation are changed by adjust the strain analytical formulas of dislocation segment. By assigning the proper conditions and reaching convergence, the solver can find the solution for the stress and strain fields directly. The total elastic energy in a volume V can be given by the well-known relation [21, 22]:

$$E = \frac{1}{2} \int (\sigma_{xx}\epsilon_{xx} + \sigma_{yy}\epsilon_{yy} + \sigma_{zz}\epsilon_{zz} + 2\sigma_{xy}\epsilon_{xy} + 2\sigma_{xz}\epsilon_{xz} + 2\sigma_{yz}\epsilon_{yz}) dV. \quad (1)$$

But because of the existence of the initial stresses in quantum dot and substrate, the total elastic energy in this model should be

$$E = \frac{1}{2} \int ((\epsilon_{xx} - \epsilon_{xx}^0 - \epsilon_{xx}^{\text{dis}})\sigma_{xx} + (\epsilon_{yy} - \epsilon_{yy}^0 - \epsilon_{yy}^{\text{dis}})\sigma_{yy} + (\epsilon_{zz} - \epsilon_{zz}^0 - \epsilon_{zz}^{\text{dis}})\sigma_{zz} + 2(\epsilon_{xy} - \epsilon_{xy}^0)\sigma_{xy} + 2(\epsilon_{xz} - \epsilon_{xz}^0)\sigma_{xz} + 2(\epsilon_{yz} - \epsilon_{yz}^0)\sigma_{yz}) dV, \quad (2)$$

TABLE 1: Stiffness matrix of InAs used in this work (unit GPa).

103.945	24.745	45.4	0	0	0
24.745	103.945	45.4	0	0	0
45.4	45.4	83.29	0	0	0
0	0	0	39.6	0	0
0	0	0	0	39.6	0
0	0	0	0	0	18.945

TABLE 2: Stiffness matrix of GaAs used in this work (unit GPa).

145.7	26.9	53.8	0	0	0
26.9	145.7	53.8	0	0	0
53.8	53.8	118.8	0	0	0
0	0	0	59.4	0	0
0	0	0	0	59.4	0
0	0	0	0	0	32.5

where the σ_{ij} and ϵ_{ij} ($i, j = x, y, z$) are the stress and strain calculated from the FEM solver; ϵ_{ij}^0 and $\epsilon_{ij}^{\text{dis}}$ ($i, j = x, y, z$) are the initial strain from lattice mismatch and dislocation segment.

Compared with other ways, this method avoids discontinuity at the dislocation core and can be extended to any specific material in the conditions of any shaped quantum dots and any types of dislocations with some care.

3. Results and Discussions

In this section, we adopt the energy criterion to predict the preferential formation site of misfit dislocations for the InAs quantum dot with GaAs substrate. By using the model and method mentioned above, we calculate the stress and strain fields of the quantum dot system with interfacial and noninterfacial 60° mixed dislocation segments located at different sites. The total energy of the quantum dot system can be obtained from (2).

Firstly, we calculated the strain energy of three different mixed dislocations which located at the island/QD interface, 0.5 nm and 1 nm above the interface. Variation of the energy, as a function of the “relative distance” in ellipsoid shaped InAs quantum dots, is shown in Figure 2(a). From the result, it is clear that the dislocations at interface are more energy favorable than the noninterfacial dislocations. It can explain the phenomenon that most of the misfit dislocations are located at the island/substrate interface. However, in some cases, the dislocations are observed located above the InAs/GaAs interface because of the surface oxidation of the material which resulted in the substrate surface moving down.

When the dislocation position along the QD growth direction is fixed, the most energy favourable position at the plane perpendicular to the QD growth direction is always at a “relative distance” 0.8 for the interfacial and noninterfacial mixed misfit dislocations. It means the positions near the edge of the quantum dot base are the energy favorable area for both interfacial and noninterfacial dislocations and

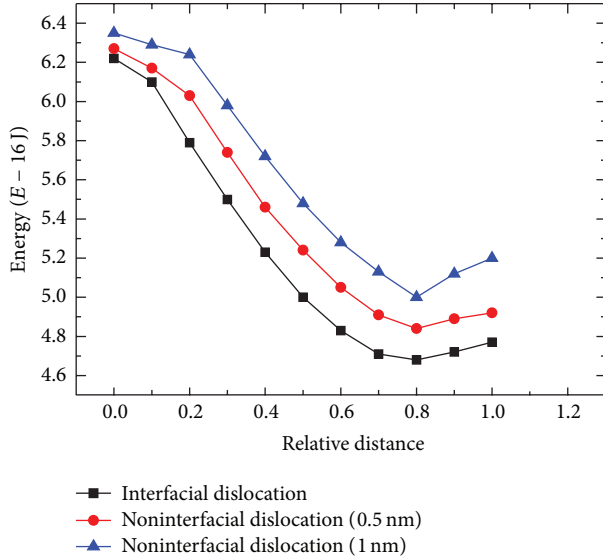


FIGURE 2: The relationship between energy and “relative distance” for 60° mixed dislocations located at island/substrate interface (black line), 0.5 nm (red line), and 1 nm (blue line) above the island/substrate interface, respectively.

island/substrate interface has little impact on the preferential position of dislocations at the plane perpendicular to the QD growth direction. This phenomenon may be because of the relative position of the dislocation is only related with the type of dislocation and the shape of the QD. The experiment result of reference [12] can support our result partly. From the TEM picture in reference [12] (Figure 1), we can see that one dislocation is located at the position of relative distance = 0.8.

In order to gain a clear idea of the most important factor which influences the dislocation preferential formation site of mixed dislocation at the plane perpendicular to the QD growth direction in InAs quantum dots, we decompose the 60° mixed dislocation into two edge dislocation components with Burgers vector $[110]$ and $[00 - 1]$, respectively, and a screw dislocation component with Burgers vector $[-110]$. The relationship between energy and “relative distance” for the three dislocation components of interfacial and noninterfacial misfit dislocations are shown in Figures 3–5. From Figure 3, it is clear that the most energy favourable position for screw dislocation is located near the edges of the QD. So it is very easy to draw the conclusion that the screw dislocation component always tends to slip out of the QD and it has a positive influence on mixed dislocation nucleate at edge of the QD. But since the screw dislocation cannot relax the strain and stress in quantum dots, it has a small effect on the 60° mixed dislocation preferential relative formation site. The main factors which influence the dislocation nucleation position are the two edge components. Owing to the fact that InAs quantum dot has a bigger lattice constant than GaAs substrate, compressive strain primarily exists in quantum dot; thus the two edge dislocation components must form at the positions which can relax the compressive strain in quantum dot most effectively. For the edge dislocation component with

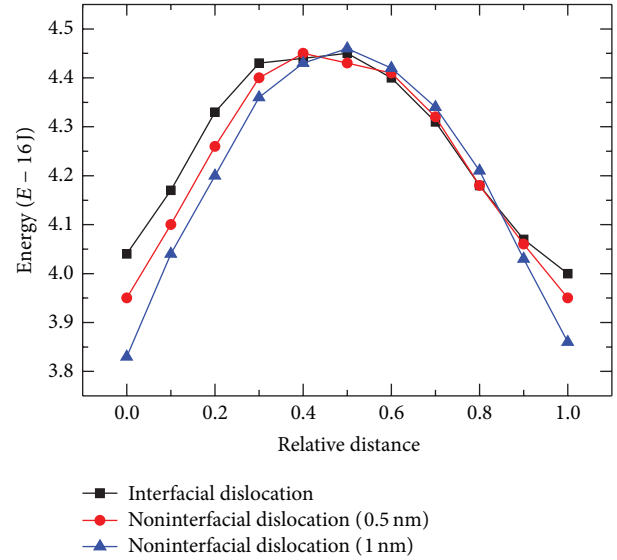


FIGURE 3: The relationship between energy and “relative distance” for screw dislocation component with Burgers vector $[-110]$ located at island/substrate interface (black line), 0.5 nm (red line), and 1 nm (blue line) above the island/substrate interface, respectively.

Burgers vector $[110]$ in Figure 4, it only exerts the tensile stress on quantum dot to balance out the compressive stress so that it firstly forms at the centre area of the island/quantum dot interface where the compressive stress reaches its maximum value. In the case of edge dislocation component with Burgers vector $[00 - 1]$ in Figure 5, it preferentially nucleates at the right margin inside the quantum dot and it is because of that position the edge dislocation can relax the compressive strain inside the quantum dot most effectively and can exert no compressive strain on the quantum dot. We should also note that when the Burgers vector of this edge dislocation component becomes $[001]$, the preferential nucleate site is at the left margin inside the quantum dot. So the 60° mixed dislocation preferential nucleation site at the plane perpendicular to the QD growth direction depends on a compromise of the two edge dislocation component formation areas.

Based on the analysis above, the 60° mixed dislocation will nucleate at the island/QD interface preferentially in common and positions near to the edge of the quantum dot base are the energy favorable areas for 60° mixed dislocations. In some special cases, the misfit dislocations can locate above the island/substrate interface, but the preferential relative position at the plane perpendicular to the QD growth direction of the mixed dislocation position is still the same.

4. Conclusion

In this paper, using FEM, 3D models have been built to predict the preferential formation site of dislocations in InAs/GaAs quantum dot system in the framework of elastic anisotropy. Based on the dislocation position dependent model, we calculate the stress/strain field and total elastic

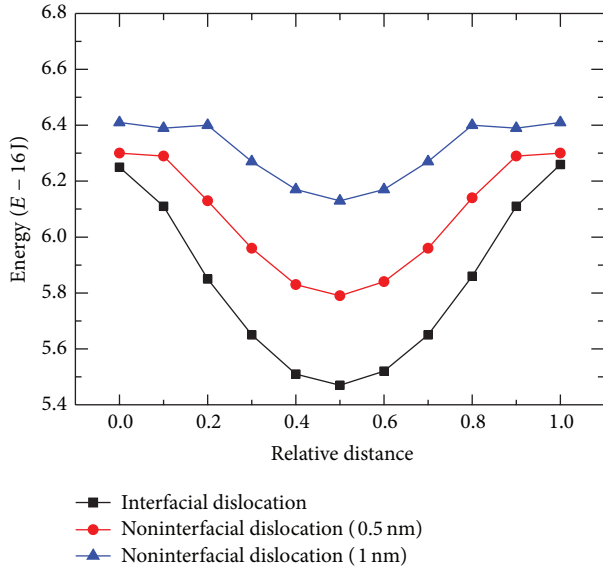


FIGURE 4: The relationship between energy and “relative distance” for edge dislocation component with Burgers vector $[110]$ located at island/substrate interface (black line), 0.5 nm (red line), and 1 nm (blue line) above the island/substrate interface, respectively.

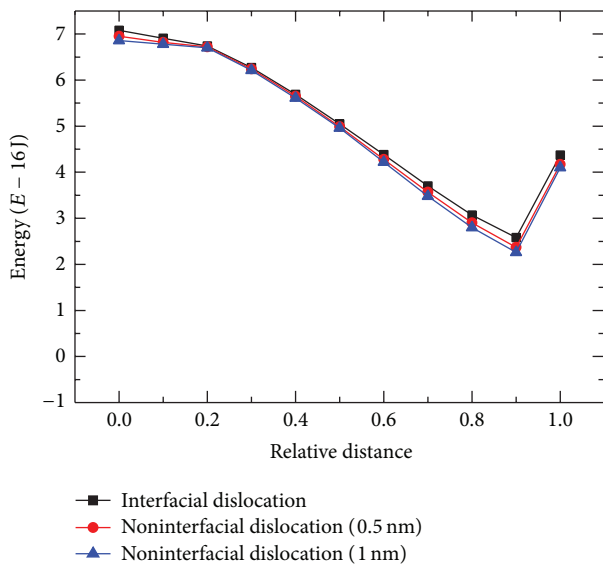


FIGURE 5: The relationship between energy and “relative distance” for edge dislocation component with Burgers vector $[00-1]$ located at island/substrate interface (black line), 0.5 nm (red line), and 1 nm (blue line) above the island/substrate interface, respectively.

energy of the different types of dislocations in InAs/GaAs quantum dot system. From the calculation, we found that the 60° mixed dislocation will nucleate at the island/QD interface preferentially in common. In some special cases, when the misfit dislocations located above the island/substrate interface, the preferential relative position of noninterfacial dislocation is the same as the interfacial one. Since once the dislocation position along the QD growth direction is fixed, the most important factors which influence the

relative position of mixed misfit dislocation are the two edge dislocation components of the mixed dislocation rather than the island/substrate interface.

Acknowledgments

This Project was supported by the National High Technology Research and Development Program of China (Grant no. 2009AA03Z405), the National Natural Science Foundation of China (Grant nos. 60908028, 60971068, and 10979065), the Program for New Century Excellent Talents in University of China (NCET-10-0261), and the Chinese Universities Scientific Fund (no. 2011RC0402).

Conflict of Interests

The authors declare that there is no conflict of interests.

References

- [1] V. M. Ustinov and A. E. Zhukov, “GaAs-based long-wavelength lasers,” *Semiconductor Science and Technology*, vol. 15, p. R41, 2000.
- [2] N. N. Ledentsov, A. R. Kovsh, A. E. Zhukov et al., “High performance quantum dot lasers on GaAs substrates operating in $1.5\ \mu\text{m}$ range,” *Electronics Letters*, vol. 39, no. 15, pp. 1126–1128, 2003.
- [3] L. Seravalli, P. Frigeri, G. Trevisi, and S. Franchi, “ $1.59\ \mu\text{m}$ room temperature emission from metamorphic InAs/InGaAs quantum dots grown on GaAs substrates,” *Applied Physics Letters*, vol. 92, no. 21, pp. 213104–213106, 2008.
- [4] I. Tãngringa, H. Q. Ni, B. P. Wu et al., “ $1.58\ \mu\text{m}$ InGaAs quantum well laser on GaAs,” *Applied Physics Letters*, vol. 91, no. 22, pp. 221101–221103, 2007.
- [5] Y. M. Liu, Z. Y. Yu, and Y. Z. Huang, “The strain distributions and carrier’s confining potentials of self-organized InAs/GaAs quantum dot,” *International Journal of Modern Physics B*, vol. 20, no. 29, pp. 4899–4907, 2006.
- [6] H. Ye, P. F. Lu, Z. Y. Yu, and L. H. Han, “Critical lateral dimension for a nanoscale-patterned heterostructure using the finite element method,” *Semiconductor Science and Technology*, vol. 24, no. 2, Article ID 025029, 2009.
- [7] Y. M. Liu, Z. Y. Yu, and X. M. Ren, “The strain relaxation of InAs/GaAs self-organized quantum dot,” *Chinese Physics B*, vol. 18, no. 3, pp. 881–887, 2009.
- [8] K. Yamaguchi, K. Yujobo, and T. Kaizu, “Stranski-Krastanov growth of InAs quantum dots with narrow size distribution,” *Japanese Journal of Applied Physics*, vol. 39, no. 12, pp. L1245–L1248, 2000.
- [9] T. Manoa, K. Watanabea, S. Tsukamotoa, H. Fujiokab, M. Oshimab, and N. Koguchia, “Fabrication of InGaAs quantum dots on GaAs(0 0 1) by droplet epitaxy,” *Journal of Crystal Growth*, vol. 209, no. 2-3, pp. 504–508, 2000.
- [10] T. Manoa, K. Watanabea, S. Tsukamotoa, H. Fujiokab, M. Oshimab, and N. Koguchia, “New self-organized growth method for InGaAs quantum dots on GaAs(001) using droplet epitaxy,” *Japanese Journal of Applied Physics*, vol. 38, pp. 1009–1011, 1999.
- [11] S. Zhou, Y. Liu, D. Wang et al., “The preferential formation site of dislocations in InAs/GaAs quantum dots,” *Superlattices and Microstructures*, vol. 51, no. 1, pp. 53–61, 2012.

- [12] Z. B. Chen, W. Lei, B. Chen et al., “Can misfit dislocations be located above the interface of InAs/GaAs (001) epitaxial quantum dots?” *Nanoscale Research Letters*, vol. 7, article 486, 2012.
- [13] Y. H. Kim, J. Y. Lee, Y. G. Noh, M. D. Kim, and J. E. Oh, “High-resolution transmission electron microscopy study on the growth modes of GaSb islands grown on a semi-insulating GaAs (001) substrate,” *Applied Physics Letters*, vol. 90, p. 241915, 2007.
- [14] Y. M. Liu, Z. Y. Yu, X. M. Ren, and Z. H. Xu, “Intensity modulation characters of orthogonally polarized HeNe lasers with different optical feedback level,” *Chinese Physics B*, vol. 17, no. 2, p. 3471, 2008.
- [15] Z. Mi, J. Yang, P. Bhattacharya, and D. L. Huffaker, “Self-organised quantum dots as dislocation filters: the case of GaAs-based lasers on silicon,” *Electronics Letters*, vol. 42, no. 2, pp. 121–123, 2006.
- [16] J. Yang, P. Bhattacharya, and Z. Mi, “High-performance $\text{In}_{0.5}\text{Ga}_{0.5}\text{As}$ /GaAs quantum-dot lasers on silicon with multiple-layer quantum-dot dislocation filters,” *IEEE Transactions on Electron Devices*, vol. 54, no. 11, pp. 2849–2855, 2007.
- [17] O. Brandt, K. Ploog, R. Bierwolf, and M. Hohenstein, “Break-down of continuum elasticity theory in the limit of monatomic films,” *Physical Review Letters*, vol. 68, no. 9, pp. 1339–1342, 1992.
- [18] Y. M. Liu, Z. Y. Yu, X. M. Ren, and Z. H. Xu, “Intensity modulation characters of orthogonally polarized HeNe lasers with different optical feedback level,” *Chinese Physics B*, vol. 17, no. 2, pp. 3471–3478, 2008.
- [19] R. Gatti, A. Marzegalli, V. A. Zinovyev, F. Montalenti, and L. Miglio, “Modeling the plastic relaxation onset in realistic SiGe islands on Si(001),” *Physical Review B*, vol. 78, no. 18, Article ID 184104, 2008.
- [20] W. Cai and A. Aresnlis, “A non-singular continuum theory of dislocations,” *Journal of the Mechanics and Physics of Solids*, vol. 54, no. 3, pp. 561–587, 2006.
- [21] H. Ye, P. Lu, Z. Yu, B. Jia, H. Feng, and Y. Liu, “Equilibrium critical size of coherent InSb/GaSb quantum dot,” *Physica E*, vol. 42, no. 9, pp. 2402–2405, 2010.
- [22] J. P. Hirth and J. Lothe, *Theory of Dislocations*, Wiley, New York, NY, USA, 1982.

Research Article

Mixed Phases at the Bottom Interface of Si-Doped AlGa_N Epilayers of Optoelectronic Devices

Chen-hui Yu,¹ Qing-zhou Luo,² Xiang-dong Luo,¹ and Pei-sheng Liu¹

¹ Jiangsu Key Laboratory of ASIC Design, Nantong University, Nantong 226019, China

² School of Remote Sensing, Nanjing University of Information Science and Technology, Nanjing 210044, China

Correspondence should be addressed to Chen-hui Yu; ychntu@126.com

Received 17 December 2013; Accepted 7 January 2014; Published 13 February 2014

Academic Editor: Wen Lei

Copyright © 2014 Chen-hui Yu et al. This is an open access article distributed under the Creative Commons Attribution License, which permits unrestricted use, distribution, and reproduction in any medium, provided the original work is properly cited.

This paper presents an analysis of crystalline structures of Si-doped Al_{0.4}Ga_{0.6}N layers grown on not-intentionally doped AlGa_N buffer layer with an AlN nucleation layer by metal organic chemical vapor deposition. Weak cubic Al_{0.4}Ga_{0.6}N (002) and (103) reflection peaks are observed in high-resolution XRD $\theta/2\theta$ scans and cubic Al_{0.4}Ga_{0.6}N (LO) mode in Raman scattering spectroscopy. These cubic subgrains are localized at the bottom interface of Si-doped layer due to the pulsed lower growth temperature and rich hydrogen atmosphere at the start of silane injection. Their appearance has no direct relationship with the buffer and nucleation layer. This study is helpful not only to understand fundamental properties of high aluminum content Si-doped AlGa_N alloys but also to provide specific guidance on the fabrication of multilayer optoelectronic devices where weak cubic subgrains potentially occur and exert complicated influences on the device performance.

1. Introduction

GaN and its alloys (e.g., AlGa_N, InAlN, and InGa_N) are foundations for new optoelectronic devices such as blue/violet light-emitting diode (LED), high electron mobility transistor (HEMT), ultraviolet and/or infrared photodetectors, and plasmonic Terahertz detectors [1–7]. Ga_N usually exists in either a hexagonal wurtzite (*h*) or a cubic zinc blende (*c*) structure [1, 2, 8, 9]. Devices based on the two crystalline structures show very different optical and electrical performances. The emitting peak or optical response wavelength is different for the different bandgap energy E_g of *c*-Ga_N and *h*-Ga_N. The mobility of electrons and holes in a *c*-Ga_N film is intrinsically higher than that in a *h*-Ga_N layer due to lower phonon scattering in cubic crystals [8]. However, more electron and hole traps may appear in film with a mixture of *c*- and *h*-Ga_N for the stacking faults among the two kinds of crystalline subgrains [10]. The coexistence of the two crystalline structures in a single film is possible for the proximity of their formation energies. Therefore, it is of great importance to understand and control the occurrence of these crystalline structures. Previous works have demonstrated that, in not-intentionally doped (NID)

GaN layers, an obvious lower substrate temperature is necessary to obtain a pure cubic phase rather than that of a pure hexagonal phase by metal organic chemical vapor deposition (MOCVD) or molecular-beam epitaxy (MBE) [8, 11–13]. Recently, uniformly distributed *c*-Ga_N and *h*-Ga_N subgrains have been simultaneously found in NID Ga_N nucleation layers grown on sapphire substrate. Both subgrains provide templates for the subsequent epitaxial growth, having important influence on the crystalline quality of Ga_N [9, 12, 14]. However, few studies have examined the possible mixed crystalline structures in doped AlGa_N alloys with high aluminum content.

In the present work, we report simultaneous observations of cubic and hexagonal subgrains in a group of silicon doped (Si-doped) AlGa_N epilayers. We have designed and grown those Si-doped Al_{0.4}Ga_{0.6}N samples by MOCVD. High-resolution X-ray diffraction (XRD) and Raman spectroscopy are employed to analyze their crystalline structures. The possible reasons for the occurrence of weak cubic subgrains in the epilayers are discussed. Our experimental results are quite different from previous work in that the coexistence of cubic and hexagonal subgrains occurs in a group of Si-doped Al_{0.4}Ga_{0.6}N epilayers. Moreover, the cubic subgrains

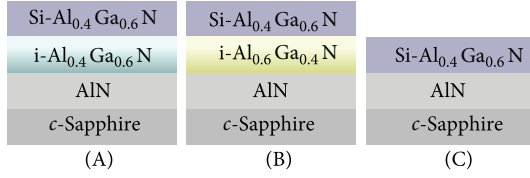
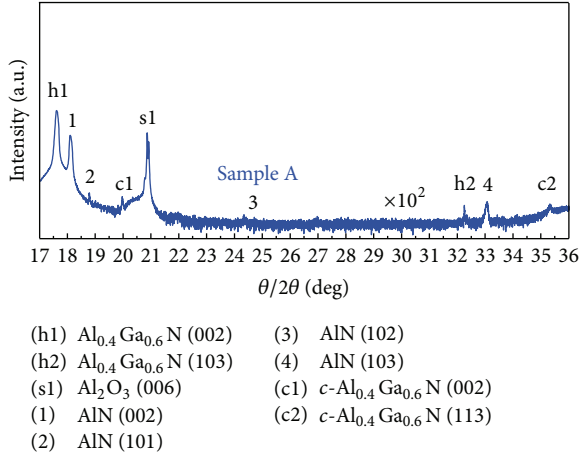


FIGURE 1: Schematic diagram of samples A, B, and C.

FIGURE 2: XRD $\theta/2\theta$ patterns of Si-doped Al_{0.4}Ga_{0.6}N epilayer, sample A, from 17° to 36°.

observed are locally distributed at the bottom interface of epilayers. These results are meaningful to the growth and understanding of multiple-interface GaN-based optoelectronic devices such as quantum well photodetectors and LEDs.

2. Experimental

Samples studied in this work were grown at a low pressure by an in-house developed MOCVD system. The geometric structure of sample A was Si-doped Al_{0.4}Ga_{0.6}N/NID Al_{0.4}Ga_{0.6}N (buffer layer)/AlN (nucleation layer) on a sapphire substrate as shown in Figure 1. The AlN nucleation layer was a bilayer structure with its first layer grown at a low temperature of about 750°C to initiate nucleation, followed by a second layer at a high temperature of about 1050°C to achieve 2D growth. The NID Al_{0.4}Ga_{0.6}N buffer layer and Si-doped Al_{0.4}Ga_{0.6}N layer were prepared at a temperature of about 1000°C. Two control samples, B and C, were also prepared for comparison and analysis. The geometric structures of B and C were almost the same as A except that the buffer layer of B was a NID Al_{0.6}Ga_{0.4}N layer instead and C had no buffer layer at all. All samples were crack-free showing good crystalline qualities.

XRD measurements, with Cu K α 1 ($\lambda = 1.54056 \text{ \AA}$) as a source, were performed to analyze dislocations, crystalline phase, subgrain orientation, and so forth. The room temperature Raman scattering spectra were obtained using

a LabRam HR800UV Raman spectrometer (Horiba Jobin-Yvon) fitted with a confocal microscope and a cooled charge-coupled device (CCD) detector. Samples were excited with the 514.5 nm green line of a Spectra Physics Ar⁺ laser focused under a microscope within a diameter of the analyzed spot around 1.0 μm . Raman scattering is a noncontact and non-destructive spectroscopic technology [9, 12, 15]. Raman spectroscopy and XRD measurements have been used together to investigate the crystalline structures in GaN-based thin film heterostructures comprehensively.

3. Results and Discussion

A high-resolution XRD $\theta/2\theta$ scan of sample A is shown in Figure 2. During the measurement, the power of the X-ray generator in the range from 17° to 23° remained at 40 kV and 10 mA but was increased to 40 kV and 40 mA in other ranges. Though this power increase induced a slight noise variance, it was helpful for the effective detection of much weaker reflected signals. Besides the strong Al₂O₃ (006) peak at around 20.80° from sapphire substrate, other reflection peaks could be grouped into three series [16, 17]. The first series are (002), (101), (102), and (103) reflection peaks from the hexagonal AlN nucleation layer. The second series are (002) and (103) peaks from the hexagonal Al_{0.4}Ga_{0.6}N layers. This indicates the dominant role of the hexagonal crystalline structure in the samples.

Two much weaker peaks at about 19.9° and 35.3° are observed as shown in Figure 3. They are obviously different from any possible reflections from AlN, GaN, substrate and hexagonal Al_{0.4}Ga_{0.6}N, even when the considerable stress effect and experimental errors are taken into account. These remaining peaks have little possibility to be satellite peaks either. Satellite peaks usually occur as continuous oscillating structures and multiorder peaks should be observed simultaneously. By comparing with previous works on pure cubic and mixed-phase GaN-based alloys, we attribute these two peaks to the cubic Al_{0.4}Ga_{0.6}N (002) and (113) reflection, respectively, which are indeed the two most intense signals in XRD measurement on cubic GaN-based alloys [11, 18, 19]. The cubic Al_{0.4}Ga_{0.6}N (002) and (113) reflection peaks have also been observed in control samples B and C. In summary, both hexagonal and weak cubic Al_{0.4}Ga_{0.6}N subgrains coexist in these epilayers.

The Raman spectra of Si-doped Al_{0.4}Ga_{0.6}N films shown in Figure 4 were recorded in a back-scattering configuration from the growth surface with a laser beam propagating parallel to the *c* axis of substrate. The inset shows the whole Raman spectra of sample A from 220 cm⁻¹ to 980 cm⁻¹. Several peaks labeled with S originating from the sapphire substrate are observed at about 751 cm⁻¹ and in the region from 380 cm⁻¹ to 450 cm⁻¹ [12]. Hexagonal AlN E₂ (low), AlN E₂ (high), and AlN A₁ (LO) modes are also observed at 249 cm⁻¹, 751 cm⁻¹, and 886 cm⁻¹, respectively [15, 20]. The intense peak at 582 cm⁻¹ is an overlapped structure with broad width including signals from sapphire, *h*-AlGa_{0.6}N E₂ (high) mode, and so forth. The active *h*-Al_{0.4}Ga_{0.6}N (LO) mode appears at 822 cm⁻¹. These features show the dominant

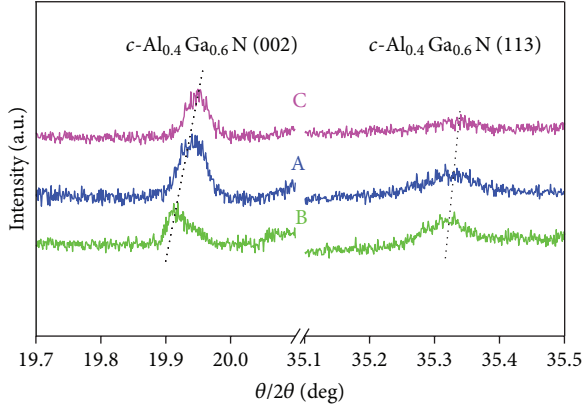


FIGURE 3: Comparison of XRD $\theta/2\theta$ patterns of sample A and control samples B and C. Cubic $\text{Al}_{0.4}\text{Ga}_{0.6}\text{N}$ (002) and (103) reflection peaks are clearly observed. Dotted lines are used for visual aid.

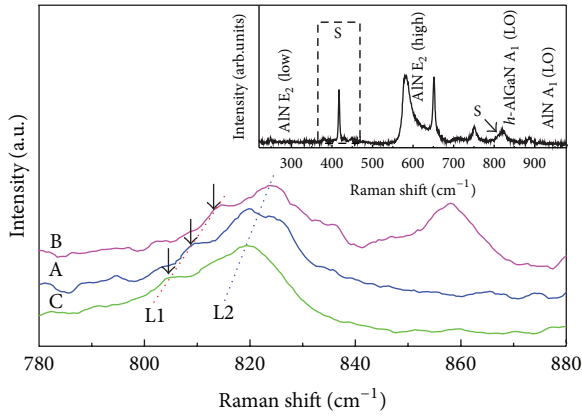


FIGURE 4: Raman spectra of Si-doped $\text{Al}_{0.4}\text{Ga}_{0.6}\text{N}$ epilayers. Inset is Raman spectra of sample A from 220 cm^{-1} to 980 cm^{-1} . Dotted lines L1 and L2 are used for visual aid. Cubic $\text{Al}_{0.4}\text{Ga}_{0.6}\text{N}$ (LO) modes are observed.

role of hexagonal crystalline structure in these epilayers. Meanwhile, a weak shoulder (L1) to lower wave number side of $h\text{-Al}_{0.4}\text{Ga}_{0.6}\text{N}$ (LO) mode (L2) is also clearly resolved at about 810 cm^{-1} . This weak shoulder, also reported in earlier studies, is attributed to the $c\text{-Al}_{0.4}\text{Ga}_{0.6}\text{N}$ (LO) mode [13, 21]. In most cases, the $c\text{-AlGa}\text{N}$ (TO) mode, which is nominally forbidden but becomes allowed due to any short range perturbations, should be detected simultaneously as the LO mode. In this study, no $c\text{-Al}_{0.4}\text{Ga}_{0.6}\text{N}$ (TO) mode was found in the Raman spectra. This discrepancy is due to two factors: (i) the otherwise $c\text{-Al}_{0.4}\text{Ga}_{0.6}\text{N}$ (TO) mode at about 606 cm^{-1} couples strongly with the intense and broad peak at 582 cm^{-1} and (ii) the TO mode of cubic phase is fairly weak under the excitation with a 514.5 nm laser line [21]. The $c\text{-Al}_{0.4}\text{Ga}_{0.6}\text{N}$ (LO) modes have been also observed in the Raman spectra of control samples B and C, shown in Figure 4. The results of Raman and XRD measurements are in good agreement and confirm the coexistence of hexagonal and weak cubic subgrains in the Si-doped $\text{Al}_{0.4}\text{Ga}_{0.6}\text{N}$ epilayers.

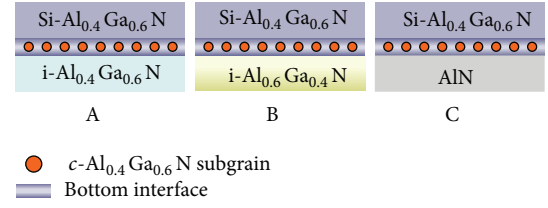


FIGURE 5: Distribution of cubic $\text{Al}_{0.4}\text{Ga}_{0.6}\text{N}$ subgrains at the bottom interface of Si-doped epilayers.

The favored growth conditions for hexagonal wurtzite and cubic zinc blende structures in MOCVD epitaxy are considerably different. The coexistence of hexagonal and cubic GaN-based alloys could only be found in special environments. For example, a frequently mentioned film is GaN nucleation layers deposited at a low temperature of about 600°C [9, 12]. In our case, an AlN nucleation layer instead is adopted and no cubic AlN subgrains have been detected by either XRD or Raman measurements. Then, an interesting question is raised as to where the cubic $\text{Al}_{0.4}\text{Ga}_{0.6}\text{N}$ subgrains are located. We could find answers through a layer-by-layer analysis. Firstly, both the sapphire substrate and the AlN nucleation layers have no relationship with the occurrence of cubic $\text{Al}_{0.4}\text{Ga}_{0.6}\text{N}$ subgrains. Secondly, cubic subgrains are independent of the $\text{Al}_{0.4}\text{Ga}_{0.6}\text{N}$ buffer layer. The hexagonal $\text{Al}_{0.4}\text{Ga}_{0.6}\text{N}$ buffer layer is grown solely in sample A. The buffer layer in sample B is replaced with an $h\text{-Al}_{0.6}\text{Ga}_{0.4}\text{N}$ layer. In sample C, no buffer layer is prepared at all. In spite of this diversity, characteristic features from cubic $\text{Al}_{0.4}\text{Ga}_{0.6}\text{N}$ subgrains have been observed in all the three samples. Then, we could claim that the occurrence of cubic $\text{Al}_{0.6}\text{Ga}_{0.4}\text{N}$ has no correlation with the buffer layer. In fact, we did perform measurements on single $\text{Al}_{0.4}\text{Ga}_{0.6}\text{N}$ buffer layer grown on AlN buffer layer and no characteristic features of cubic subgrains have been observed in either XRD or Raman measurements. Earlier literatures also indicate that there is little chance to find cubic subgrains in NID AlGaIn epilayers grown under similar epitaxy conditions as this work [22]. Thus, the occurrence of cubic $\text{Al}_{0.6}\text{Ga}_{0.4}\text{N}$ subgrains is undoubtedly related to the growth of Si-doped $\text{Al}_{0.4}\text{Ga}_{0.6}\text{N}$ layers.

These cubic subgrains have two possible existing forms in films. The first one is an even distribution. However, characteristic features from cubic subgrains in our Si-doped $\text{Al}_{0.4}\text{Ga}_{0.6}\text{N}$ layer are particularly weak in both XRD and Raman measurements. In addition, few researchers, including us, have reported cubic signals in thick Si-doped AlGaIn layers grown at a high temperature of about 1000°C . Then, the possibility of uniform distribution could be excluded. The second form is a local distribution at the bottom interface between buffer layer and the Si-doped layer as shown in Figure 5. This situation could be understood from the point of view of growth environments. Previous works indicate that a higher growth temperature and a rich nitrogen atmosphere favor the growth of hexagonal GaN-based alloys, while a lower growth temperature and a rich hydrogen atmosphere are beneficial to the occurrence of cubic subgrains [8].

At the onset of doping, silane (doping agent) carried by high room temperature hydrogen fluxes was instantaneously injected into the reaction chamber of in-house developed MOCVD, leading to a quick decrease of reaction temperature and a relatively high percentage of nitrogen atmosphere, and subsequently results in the occurrence of weak cubic subgrains. With the increase in processing time, the reaction temperature and atmosphere recover and the pure hexagonal crystalline phase becomes the sole structure again. This is why the cubic subgrains occur locally at the bottom interface of Si-doped layers. Meanwhile, interstitial silicon atoms in the Si-doped layers increase the deformation of the hexagonal crystalline lattice and cubic structure in GaN-based alloys resulting in a deformed hexagonal lattice with stacking faults in alternative layers [9]. Then, the interstitial silicon atoms are the possible reason for the occurrence of cubic subgrains. The morphology and microstructure of these weak cubic subgrains at the interface will be considered in further works.

4. Summary and Conclusions

In summary, we have investigated the crystalline structures of Si-doped $\text{Al}_{0.4}\text{Ga}_{0.6}\text{N}$ layers grown with an AlN nucleation layer by MOCVD. We have also observed cubic $\text{Al}_{0.4}\text{Ga}_{0.6}\text{N}$ (002) and (103) reflection peaks in high-resolution XRD $\theta/2\theta$ scans and cubic $\text{Al}_{0.4}\text{Ga}_{0.6}\text{N}$ (LO) mode in Raman scattering spectroscopy, as well as the specific features from hexagonal wurtzite structure of $\text{Al}_{0.4}\text{Ga}_{0.6}\text{N}$. It is found that the cubic subgrains are localized at the bottom interface of Si-doped layer due to the pulsed lower growth temperature and rich hydrogen atmosphere at the start of silane injection. This study is helpful not only to understand of fundamental properties of GaN-based alloys, but also to provide specific guidance on the growth of multilayer optoelectronic devices such as LED, HEMT, and quantum well photo-detector, where weak cubic subgrains potentially occur at the multiply interfaces and exert complicated influences on the device performances.

Conflict of Interests

All authors declare that there is no conflict of interests regarding the publication of this paper.

Acknowledgments

The authors thank James Torley from the University of Colorado at Colorado Springs for critical reading of the paper. This work was supported in part by the National Natural Science Foundation of China (Grant nos. 11104150, 11274330, and 41001288) and the Natural Science Foundation of Jiangsu Province of China (Grant no. 10KJA140043).

References

- [1] Q. Y. Wei, T. Li, J. Y. Huang et al., "Free carrier accumulation at cubic AlGaIn/GaN heterojunctions," *Applied Physics Letters*, vol. 100, no. 14, Article ID 142108, 2012.

- [2] E. A. DeCuir Jr., M. O. Manasreh, E. Tschumak, J. Schörmann, D. J. As, and K. Lischka, "Cubic GaNAlN multiple quantum well photodetector," *Applied Physics Letters*, vol. 92, no. 20, Article ID 201910, 2008.
- [3] W. D. Hu, X. S. Chen, Z. J. Quan, C. S. Xia, W. Lu, and H. J. Yuan, "Demonstration and dynamic analysis of trapping of hot electrons at gate edge model for current collapse and gate lag in GaN-based high-electron-mobility transistor including self-heating effect," *Applied Physics Letters*, vol. 89, no. 24, Article ID 243501, 2006.
- [4] X. Wang, W. Hu, X. Chen, and W. Lu, "The study of self-heating and hot-electron effects for AlGaIn/GaN double-channel HEMTs," *IEEE Transactions on Electron Devices*, vol. 59, no. 5, pp. 1393–1401, 2012.
- [5] N. Guo, W. D. Hu, X. S. Chen, L. Wang, and W. Lu, "Enhanced plasmonic resonant excitation in a grating gated field-effect transistor with supplemental gates," *Optics Express*, vol. 21, pp. 1606–1614, 2013.
- [6] W. D. Hu, L. Wang, X. S. Chen et al., "Room-temperature plasmonic resonant absorption for grating-gate GaN HEMTs in far infrared terahertz domain," *Optical and Quantum Electronics*, vol. 45, pp. 713–720, 2013.
- [7] C. H. Yu, Q. Z. Luo, X. D. Luo, and P. S. Liu, "Donor-like surface traps on two-dimensional electron gas and current collapse of AlGaIn/GaN HEMTs," *The Scientific World Journal*, vol. 2013, Article ID 931980, 6 pages, 2013.
- [8] B. M. Shi, M. H. Xie, H. S. Wu, N. Wang, and S. Y. Tong, "Transition between wurtzite and zinc-blende GaN: an effect of deposition condition of molecular-beam epitaxy," *Applied Physics Letters*, vol. 89, no. 15, Article ID 151921, 2006.
- [9] J. Narayan, P. Pant, A. Chugh, H. Choi, and J. C. C. Fan, "Characteristics of nucleation layer and epitaxy in GaN/sapphire heterostructures," *Journal of Applied Physics*, vol. 99, no. 5, Article ID 054313, 2006.
- [10] M. S. Yi, H. H. Lee, D. J. Kim et al., "Effects of growth temperature on GaN nucleation layers," *Applied Physics Letters*, vol. 75, no. 15, pp. 2187–2189, 1999.
- [11] T. Frey, D. J. As, M. Bartels et al., "Structural and vibrational properties of molecular beam epitaxy grown cubic (Al, Ga)N/GaN heterostructures," *Journal of Applied Physics*, vol. 89, no. 5, pp. 2631–2634, 2001.
- [12] A. Hushur, M. H. Manghnani, and J. Narayan, "Raman studies of GaN/sapphire thin film heterostructures," *Journal of Applied Physics*, vol. 106, no. 5, Article ID 054317, 2009.
- [13] H. F. Liu, H. Chen, Z. Q. Li et al., "MBE growth and Raman studies of cubic and hexagonal GaN films on (001)-oriented GaAs substrates," *Journal of Crystal Growth*, vol. 218, no. 2, pp. 191–196, 2000.
- [14] P. Pant, J. Narayan, A. Wushuer, and M. H. Manghnani, "Comparative Raman and HRTEM study of nanostructured GaN nucleation layers and device layers on sapphire (0001)," *Journal of Nanoscience and Nanotechnology*, vol. 8, no. 11, pp. 5985–5992, 2008.
- [15] V. Lughy and D. R. Clarke, "Defect and stress characterization of AlN films by Raman spectroscopy," *Applied Physics Letters*, vol. 89, no. 24, Article ID 241911, 2006.
- [16] J. Y. Li, X. L. Chen, Z. Y. Qiao, Y. G. Cao, M. He, and T. Xu, "Synthesis of aligned gallium nitride nanowire quasi-arrays," *Applied Physics A*, vol. 71, no. 3, pp. 349–350, 2000.
- [17] A. Artieda, M. Barbieri, C. S. Sandu, and P. Murali, "Effect of substrate roughness on c-oriented AlN thin films," *Journal of Applied Physics*, vol. 105, no. 2, Article ID 024504, 2009.

- [18] R. Armitage, K. Nishizono, J. Suda, and T. Kimoto, "Mechanism of stabilization of zincblende GaN on hexagonal substrates: insight gained from growth on ZrB₂ (0001)," *Journal of Crystal Growth*, vol. 284, no. 3-4, pp. 369–378, 2005.
- [19] X. H. Zheng, Y. T. Wang, Z. H. Feng et al., "Method for measurement of lattice parameter of cubic GaN layers on GaAs (001)," *Journal of Crystal Growth*, vol. 250, no. 3-4, pp. 345–348, 2003.
- [20] V. Y. Davydov, Y. E. Kitaev, I. N. Goncharuk et al., "Phonon dispersion and Raman scattering in hexagonal GaN and AlN," *Physical Review B*, vol. 58, no. 19, pp. 12899–12907, 1998.
- [21] A. Tabata, R. Enderlein, J. R. Leite et al., "Comparative Raman studies of cubic and hexagonal GaN epitaxial layers," *Journal of Applied Physics*, vol. 79, no. 8, pp. 4137–4140, 1996.
- [22] F. A. Ponce, J. S. Major Jr., W. E. Plano, and D. F. Welch, "Crystalline structure of AlGa_{0.2}N epitaxy on sapphire using AlN buffer layers," *Applied Physics Letters*, vol. 65, no. 18, pp. 2302–2304, 1994.

Research Article

Nonnegative Matrix Factorization Numerical Method for Integrated Photonic Cavity Based Spectroscopy

Zhengyu Huang,^{1,2} Dayuan Xiong,³ Guixu Zhang,² Yiqin Shi,¹
Changning Hao,¹ and Junli Duan¹

¹ Department of Gerontology, Xinhua Hospital, Shanghai Jiaotong University, Shanghai 200092, China

² Department of Computer Science, East China Normal University, 500 Dongchuan Road, Shanghai 200235, China

³ Key Laboratory of Polarized Materials and Devices, East China Normal University, Shanghai 200241, China

Correspondence should be addressed to Changning Hao; gilberthaocn@gmail.com and Junli Duan; duanjunlixh@163.com

Received 29 November 2013; Accepted 7 January 2014; Published 13 February 2014

Academic Editor: Wen Lei

Copyright © 2014 Zhengyu Huang et al. This is an open access article distributed under the Creative Commons Attribution License, which permits unrestricted use, distribution, and reproduction in any medium, provided the original work is properly cited.

Nonnegative matrix factorization numerical method has been used to improve the spectral resolution of integrated photonic cavity based spectroscopy. Based on the experimental results for integrated photonic cavity device on Optics Letters 32, 632 (2007), the theoretical results show that the spectral resolution can be improved more than 3 times from 5.5 nm to 1.8 nm. It is a promising way to release the difficulty of fabricating high-resolution devices.

1. Introduction

Miniature spectrometers are important for a wide variety of applications such as biomedical, chemical, remote sensing, and environmental engineering [1, 2]. The photonic device is the key to improve the performance of miniature spectrometer. One of the photonic devices is the wavelength division device. The integrated photonic cavity is one of the available options for wavelength division device. The integrated photonic cavity based wavelength division devices can match the detector completely and simplify the spectrometers extremely, which can leave the moving parts away and have very high reliability [1–5]. Moreover, the integrated photonic cavity based spectrometer has the ability to capture the target spectrum in real time, without any scanning time, which is an excellent property for certain specific applications especially in remote sensing, gas detection, biological, biochemical, geology exploring, and field investigating. It has been demonstrated that the integrated photonic cavity can be used to obtain a high spectral resolution by a chip with 128 filter channels [1, 2], which is one of the most promising miniature spectrometer types.

An interesting problem is to improve the spectral resolution by numerical model on this concept of high-resolution

miniature spectrometer. Since the filtering properties of the integrated photonic cavity may not be ideal, the transmission spectrum of each photonic cavity channel may have large ripples on pass- and stopbands and poor stopband attenuation [6]. Moreover, the transmission spectrum of each channel may overlap with each other and the peak intensity of each channel may differ. All of those problems will lead to the widening and deformation of input signal spectrum, which will reduce the spectral resolution of the integrated photonic cavity based spectrometer.

In order to improve the spectral resolution of the integrated photonic cavity, one method is to fabricate more narrowband integrated photonic cavity devices, but that is an extremely difficult and expensive work. Digital signal processing is another low-cost way to improve the spectral resolution. Several approaches have recently been exploited, such as sparse nature of signals [7], adaptive regularization [8], and filters with random transmittance [9].

As a new method for reconstruction of image, the nonnegative matrix factorization (NMF) has been developed, which uses nonnegativity constraints and results in a parts-based representation [10]. In this work, we will utilize NMF numerical method for spectrum reconstruction to improve the resolution of integrated photonic cavity based spectroscopy.

The experimental results of the chip integrated with 128 filter channels [1, 2] are used in our numerical calculation. The resolution improving effect has been investigated.

2. Simulation Models

Our goal is to investigate the effect in terms of resolution improvement by using NMF numerical method. Using the concept of high-resolution miniature spectrometer [1, 2], the mathematical description of experimental measurement can be expressed as

$$Y(\lambda_j) = \int T_j(\lambda) X(\lambda) d\lambda \approx \sum_i T_j(\lambda_i) X(\lambda_i) \Delta\lambda, \quad (1)$$

where λ is wavelength, $Y(\lambda_j)$ are the output signal spectrum measured by the miniature spectrometer, $T_j(\lambda_i)$ is the intrinsic transmission property of the j th channel filter in the 128-channel device which is measured by a standard precision spectrometer, and $X(\lambda_i)$ is the target spectrum, $j = 1, 2, 3, \dots, 128$.

For the whole wave band covered by integrated photonic cavity, from λ_1 to λ_{128} , the above integral can be discretized into a system of linear equations, which can be expressed in matrix form as follows:

$$\begin{bmatrix} Y_1 \\ Y_2 \\ \vdots \\ Y_i \\ \vdots \\ Y_n \end{bmatrix} = \begin{bmatrix} T_{11} & T_{12} & \cdots & T_{1j} & \cdots & T_{1m} \\ T_{21} & T_{22} & \cdots & T_{2j} & \cdots & T_{2m} \\ \vdots & \vdots & \vdots & \vdots & \vdots & \vdots \\ T_{i1} & T_{i2} & \cdots & T_{ij} & \cdots & T_{im} \\ \vdots & \vdots & \vdots & \vdots & \vdots & \vdots \\ T_{n1} & T_{n2} & \cdots & T_{nj} & \cdots & T_{nm} \end{bmatrix} \cdot \begin{bmatrix} X_1 \\ X_2 \\ \vdots \\ X_j \\ \vdots \\ X_m \end{bmatrix}. \quad (2)$$

For convenience, the above matrix form can be expressed as a concise form:

$$Y = T \times X, \quad (3)$$

where Y is a $n \times 1$ matrix, n is the numbers of channels, T is a $n \times m$ matrix, $m > n$ is an ill-conditioned matrix, m is the spectrum data point number of T and X , and X is a $m \times 1$ matrix.

From the point of digital signal processing, Y is the output signal, T is the transfer function, and X is the input signal. The reconstruction of the input signal is a linear inverse problem which we intend to solve. Since T is an ill-conditioned matrix, recovering the original input signal spectrum becomes a large discrete ill-posed problem. In fact, in this work, $m > n$, which means the output signal; has less detailed information than the input signal, so the spectrum reconstruction is an underdetermined systems. NMF numerical method is proposed to solve the problem and improve the resolution of integrated photonic cavity based spectroscopy.

In this work, we chose $m = 1990$, which is considerably larger than $n = 128$; so it is difficult to get X from measured Y and T matrix. Then NMF constructs approximate factorizations of the form $T \approx WH$ or

$$V_{iu} \approx (WH)_{iu} = \sum_{a=1}^r W_{ia} H_{au}. \quad (4)$$

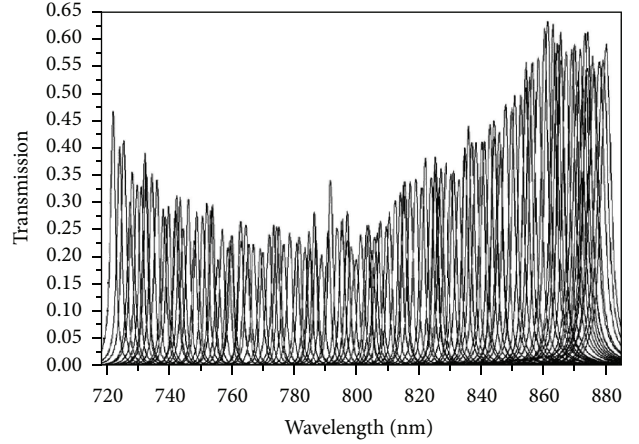


FIGURE 1: Experimental spectra of the 128-channel integrated filter array cited from [1, 2]. It is used to form matrix T .

The r columns of W are called basis spectra. Each column of H is called an encoding and is in one-to-one correspondence with a spectrum in T . An encoding consists of the coefficients by which the group of filter spectra represented by matrix T is represented with a linear combination of basis spectra. The dimensions of the matrix factors W and H are $n \times r$ and $r \times m$, respectively.

The rank r of the factorization is generally chosen so that $(n + m) \times r < n \times m$, and the product WH can be regarded as a compressed form of the data in T .

Obtaining the W and H , we can have the reconstructed spectrum X by Y and WH as follows:

$$X = \frac{1}{\Delta\lambda} T^{-1} Y = \frac{1}{\Delta\lambda} H^T (W^T T H^T)^{-1} W^T Y. \quad (5)$$

NMF numerical method does not allow negative entries in the matrix factors W and H . These non-negativity constraints permit the combination of multiple basis spectra to represent a spectrum. But only additive combinations are allowed, because the nonzero elements of W and H are all positive. Therefore, the non-negativity constraints are compatible with the intuitive notion of combining parts to form a whole, which is how NMF learns a parts-based representation.

3. Result and Discussion

The experimental spectral results of 128 integrated photonic cavities device reported by Wang et al. [1, 2] were chosen as the basis spectra of our model, which is the highest integration of filter array reported to our knowledge. The transmission spectra of 128 integrated photonic cavities device are shown in Figure 1. The matrix T in our calculation is generated from these spectra. The spectrum of every channel is one line in matrix T . Their passbands distribute in the range of 722.0 ~ 880.0 nm with a bandwidth from 1.7 to 3.8 nm and an average channel interval of 1.2 nm [1, 2]. The resolution limit is 5.5 nm.

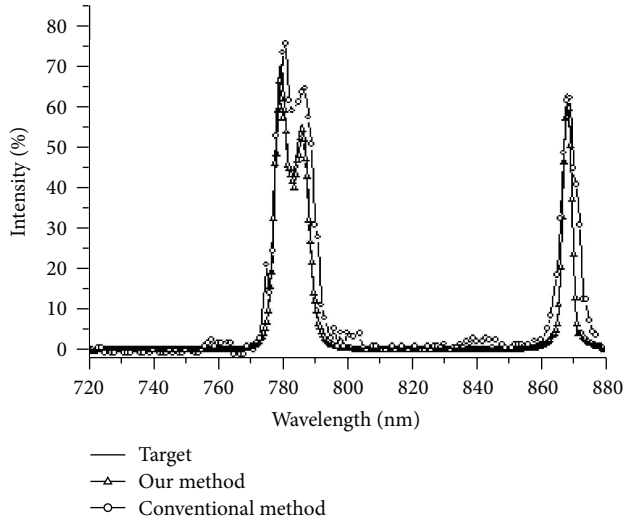


FIGURE 2: Comparison of resolution ability for integrated photonic cavity spectrometer itself [1, 2] and accompanied with our method.

To demonstrate the function of the NMF numerical method, we reconstruct the target spectrum on Optics Letters 32, 632 (2007) [1, 2] first. As shown in Figure 2 cited from Wang et al. 2007, the target spectrum (solid line) measured by a commercial Lambda 900 UV-Vis-NIR Spectrometer has two main feature structures; one is a two-peak structure with interval of 7 nm and another is a narrowband peak with FWHM (full width half maximum) of 3 nm. The conventional method used in the reference is normalization processing about the output spectrum from the 128-channel integrated filter array by the peak of each channel (line with empty circles). It is obvious that in the conventional method the spectrum was broadened and distorted, while the contrast of the two-peak structure was also attenuated. Using our NMF numerical method, the reconstructed spectrum (line with hollow triangles) is perfectly in agreement with the target spectrum, the FWHM of the narrowband peak is recovered to 3 nm, and the contrast of the two-peak structure is almost recovered too.

To evaluate the suitability of the NMF numerical method, several typical targets spectra with different structures were reconstructed by the NMF numerical method, including a typical two-peak structure spectrum, a typical fluorescence spectrum with sharp ascending and slowly descending branch, and a typical infrared transmission spectroscopy with characteristic absorption peaks. In Figures 3, 4, 5, and 6, “Target” is the input original target spectrum (solid line), “Our method” is reconstruction spectrum by the NMF numerical method (dash line with empty triangle), and “Conventional method” is normalization processing about the output spectrum from the 128-channel integrated filter array by the peak of each channel (line with empty circles). Contrastive analysis of the three curves was given as follows.

For a target spectrum with two-peak structure whose interval is 8 nm, both the integrated photonic cavity spectrometer itself and that accompanied with our method can distinguish two peaks as shown in Figure 3. Although the

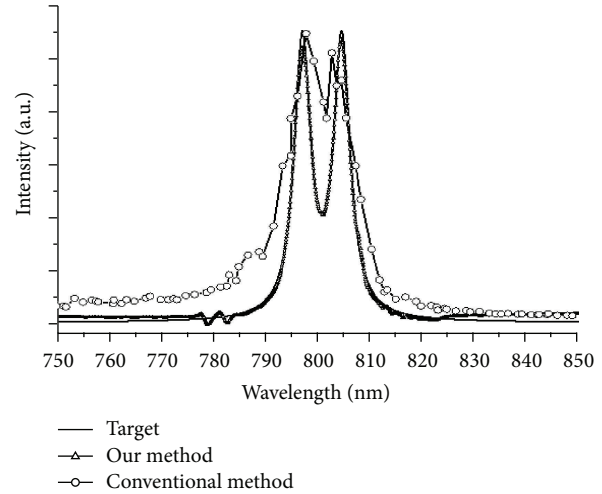


FIGURE 3: The reconstruction of a typical two-peak structure with interval of 8 nm.

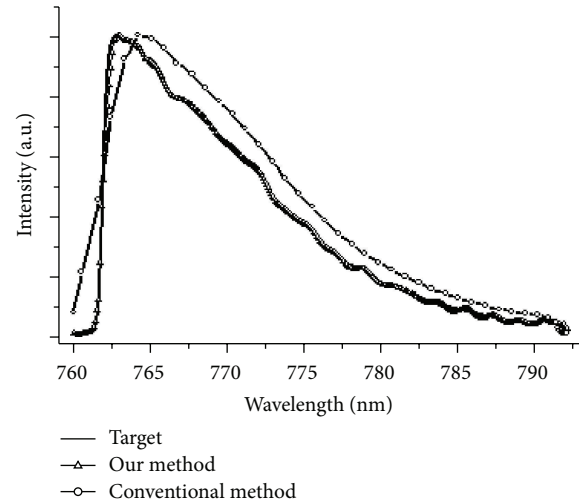


FIGURE 4: The reconstruction of a typical fluorescence spectrum with sharp edges and asymmetric peak structure.

above integrated filter array can distinguish two peaks, the measured spectrum is obviously distorted and the bandwidth is broadened for the sparse output signal data and limited spectral resolution. With the help of NMF numerical method, the spectral resolution is improved and more detail informations are recovered; so it becomes in good agreement between the original target spectrum (solid line) and reconstructed spectrum (line with hollow triangles); especially the bandwidth and contrast of the two-peak structure are improved obviously.

For a typical fluorescence spectrum with sharp ascending and slowly descending branch [11], as shown in Figure 4, since only 6 filter channels cover the sharp ascending branch, it was deformed to a gentle slope and the peak shape was also distorted by the conventional method (line with empty circles). Using our NMF numerical method, the spectral resolution is improved and more data points recovered in the

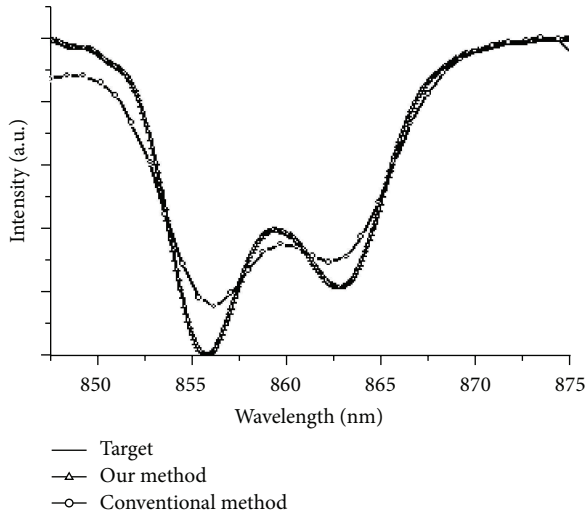


FIGURE 5: The reconstruction of a typical infrared transmission spectroscopy with characteristic absorption peaks.

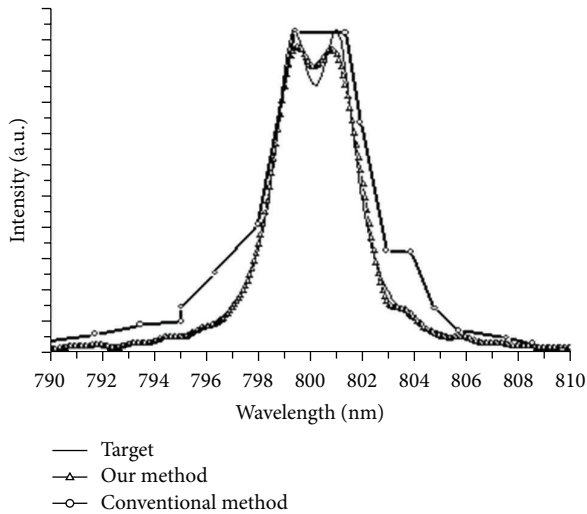


FIGURE 6: Comparison of resolution ability for target spectrum and the reconstructed spectrum by NMF method. The peak interval of the target is 1.8 nm.

reconstructed spectrum (line with hollow triangles), which becomes in good agreement with the original target spectrum (solid line).

Similarly, for a typical infrared transmission spectroscopy with characteristic absorption peaks, the filter channels covering the absorption peaks are limited, leading to serious information loss and distorted spectral structures. As shown in Figure 5, it can also be recovered by using NMF numerical method.

To evaluate the resolution limit of the 128 integrated photonic cavities device using NMF numerical method, a series of two-peak structure spectra with different interval were reconstructed, especially when the peak interval of target decreases to smaller than 5.5 nm, which is beyond the resolution limit of 128 integrated photonic cavities device

reported in [1, 2]; the integrated photonic cavity spectrometer itself cannot distinguish the two-peak structure any more. However, it can still be distinguished clearly with our method. We find that the resolution limit is extended to 1.8 nm by using NMF numerical method. As shown in Figure 3, two peaks with interval of 1.8 nm can still be distinguished by our method. The target spectrum and reconstructed spectrum are presented by black and red lines, respectively. The two peaks are clearly distinguished. However, the peak position and spectrum line shape around peak position have shown the observable error. These results indicate that the spectral resolution is improved from 5.5 nm to 1.8 nm in the aid of nonnegative matrix factorization.

4. Conclusion

In this work, NMF method has been used to improve the spectral resolution of integrated photonic cavity based spectroscopy. The numerical results show that it will agree with the original target better with the aid of NMF method. The spectral resolution can be improved from 5.5 nm to 1.8 nm, 3 times better than without the aid of NMF method.

Conflict of Interests

The authors declare that they have no conflict of interests regarding the publication of this paper.

Acknowledgments

This work was supported by the Shanghai Science and Technology Foundations (11nm0502100, 12nm0502900, and 11nm0503600) and partially supported by the National Nature Science Foundation of China (no. 61106092 and no. 11374213).

References

- [1] S. W. Wang, C. Xia, X. Chen et al., "Concept of a high-resolution miniature spectrometer using an integrated filter array," *Optics Letters*, vol. 32, no. 6, pp. 632–634, 2007.
- [2] S. W. Wang, M. Li, C. Xia, H. Wang, X. Chen, and W. Lu, "128 channels of integrated filter array rapidly fabricated by using the combinatorial deposition technique," *Applied Physics B*, vol. 88, no. 2, pp. 281–284, 2007.
- [3] S. W. Wang, X. Chen, W. Lu, L. Wang, Y. Wu, and Z. Wang, "Integrated optical filter arrays fabricated by using the combinatorial etching technique," *Optics Letters*, vol. 31, no. 3, pp. 332–334, 2006.
- [4] S. W. Wang, D. Liu, B. Lin, X. Chen, and W. Lu, "16 × 1 Integrated filter array in the MIR region prepared by using a combinatorial etching technique," *Applied Physics B*, vol. 82, no. 4, pp. 637–641, 2006.
- [5] S. W. Wang, D. Liu, B. Lin et al., "Realization of integrated narrow bandpass filters in the infrared region," *International Journal of Infrared and Millimeter Waves*, vol. 25, no. 11, pp. 1677–1683, 2004.
- [6] C. C. Chang, N. T. Lin, U. Kurokawa, and B. I. Choi, "Spectrum reconstruction for filter-array spectrum sensor from sparse

- template selection,” *Optical Engineering*, vol. 50, no. 11, Article ID 114402, 2011.
- [7] J. Oliver, W. Lee, S. Park, and H. N. Lee, “Improving resolution of miniature spectrometers by exploiting sparse nature of signals,” *Optics Express*, vol. 20, no. 3, pp. 2613–2625, 2012.
- [8] U. Kurokawa, B. I. Choi, and C. C. Chang, “Filter-based miniature spectrometers: spectrum reconstruction using adaptive regularization,” *IEEE Sensors Journal*, vol. 11, no. 7, pp. 1556–1563, 2011.
- [9] J. Oliver, W. B. Lee, and H. N. Lee, “Filters with random transmittance for improving resolution in integrated photonic cavity based spectroscopy,” *Optics Express*, vol. 21, no. 4, pp. 3969–3989, 2013.
- [10] D. D. Lee and H. S. Seung, “Learning the parts of objects by non-negative matrix factorization,” *Nature*, vol. 401, no. 6755, pp. 788–791, 1999.
- [11] W. Lu, Y. M. Mu, X. Q. Liu et al., “Direct observation of above-quantum-step quasibound states in GaAs/Al_xGa_{1-x}As/vacuum heterostructures,” *Physical Review B*, vol. 57, no. 16, pp. 9787–9791, 1998.

Research Article

Improving Light Outcoupling Efficiency for OLEDs with Microlens Array Fabricated on Transparent Substrate

Jun Wang, Weizhi Li, and Chong Wang

State Key Laboratory of Electronic Thin Films and Integrated Devices, School of Optoelectronic Information, University of Electronic Science and Technology of China, Chengdu, Sichuan 610054, China

Correspondence should be addressed to Jun Wang; uestc_wj@yahoo.com

Received 23 October 2013; Accepted 23 December 2013; Published 12 January 2014

Academic Editor: Wen Lei

Copyright © 2014 Jun Wang et al. This is an open access article distributed under the Creative Commons Attribution License, which permits unrestricted use, distribution, and reproduction in any medium, provided the original work is properly cited.

Low light outcoupling efficiency restricts the wide application of organic light-emitting diodes in solid state light market although the internal quantum efficiency of the device could reach near to 100%. In order to improve the output efficiency, different kinds of microlens array on the substrate emission surface were designed and simulated using light tracing method. Simulation results indicate that the microlens array on the substrate could efficiently improve the light output efficiency and an enhancement of 1.8 could be obtained with optimized microlens structure design. The microlens array with semicircle shape using polymer material was fabricated on glass substrate by a facile approach. Finally, the organic device with microlens array substrate was manufactured and the light output of the device with surface microlens structure could increase to 1.64 times comparing with the device without microlens.

1. Introduction

Due to high power efficiency, simple fabrication processes, and wide-color covering, organic light-emitting diodes (OLEDs) are the focus of attentions in applications of display and solid state lighting [1, 2]. Because of the difference among the refractive indices of the substrate, anode, organic materials, and the air, two wave guiding phenomena become obvious in the anode/organic layers and substrate/air layers of OLEDs [3]. Only 20% of the total emitted light from the organic layers can escape into the front side of substrate to form useful emission [4, 5]. Therefore the greatest potential for enhancing OLEDs external efficiency is to improve the light outcoupling from substrate.

Many different approaches had been done with the aim of optimizing the light outcoupling for OLEDs, including low-index grids [6, 7], periodic corrugated structure [8], Bragg mirrors [9, 10], buckling patterns [11], photonic crystals [12, 13], antireflection coatings [14], and monolayer of SiO₂ microparticles [15]. Those methods focused on changing the contact surface of glass substrate with organic device, which were also complicated to achieve them.

Different kinds of microlens array on the substrate surface have also been employed in some researches and showed

obvious enhancement in device efficiency. The microlens array using prepolymer NOA65 material was fabricated on the substrate which was prepatterned by microcontact printing of hydrophobic self-assembled monolayers, and the light outcoupling efficiency was improved by 24.5% without any apparent color change [16]. Spherical microlens pattern using photoresist material was designed on the backside of OLEDs substrate by conventional etching method to minimize the total internal reflection loss at substrate/air interface, and an enhancement of 1.65 could be obtained with high refractive index glass as substrate [17]. Flexible microlens arrays using a mixture of polydimethylsiloxane prepolymer by breath figure method were poured on organic substrate surface and a 34% of external quantum efficiency enhancement for OLEDs [18]. An irregular hemispherical microlens system made of flat polyethylene terephthalate film with microcavity (stacks of SiO₂ and SiNx layers) was used for organic light-emitting devices and the external out-coupling factor of the device increases by a factor of ~1.8 with wide viewing angles [19]. The numerical simulations of microlens array could also be used effectively in the infrared region with the ray tracing simulation method [20–22].

In this paper, a facile approach is proposed to enhance the light outcoupling for organic devices using traditional

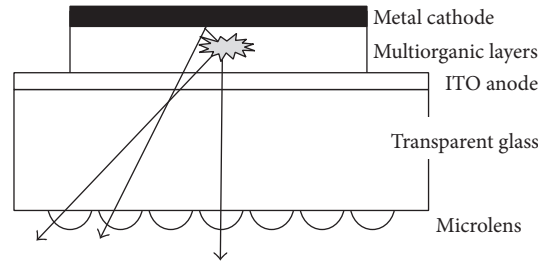


FIGURE 1: Mechanism of light outcoupling enhancement with microlens array for OLEDs.

photolithography method. Transparent substrate with microlens array is simulated with ray trace software. The photoresist is spun coating on the substrate to form microlens array and then the light outcoupling results of organic device are discussed with normal and the modified substrate. With respect to many previously reported studies on microlens fabrication method, here the easy achieved method using polymer photoresist is proposed, and by which ~85% enhancement of the light extraction for OLED is obtained.

2. Simulation

The mechanism of outcoupling enhancement with microlens array on substrate for organic device was proposed in Figure 1. Some light emitting from organic material and transmitting to glass-air interface would be reflected to glass because of the mismatch of refractive index and the incident angle higher than critical angle. With microlens array modification of the glass-air interface, the light emitting with large incident angle could be extracted out because the surface of glass was changed by the array. A portion of the light may reflect at the interface and back to the organic layer, but that portion could reflect at the metal organic interface and reach the glass-air interface again. Therefore, more light is extracted out due to morphology changing by the microlens array. The geometric structure and fill factor of the microlens array would affect the outcoupling of emission light.

In order to identify the influence of geometric structure and fill factor of the lens array to the light outcoupling efficiency, three-dimensional models of organic device with the structure shown in Figure 1 were setup and simulated with ray tracing method using TracePro software package. The structure of organic device was glass substrate ($50 \times 50 \times 1$ mm)/ITO ($30 \times 30 \times 0.0001$ mm)/multiorganic layers ($30 \times 30 \times 0.00012$ mm)/aluminum cathode ($30 \times 30 \times 0.0001$ mm). For simplicity, the metal cathode layer was regarded as ideal reflecting layer, and the absorption parameter of substrate material was set to zero. Refractive index of glass substrate was 1.5 [23, 24], which was very near to that of the AZ series photoresist used to form microlens. Five kinds of microlens with different geometrical parameters were designed and simulated, and those parameters were listed in Table 1. The design of microlens size is dependent on some reported microlens results and the dimension of the microlens we fabricated. Types 1, 2, and 3 microlens arrays were different in the contact angle with substrate; types 1, 4, and 5 microlens

array were different in the fill factor at the output plane surface of substrate.

Those organic devices with different substrate and same organic device structure were simulated with ray tracing method. Illuminance maps of the substrate output surface are shown in Figures 2(a), 2(b), and 2(c), corresponding to devices 1, 3, and 4, respectively. The maximum illuminance value is 442 lux for device 1, which is much higher than that of device 3 (321 lux). The light outcoupling efficiencies of different contact angle organic devices (types 1, 2, and 3) microlens array on substrate are 38.7%, 34.8%, and 31.4%, respectively. As the contact angle of microlens with substrate is increased, light outcoupling efficiency is improved. But the microlens array with 90° contact angle is uneasy to fabricate in the realizing process, and feasible angle should be considered combining with the manufacture method. Comparing the microlens with same contact angle and different fill factor (types 1, 4, and 5), the light outcoupling efficiencies of device are 38.7%, 38.5%, and 30.3%, respectively. The microlens fill factor on the substrate of type 1 is near to type 5, just the pattern arrangement difference, so that the outcoupling efficiencies of two devices are very comparative. For the device with lower fill factor (57.7%, device 5), the light outcoupling efficiency became obvious down to 30.3%. It's apparent that higher fill factor microlens array design would be the better choice to promote the light outcoupling. The illuminance value and uniformity of three organic devices could be obtained from Figure 2. The heterogeneity of light intensity in the substrate surface center ($30 \text{ mm} \times 30 \text{ mm}$) is caused by the quantitative limitation of light ray used in the simulation process. Comparing with the output efficiency of 21.5% for normal glass substrate, adding microlens array in the glass substrate could efficiently improve the light outcoupling and an enhancement of ~1.8 could be obtained from the simulation results with optimized microlens array structure on the substrate.

3. Microlens Fabrication and Device Performance

Before using photoresist as microlens material on the glass substrate surface, the transmittance character of the material in visible spectra area should be identified. The photoresist was spun coating on the glass substrate to form a unique thin film. Then the transmittance of photoresist film with glass substrate in visible region was tested by ultraviolet

TABLE 1: Microlens arrays with different geometrical parameters.

Device	Microlens types	Radius (μm)	Gap (μm)	Hight (μm)	Contact angle ($^\circ$)
1	Type 1	50 μm	5 μm	50 μm	90
2	Type 2	50 μm	5 μm	25 μm	60
3	Type 3	50 μm	5 μm	13.4 μm	30
4	Type 4	30 μm	5 μm	30 μm	90
5*	Type 5	50 μm	5 μm	50 μm	90

* In device 5, microlens arrangement was similar to honeycomb lattice; the other four types were orthorhombic pattern.

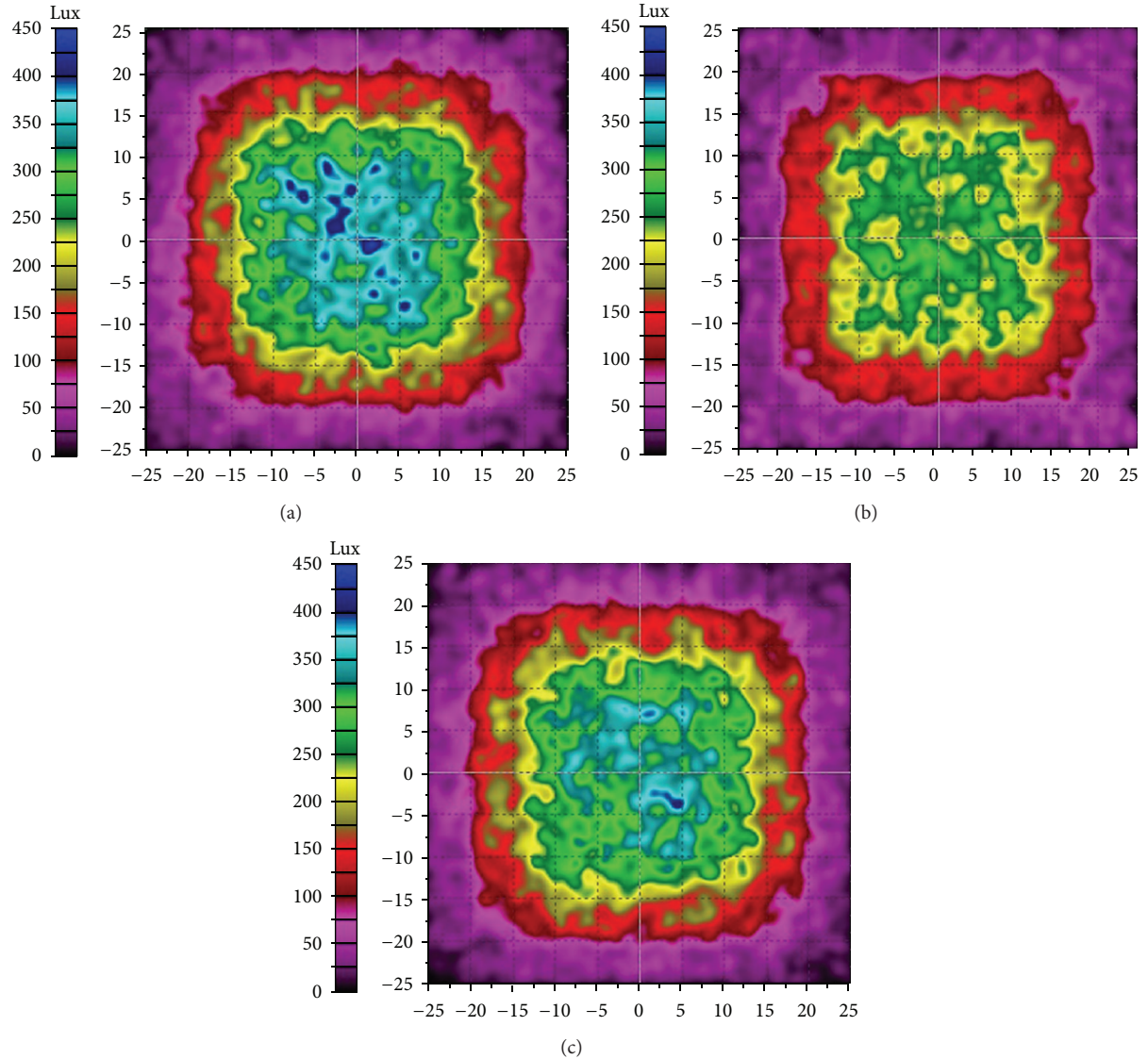


FIGURE 2: Illuminance maps of the substrate output surface, (a) for device 1, (b) for device 3, and (c) for device 4.

spectrometer UV7000 and shown in Figure 3. The average transmittance of the film (including substrate) at 400 nm ~ 700 nm region is over 95%, so that it's suitable for photoresist to act as microlens array.

The organic device with multiorganic layers structure was fabricated on the glass substrate with microlens array and the concise process was shown in Figure 4. In the figure,

the transparent substrate Figure 4(a) with ITO film was spun coating a thick layer of photoresist Figure 4(b), and then the photoresist pattern Figure 4(c) formed on the substrate using normal photolithography process and photomask. To achieve hemispherical type lens array Figure 4(d), the substrate was postbaked in oven at 140°C temperature for 30 mins. At last, multiorganic layers and metal cathode were evaporated

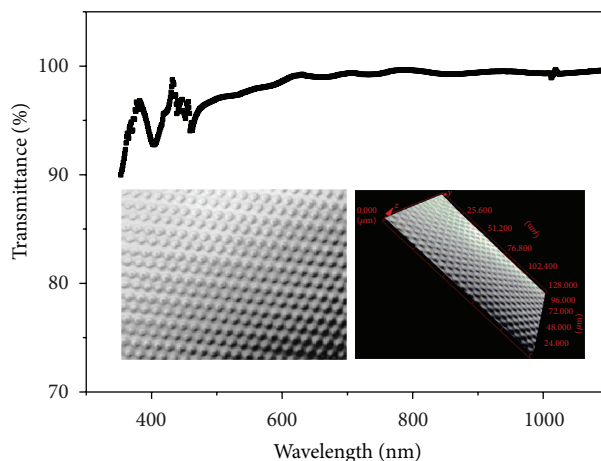


FIGURE 3: The transmittance of photoresist film (including substrate) at different wavelength; the inset is top view photo and 3-dimension image of fabricated microlens array.

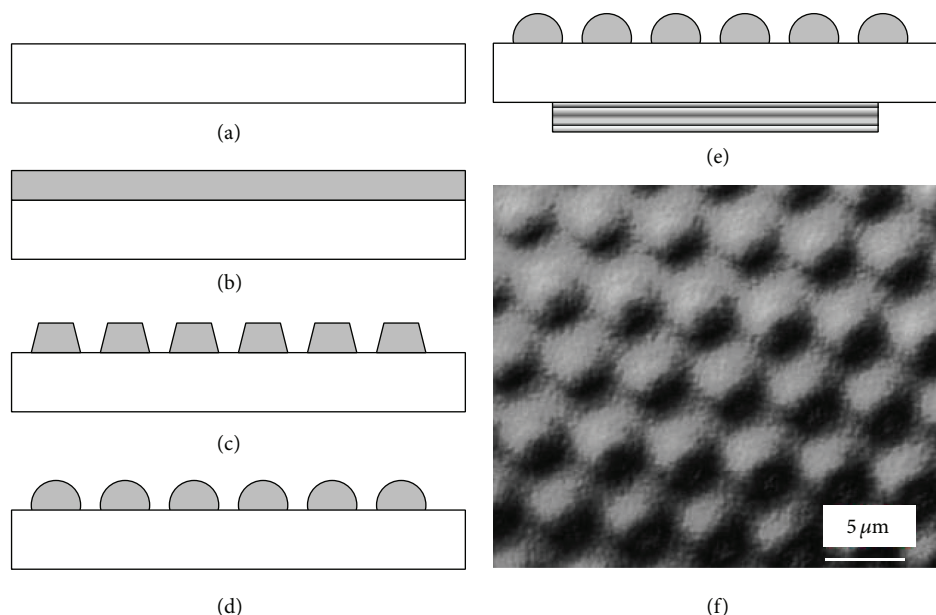


FIGURE 4: Schematic diagram of concise fabrication process for microlens array, (a) substrate, (b) coating photoresist, (c) photoresist pattern formed, (d) microlens array fabricated, (e) evaporating organic device with the microlens array substrate, (f) surface morphology of the microlens array.

on the substrate in vacuum chamber Figure 4(e). The scan electron microscope image of the microlens was described in Figure 4(f), which indicated that microlens array with semicircle shape has been formed. The top view photo and 3-dimension image of the microlens array were also shown in the inset of Figure 3. The height and diameter of microlens are $\sim 2\ \mu\text{m}$ and $5\ \mu\text{m}$, respectively, and the gap between the microlens is $\sim 0.5\ \mu\text{m}$. The size of the microlens array is decreased equal proportion with the former simulated microlens type 1, because the thick film ($50\ \mu\text{m}$) material would absorb the emission light obviously and also thick microlens with hemispherical section is uneasy to control.

In order to identify the improvement of light outcoupling performance of substrate with microlens array, organic

devices with microlens array covered substrate and normal substrate were prepared. Using same white LED diode as light source, the illumination images of the LED through normal glass substrate and the substrate with microlens array are inserted in Figure 5. It's obvious that both the luminance and the emission area of the substrate with microlens array (b) are higher than the normal substrate (a). OLEDs were also fabricated on both substrates with the device structure ITO/NPB (40 nm)/CBP: (tpbi)₂Ir(acac) (2 wt%, 30 nm)/BCP (10 nm)/Alq₃ (40 nm)/LiF (1 nm)/Al (100 nm). The luminance-voltage characteristics of two organic devices are presented in Figure 5. The luminance value of the organic device with microlens array on substrate is about 1.3 times than that with normal glass substrate at the same driving

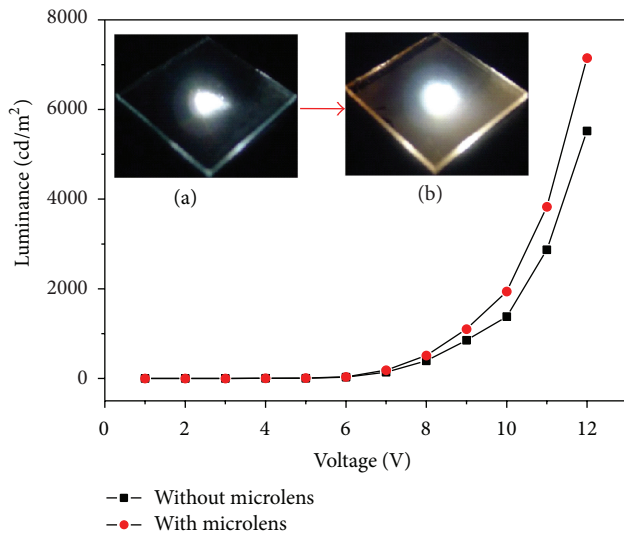


FIGURE 5: Luminance versus voltage character of two organic devices (with and without microlens array covered substrate); the inset is illumination images of the LED through normal glass substrate (a) and the substrate with microlens array (b).

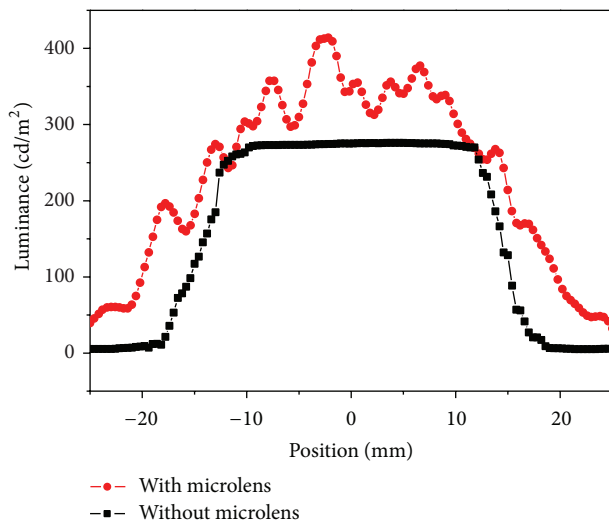


FIGURE 6: Luminance on the center line of the organic devices fabricated with and without microlens array on substrate.

voltage. A ~30% of maximum luminance enhancement for OLEDs could be obtained from the microlens array covered substrate.

Not only the luminance but also the emission area would increase from the test result shown in the inset of Figure 5. The organic devices using microlens array substrate and normal substrate (50 mm × 50 mm, the center organic emission area 30 mm × 30 mm) were fabricated with the former structure, and luminance in the center line luminance of both devices was demonstrated in Figure 6. The luminance value of device with microlens array on the substrate was obvious higher than that of device without microlens, and also the emission area extended to the margin of the glass

substrate. The luminance integral area of the device covered with microlens array is 1.28 times larger than that of normal substrate device. So the total luminance integral square area of with microlens device is ~1.64 times larger than that of without microlens. The microlens array on substrate surface could efficiently improve the light outcoupling from OLEDs.

4. Conclusion

In summary, a facile approach of fabricating microlens array on substrate is introduced to enhance the light outcoupling for organic devices using traditional photolithography method. Different kinds of microlens array are simulated with ray trace software and optimized microlens array model with an enhancement of 80% light output efficiency that is obtained from the simulation results. The microlens array with hemispherical type section and high uniform shape could be easily fabricated using photoresist material on glass substrate. Organic devices were fabricated with the microlens array covered substrate and normal glass substrate. The maximum luminance of organic device with microlens array is ~1.3 times higher than that without microlens array covered substrate and the light output intensity is about 1.64 times comparing with the device without microlens.

Conflict of Interests

The authors declare that there is no conflict of interests regarding the publication of this paper.

Acknowledgments

This work is supported by National Science Foundation of China (NSFC) via Grant no. 61006036, “the Fundamental Research Funds for the Central Universities” (ZYGX2011X012), and Program for New Century Excellent Talents in University (NCET-10-0299).

References

- [1] T. H. Han, Y. Lee, M. R. Choi et al., “Extremely efficient flexible organic light-emitting diodes with modified graphene anode,” *Nature Photonics*, vol. 6, no. 2, pp. 105–110, 2012.
- [2] W. J. Hyun, S. H. Im, O. O. Park, and B. D. Chin, “Corrugated structure through a spin-coating process for enhanced light extraction from organic light-emitting diodes,” *Organic Electronics*, vol. 13, no. 4, pp. 579–585, 2012.
- [3] Y. H. Ho, K. Y. Chen, K. Y. Peng, M. C. Tsai, W. C. Tian, and P. K. Wei, “Enhanced light out-coupling of organic light-emitting diode using metallic nanomesh electrodes and microlens array,” *Optics Express*, vol. 21, no. 7, pp. 8535–8543, 2013.
- [4] S. W. Liu, J. X. Wang, Y. Divayana et al., “An efficient non-Lambertian organic light-emitting diode using imprinted sub-micron-size zinc oxide pillar arrays,” *Applied Physics Letters*, vol. 102, Article ID 053305, 2013.
- [5] Z. B. Wang, M. G. Helander, J. Qiu et al., “Unlocking the full potential of organic light-emitting diodes on flexible plastic,” *Nature Photonics*, vol. 5, no. 12, pp. 753–757, 2011.
- [6] Y. Sun and S. R. Forrest, “Enhanced light out-coupling of organic light-emitting devices using embedded low-index grids,” *Nature Photonics*, vol. 2, no. 8, pp. 483–487, 2008.

- [7] T. W. Koh, J. M. Choi, S. Lee, and S. Yoo, "Optical outcoupling enhancement in organic light-emitting diodes: highly conductive polymer as a low-index layer on microstructured ITO electrodes," *Advanced Materials*, vol. 22, no. 16, pp. 1849–1853, 2010.
- [8] Y. G. Bi, J. Feng, Y. F. Li et al., "Enhanced efficiency of organic light-emitting devices with metallic electrodes by integrating periodically corrugated structure," *Applied Physics Letters*, vol. 100, Article ID 053304, 2012.
- [9] S.-H. Cho, Y.-W. Song, J.-G. Lee et al., "Weak-microcavity organic light-emitting diodes with improved light out-coupling," *Optics Express*, vol. 16, no. 17, pp. 12632–12639, 2008.
- [10] C.-L. Lin, T.-Y. Cho, C.-H. Chang, and C.-C. Wu, "Enhancing light outcoupling of organic light-emitting devices by locating emitters around the second antinode of the reflective metal electrode," *Applied Physics Letters*, vol. 88, Article ID 081114, 2006.
- [11] W. H. Koo, S. M. Jeong, F. Araoka et al., "Light extraction from organic light-emitting diodes enhanced by spontaneously formed buckles," *Nature Photonics*, vol. 4, no. 4, pp. 222–226, 2010.
- [12] Y. R. Do, Y. C. Kim, Y. W. Song et al., "Enhanced light extraction from organic light-emitting diodes with 2D SiO₂/SiN_x photonic crystals," *Advanced Materials*, vol. 15, no. 14, pp. 1214–1218, 2003.
- [13] W. Xu and Y. Li, "The effect of anisotropy on light extraction of organic light-emitting diodes with photonic crystal structure," *Journal of Nanomaterials*, vol. 2013, Article ID 969120, 6 pages, 2013.
- [14] K. Saxena, D. S. Mehta, V. K. Rai, R. Srivastava, G. Chauhan, and M. N. Kamalasanan, "Implementation of anti-reflection coating to enhance light out-coupling in organic light-emitting devices," *Journal of Luminescence*, vol. 128, no. 3, pp. 525–530, 2008.
- [15] T. Bocksrocker, J. Hoffmann, C. Eschenbaum et al., "Micro-spherically textured organic light emitting diodes: a simple way towards highly increased light extraction," *Organic Electronics*, vol. 14, pp. 396–401, 2013.
- [16] W. K. Huang, W. S. Wang, H. C. Kan, and F. C. Chen, "Enhanced light out-coupling efficiency of OLEDs with self-organized microlens arrays," *SID Symposium Digest of Technical Papers*, vol. 37, no. 1, pp. 961–963, 2006.
- [17] H. J. Peng, Y. L. Ho, C. F. Qiu, M. Wong, and H. S. Kwok, "Coupling efficiency enhancement of organic light emitting devices with refractive microlens array on high index glass substrate," *SID Symposium Digest of Technical Papers*, vol. 35, no. 1, pp. 158–161, 2004.
- [18] F. Galeotti, W. Mróz, G. U. Scavia, and C. Botta, "Microlens arrays for light extraction enhancement in organic light-emitting diodes: a facile approach," *Organic Electronics*, vol. 14, pp. 212–218, 2013.
- [19] J. Lim, S. S. Oh, D. Y. Kim et al., "Enhanced out-coupling factor of microcavity organic light-emitting devices with irregular microlens array," *Optics Express*, vol. 14, no. 14, pp. 6564–6571, 2006.
- [20] N. Guo, W. D. Hu, X. S. Chen et al., "Investigation of radiation collection by InSb infrared focal-plane arrays with micro-optic structures," *Journal of Electronic Materials*, vol. 42, pp. 3181–3185, 2013.
- [21] N. Guo, W. D. Hu, X. S. Chen, C. Meng, Y. Q. Lv, and W. Lu, "Optimization of microlenses for InSb infrared focal-plane arrays," *Journal of Electronic Materials*, vol. 40, no. 8, pp. 1647–1650, 2011.
- [22] N. Guo, W. D. Hu, X. S. Chen et al., "Optimization for mid-wavelength InSb infrared focal plane arrays under front-side illumination," *Optical and Quantum Electronics*, vol. 45, pp. 673–679, 2013.
- [23] H. Peng, Y. L. Ho, X.-J. Yu, M. Wong, and H.-S. Kwok, "Coupling efficiency enhancement in organic light-emitting devices using microlens array—theory and experiment," *IEEE Journal of Display Technology*, vol. 1, no. 2, pp. 278–282, 2005.
- [24] S. Mladenovski, K. Neyts, D. Pavicic, A. Werner, and C. Othe, "Exceptionally efficient organic light emitting devices using high refractive index substrates," *Optics Express*, vol. 17, no. 9, pp. 7562–7570, 2009.

Research Article

Thickness-Dependent Strain Effect on the Deformation of the Graphene-Encapsulated Au Nanoparticles

Shuangli Ye,¹ Honghua Huang,^{1,2} Cailei Yuan,² Feng Liu,¹ Min Zhai,¹ Xinzhi Shi,¹ Chang Qi,¹ and Gaofeng Wang¹

¹ Institute of Microelectronics and Information Technology, Wuhan University, Wuhan, Hubei 430072, China

² Laboratory of Nanomaterials and Sensors, School of Physics, Electronics and Communication, Jiangxi Normal University, Nanchang, Jiangxi 330022, China

Correspondence should be addressed to Shuangli Ye; slye@whu.edu.cn

Received 29 November 2013; Accepted 23 December 2013; Published 9 January 2014

Academic Editor: Wen Lei

Copyright © 2014 Shuangli Ye et al. This is an open access article distributed under the Creative Commons Attribution License, which permits unrestricted use, distribution, and reproduction in any medium, provided the original work is properly cited.

The strain effect on graphene-encapsulated Au nanoparticles is investigated. A finite-element calculation is performed to simulate the strain distribution and morphology of the monolayer and multilayer graphene-encapsulated Au nanoparticles, respectively. It can be found that the inhomogeneous strain and deformation are enhanced with the increasing shrinkage of the graphene shell. Moreover, the strain distribution and deformation are very sensitive to the layer number of the graphene shell. Especially, the inhomogeneous strain at the interface between the graphene shell and encapsulated Au nanoparticles is strongly tuned by the graphene thickness. For the mono- and bilayer graphene-encapsulated Au nanoparticles, the dramatic shape transformation can be observed. However, with increasing the graphene thickness further, there is hardly deformation for the encapsulated Au nanoparticles. These simulated results indicate that the strain and deformation can be designed by the graphene layer thickness, which provides an opportunity to engineer the structure and morphology of the graphene-encapsulated nanoparticles.

1. Introduction

Metal nanoparticles have extensive technological applications in nanosensors, catalysis, and biomedical engineering [1–3]. The high surface-to-volume ratio, however, makes the naked metal nanoparticles sensitive to the ambient atmosphere and unstable. Therefore, encapsulated metal nanoparticles have attracted increasing attention as an alternative to the naked metal nanoparticles. It has been demonstrated that it is an efficient method to prevent the oxidation of the metal nanoparticles by encapsulating them with graphene shell [4, 5]. Moreover, the properties of the encapsulated nanoparticles can be significantly modified by the graphene shell due to the unique electronic, optical, and mechanical properties of graphene [6, 7]. Recently, there is a great interest in the preparation and investigation of the graphene-encapsulated nanoparticles. The high performance of the graphene-encapsulated nanoparticles has a promising potential application [8]. On the other hand, graphene-encapsulated nanoparticles can be compared to the core/shell

nanostructures. The properties of this core/shell nanostructure strongly depend on the interplay between the core and shell layer [9, 10]. Especially, the atomic structure and morphology of the core and shell can be tailored. For example, the graphene shell has been illustrated to be used as compression cell to induce the transformation and reconstruction of the encapsulated nanoparticles by electron or ion beam irradiation, in which the compressive strain plays an important role [11, 12]. However, because the mechanical property of graphene is very sensitive to the layer number of the graphene shell, the interplay between the core and shell layer can be quite different for the graphene-encapsulated nanoparticles with various shell thickness. Until now, most reports focus on the multilayer graphitic shell with carbon onion structure, which has much weaker mechanical property than that of monolayer graphene. Therefore, information on the graphene thickness-dependent strain distribution may be crucial for designing the atomic structure and morphology of the encapsulated nanoparticles.

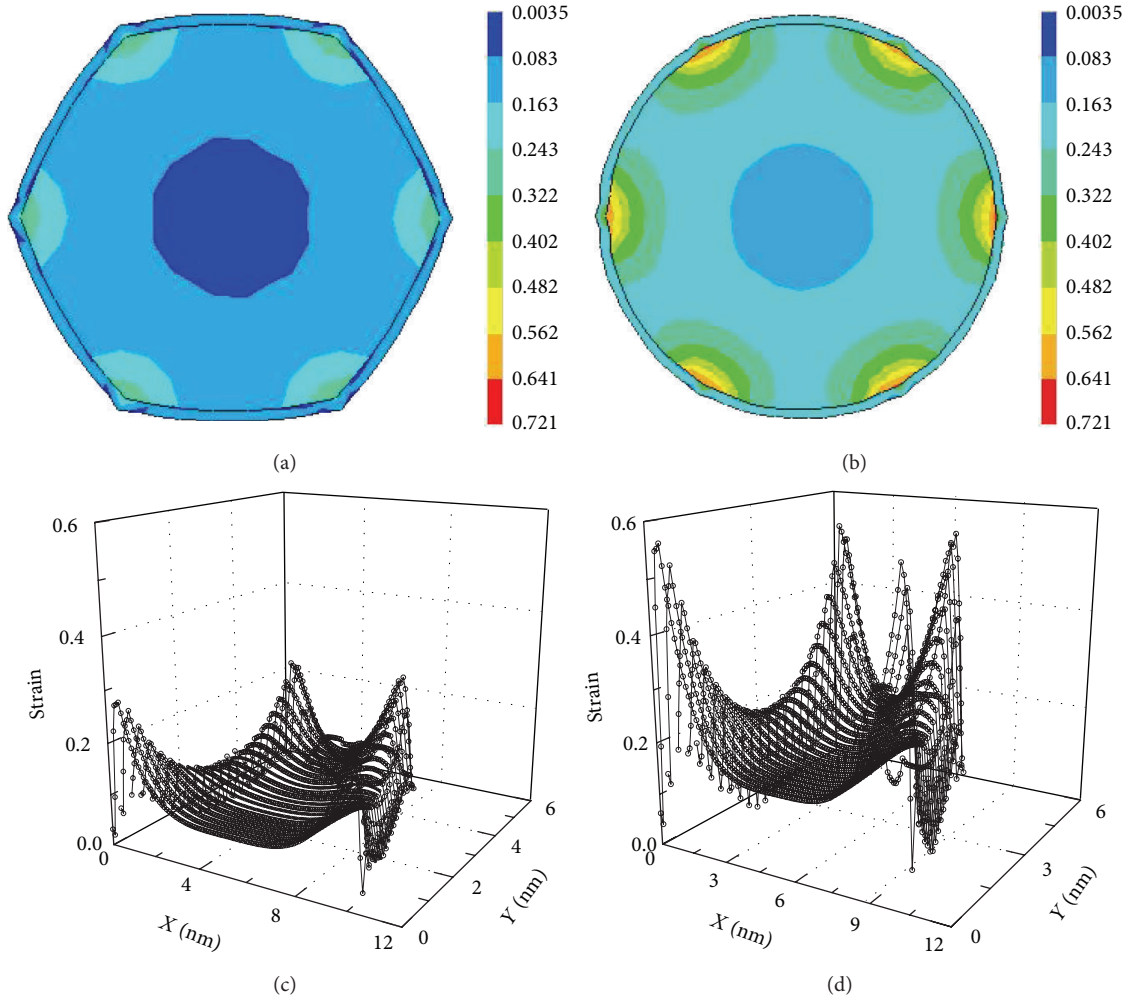


FIGURE 1: Strain distribution and morphological deformation ((a) and (b)) and X-Y plane strain profiles ((c) and (d)) for the monolayer graphene-encapsulated Au nanoparticle.

In this paper, a finite-element calculation is performed to simulate the strain distribution and deformation of the monolayer and multilayer graphene-encapsulated Au nanoparticles, respectively. The graphene thickness-dependent deformation of the encapsulated Au nanoparticles can be found. The simulated results reveal that thickness-dependent Young's modulus of the graphene shell is responsible for the tuned strain and deformation. This paper demonstrates that the thickness of the graphene shell can play an important role when the structure and morphology of the encapsulated nanoparticles are modified by the shrinkage of the graphene shell.

2. Results and Discussions

In order to investigate the strain tuning effect on the morphology evolution of the nanoparticle, a finite-element (FE) calculation is performed to simulate the dynamic strain distribution of graphene-encapsulated Au nanoparticle with different graphene thickness during the morphology evolution process. FE calculation is a versatile computer simulation

technique used for continuum modeling of deformation [13]. The simulations are taken to account for the physical properties of many materials, including elastic anisotropy, thermal expansion, and three-dimensional object shape [14–16]. Moreover, a general qualitative agreement between atomistic strain calculations and continuum elastic models has been demonstrated in nanomaterials [17, 18]. Recently, using the FE calculation to simulate the strain distribution of nanoparticles has been widely reported [19, 20]. In our FE model, the Au nanoparticle is considered as hexagonal shape with side length of 5 nm and the graphene shell encapsulates the nanoparticles without any spare space, which are the initial states. The morphology evolution and the dynamic strain distribution of the graphene-encapsulated Au nanoparticle are simulated with the continuous shrinkage of the graphene shell, which can be experimentally realized by the electron or ion beam irradiation [11, 12]. The thickness of monolayer graphene is 0.335 nm [21]; the thickness of the bilayer, triple-layer, four-layer, and seven-layer graphene is 0.81, 1.285, 1.76, and 3.185 nm with the layer distance of 0.14 nm, respectively. Young's moduli are 0.8E11, 8.91E11, 3.93E11, 0.51E11, 0.27E11,

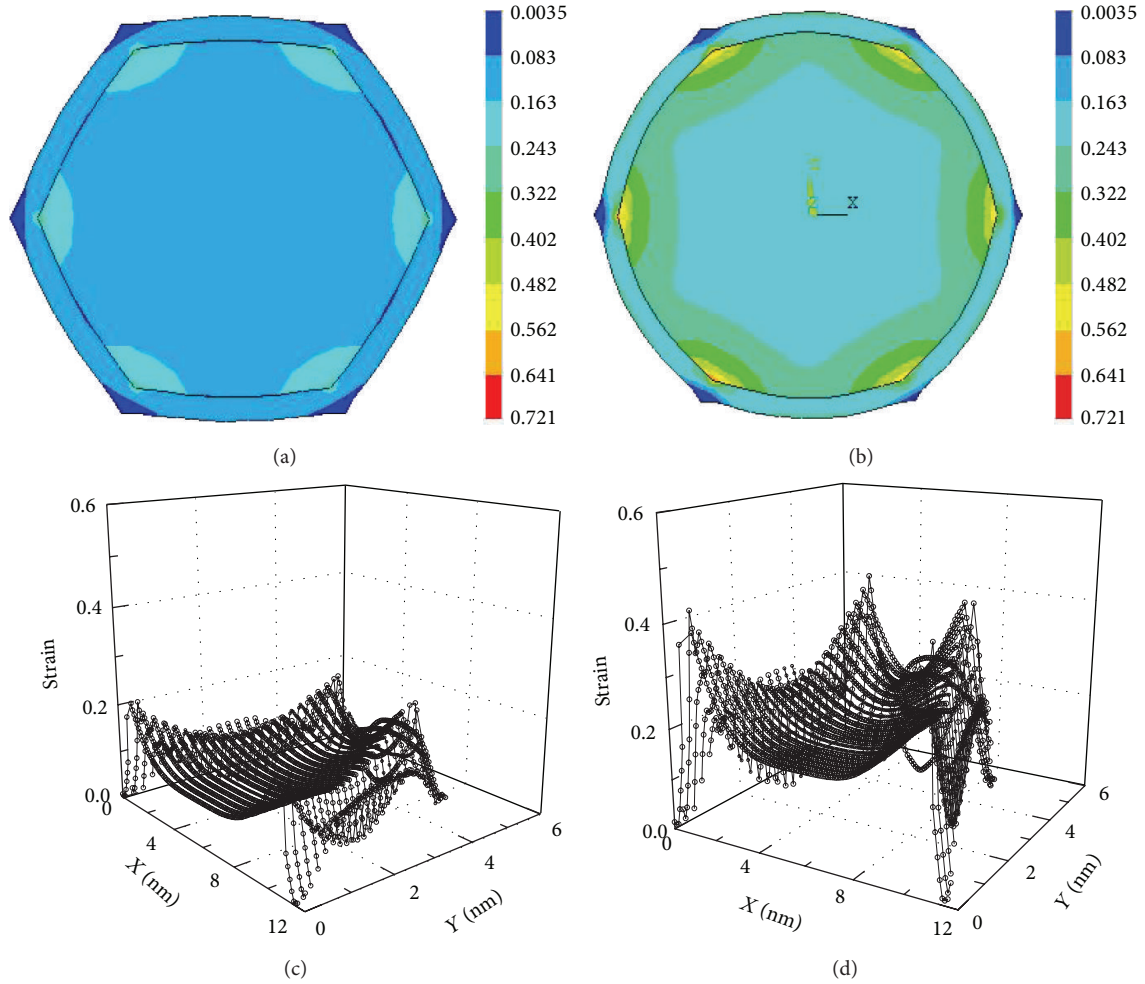


FIGURE 2: Strain distribution and morphological deformation ((a) and (b)) and X-Y plane strain profiles ((c) and (d)) for the bilayer graphene-encapsulated Au nanoparticle.

and $0.27\text{E}11\text{ Pa}$ [22, 23] for Au, monolayer, bilayer, triple-layer, four-layer, and seven-layer graphene, while Poisson's ratio is taken to be 0.42 and 0.165 for Au and graphene, respectively.

Figures 1(a), 1(b), 2(a), and 2(b) show the representative cross-sectional morphologies of the mono- and bilayer graphene-encapsulated Au nanoparticle during their morphology evolution with the increasing shrinkage of the graphene shell. Correspondingly, Figures 1(c), 1(d), 2(c), and 2(d) illustrate the X-Y plane strain profiles synchronously for these morphologies. As it can be seen in Figures 1(a) and 1(b), the encapsulated Au nanoparticle in monolayer graphene is transformed from hexagonal to spherical shape with the increasing shrinkage of graphene shell. Figures 1(c) and 1(d) indicate that the Au nanoparticle is incurred compressive strain by the monolayer graphene shell. Meanwhile, the strain distribution is very inhomogeneous, which increases with the increasing shrinkage of the graphene shell. The compressive strain reaches to the maximum at the six corners of the hexagonal Au nanoparticle close to the graphene/Au interface. However, the strain decreases very fast in Au nanoparticle as the position is away from the corners.

Figure 2 shows the morphology evolution of the bilayer graphene-encapsulated Au nanoparticle with the increasing shrinkage of the graphene shell. It can be found that the encapsulated hexagonal Au nanoparticle in bilayer graphene trends to be transformed to spherical shape with the increasing shrinkage of the graphene shell. The Au nanoparticle is incurred inhomogeneous compressive strain by the bilayer graphene shell, however, which is much smaller than that in the monolayer graphene-encapsulated Au nanoparticle, as shown in Figures 2(c) and 2(d). Moreover, compared with the strain distribution in the monolayer graphene-encapsulated Au nanoparticle, the strain distribution is less inhomogeneous and decreases much smoothly in the encapsulated Au nanoparticle with bilayer graphene as the position is away from the corners. These phenomena can be due to the fact that Young's modulus of the bilayer graphene is smaller than that of the monolayer graphene, even though both Young's moduli of the monolayer and bilayer graphene are larger than those of Au nanoparticle. Therefore, these simulated results indicate that the inhomogeneous compressive strain can be induced with the increasing shrinkage of the graphene shell when Young's modulus of the graphene shell is larger

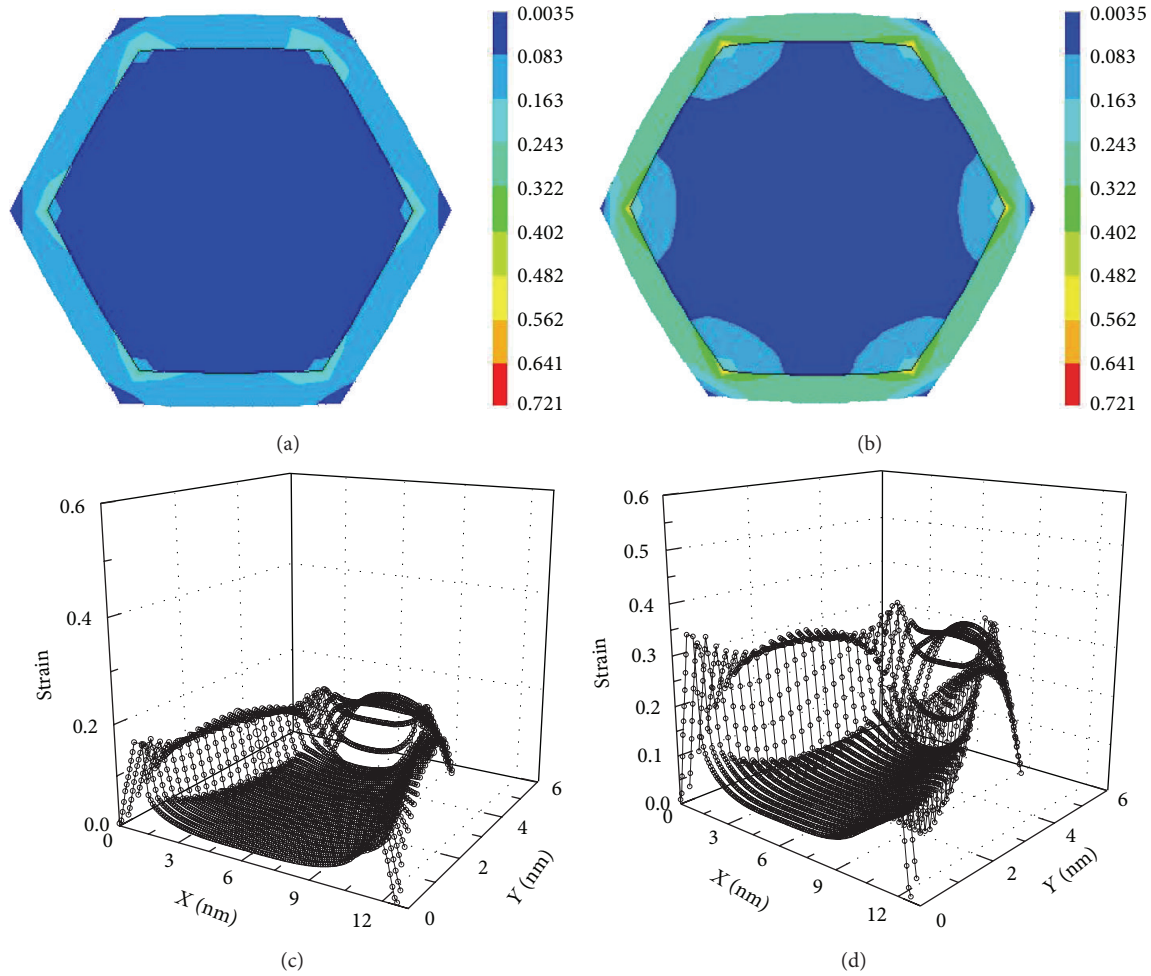


FIGURE 3: Strain distribution and morphological deformation ((a) and (b)) and X-Y plane strain profiles ((c) and (d)) for the triple-layer graphene-encapsulated Au nanoparticle.

than that of Au nanoparticle, leading to the deformation of the encapsulated Au nanoparticle. On the other hand, the strain distribution strongly depends on the graphene thickness which has different Young's modulus, especially at the graphene/Au interface. The thickness-dependent deformation and the strain distribution can be used to tune the structure and the properties of the encapsulated Au nanoparticle.

Figures 3 and 4 are the cross-sectional morphologies and strain distribution for the encapsulated Au nanoparticle with the triple-layer and seven-layer graphene shell with the increasing shrinkage of the graphene shell, respectively. Both Young's moduli of the triple-layer and seven-layer graphene are smaller than those of Au nanoparticle, because Young's modulus of the graphene decreases with the increasing of the layer number [23]. Compared with that of the monolayer and bilayer graphene-encapsulated Au nanoparticle, the simulation results demonstrate that the strongest strain happens in the graphene shell instead of in the Au nanoparticle core for triple-layer and seven-layer graphene-encapsulated Au nanoparticle, as shown in Figures 3 and 4. The strain in the shrinking graphene shell increases with the increasing of

the layer thickness. On the other hand, it can be found that decreasing Young's modulus leads to the decreasing of the inhomogeneous compressive strain on the Au nanoparticle core. Therefore, although the shrinkage of the graphene shell increases, the deformation can be hardly seen for the encapsulated Au nanoparticle with the triple-layer and seven-layer graphene shell as shown in Figures 3(a), 3(b), 4(a), and 4(b). These simulated results reveal that, with the increasing shrinkage of the graphene shell, the inhomogeneous compressive strain can be enhanced in the graphene layer close to the graphene/Au interface when Young's modulus of the graphene shell is smaller than that of Au nanoparticle. The strong local deformation of the graphene layer at the graphene/Au interface should be observed, which can be used to tune the structure and the properties of the graphene shell. However, the structure of the inner encapsulated Au nanoparticles is hardly deformed for the thicker graphene shell.

Figure 5 is the comparison of the maximum strain value with different shrinkage of the graphene shell in the graphene-encapsulated Au nanoparticle for monolayer, bilayer, triple-layer, four-layer, and seven-layer graphene

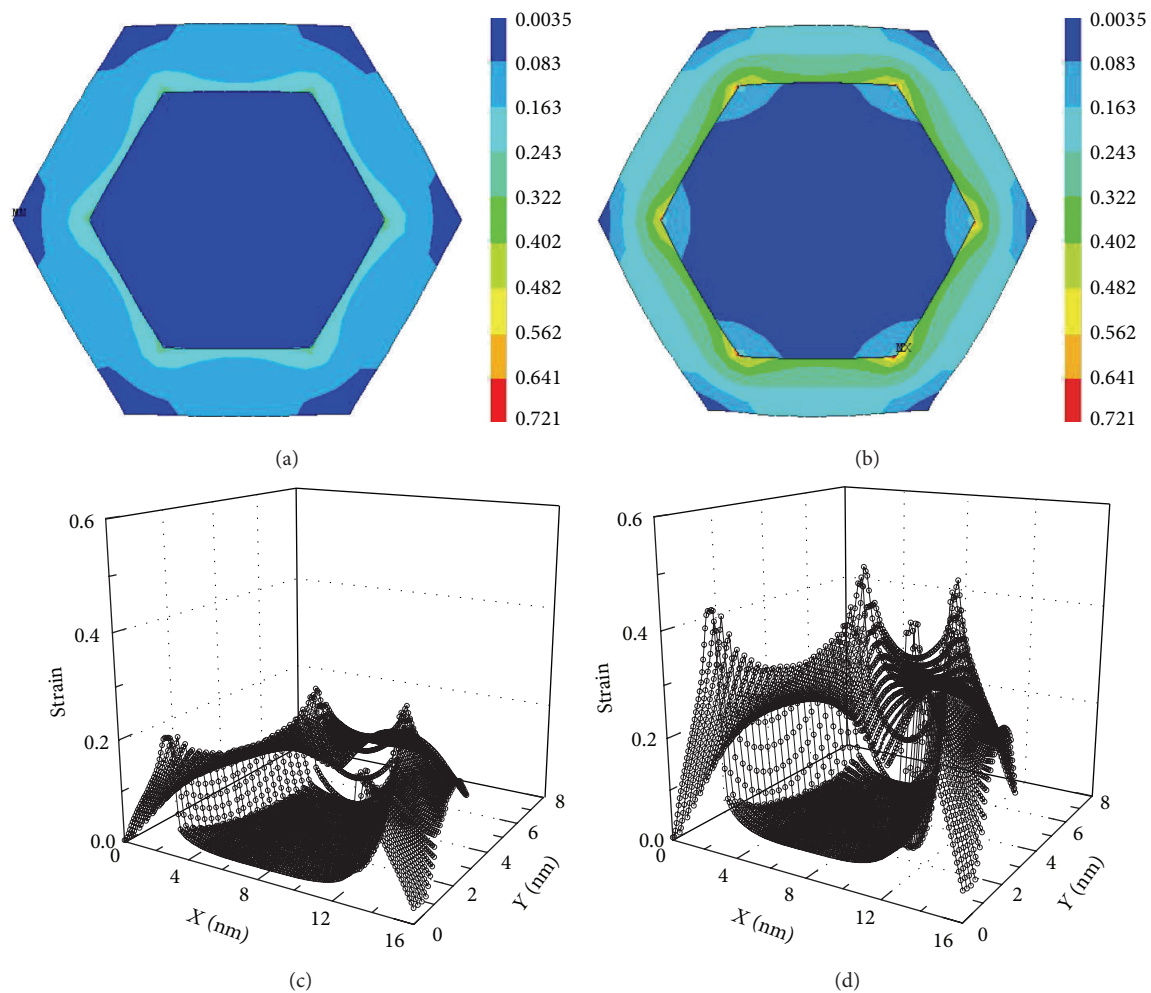


FIGURE 4: Strain distribution and morphological deformation ((a) and (b)) and X-Y plane strain profiles ((c) and (d)) for the seven-layer graphene-encapsulated Au nanoparticle.

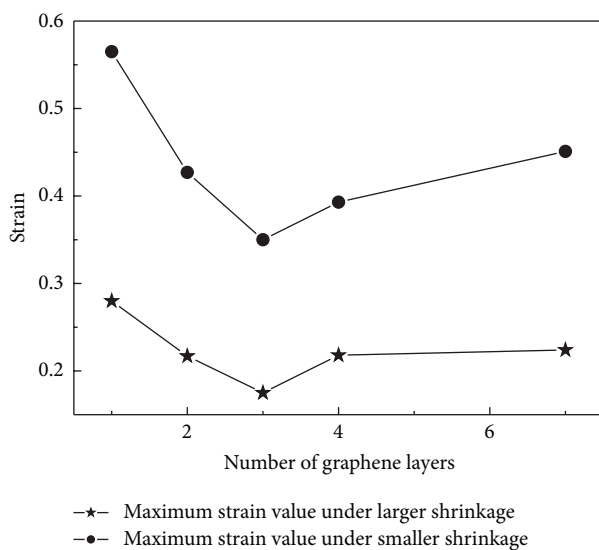


FIGURE 5: The maximum strain values in the graphene-encapsulated Au nanoparticle with different shrinkage of graphene shell.

shell, respectively. It can be found that the strongest inhomogeneous strain happens in the monolayer graphene-encapsulated Au nanoparticle, which can be attributed to highest Young's modulus of the monolayer graphene. The inhomogeneous strain decreases with the increasing graphene thickness and reaches to the smallest value in the triple-layer graphene-encapsulated Au nanoparticle. With increasing the graphene thickness further, the inhomogeneous strain is enhanced again, which can be due to the enhanced shrinkage by the thicker graphene shell. This result indicates that graphene thickness-dependent Young's modulus is responsible for the tuned strain and deformation of the graphene-encapsulated Au nanoparticle.

3. Conclusion

The influence of graphene thickness-dependent Young's modulus on the strain distribution and deformation of the graphene-encapsulated hexagonal Au nanoparticle is investigated by FE simulations. With the shrinkage of the graphene

shell, it can be found that the encapsulated Au nanoparticle can be deformed when Young's modulus of the graphene shell is larger than that of Au nanoparticle. The compressive strain distributes inhomogeneously in the graphene shell and in the Au nanoparticle core, especially at the interface. The inhomogeneous strain reaches to the maximum in the monolayer graphene-encapsulated Au nanoparticle. With increasing the number of graphene layer, the inhomogeneous strain on the encapsulated Au nanoparticles decreases. However, the local strain can be enhanced in the graphene layer close to the graphene/Au interface when Young's modulus of the graphene shell is smaller than that of Au nanoparticle. These simulated results indicate that the strain and deformation of the graphene shell and encapsulated nanoparticles can be designed separately by tuning the graphene layer thickness, which provides an opportunity to engineer the physical properties of the graphene-encapsulated nanoparticles.

Conflict of Interests

The authors declare that there is no conflict of interests regarding the publication of this paper.

Acknowledgments

This work is supported by the National Natural Science Foundation of China (Grant nos. 61006080, 11174226, 51371129, 11004087, and 11164008) and the Specialized Research Fund for the Doctor Program of Higher Education no. 20100141120080.

References

- [1] R. Narayanan and M. A. El-Sayed, "Catalysis with transition metal nanoparticles in colloidal solution: nanoparticle shape dependence and stability," *Journal of Physical Chemistry B*, vol. 109, no. 26, pp. 12663–12676, 2005.
- [2] J. Zhao, X. Zhang, C. R. Yonzon, A. J. Haes, and R. P. Van Duyne, "Localized surface plasmon resonance biosensors," *Nanomedicine*, vol. 1, no. 2, pp. 219–228, 2006.
- [3] P. K. Jain, I. H. ElSayed, and M. A. El-Sayed, "Au nanoparticles target cancer," *Nano Today*, vol. 2, no. 1, pp. 18–29, 2007.
- [4] T. Hayashi, S. Hirono, M. Tomita, and S. Umemura, "Magnetic thin films of cobalt nanocrystals encapsulated in graphite-like carbon," *Nature*, vol. 381, no. 6585, pp. 772–774, 1996.
- [5] R. Caudillo, X. Gao, R. Escudero, M. José-Yacaman, and J. B. Goodenough, "Ferromagnetic behavior of carbon nanospheres encapsulating silver nanoparticles," *Physical Review B*, vol. 74, no. 21, Article ID 214418, 2006.
- [6] K. I. Bolotin, K. J. Sikes, Z. Jiang et al., "Ultrahigh electron mobility in suspended graphene," *Solid State Communications*, vol. 146, no. 9–10, pp. 351–355, 2008.
- [7] C. Lee, X. Wei, J. W. Kysar, and J. Hone, "Measurement of the elastic properties and intrinsic strength of monolayer graphene," *Science*, vol. 321, no. 5887, pp. 385–388, 2008.
- [8] S. Yang, X. Feng, S. Ivanovici, and K. Müllen, "Fabrication of graphene-encapsulated oxide nanoparticles: towards high-performance anode materials for lithium storage," *Angewandte Chemie—International Edition*, vol. 49, no. 45, pp. 8408–8411, 2010.
- [9] H. Zeng, S. Sun, J. Li, Z. L. Wang, and J. P. Liu, "Tailoring magnetic properties of core/shell nanoparticles," *Applied Physics Letters*, vol. 85, no. 5, pp. 792–794, 2004.
- [10] A. M. Smith and S. Nie, "Semiconductor nanocrystals: structure, properties, and band gap engineering," *Accounts of Chemical Research*, vol. 43, no. 2, pp. 190–200, 2010.
- [11] A. V. Krasheninnikov and F. Banhart, "Engineering of nanostructured carbon materials with electron or ion beams," *Nature Materials*, vol. 6, no. 10, pp. 723–733, 2007.
- [12] L. Sun, A. V. Krasheninnikov, T. Ahlgren, K. Nordlund, and F. Banhart, "Plastic deformation of single nanometer-sized crystals," *Physical Review Letters*, vol. 101, no. 15, Article ID 156101, 2008.
- [13] K. H. Huebner, D. L. Dewhurst, D. E. Smith, and T. G. Byrom, *The Finite Element Method for Engineers*, John Wiley & Sons, New York, NY, USA, 2001.
- [14] J. Grönqvist, N. Søndergaard, F. Boxberg, T. Guhr, S. Åberg, and H. Q. Xu, "Strain in semiconductor core-shell nanowires," *Journal of Applied Physics*, vol. 106, Article ID 053508, 2009.
- [15] B. Liu, Y. Huang, H. Jiang, S. Qu, and K. C. Hwang, "The atomic-scale finite element method," *Computer Methods in Applied Mechanics and Engineering*, vol. 193, no. 17–20, pp. 1849–1864, 2004.
- [16] H. Hu, L. Onyebueke, and A. Abatan, "Characterizing and modeling mechanical properties of nanocomposites-review and evaluation," *Journal of Minerals & Materials Characterization & Engineering*, vol. 9, no. 4, pp. 275–319, 2010.
- [17] D. Baretin, S. Madsen, B. Lassen, and M. Willatzen, "Comparison of wurtzite atomistic and piezoelectric continuum strain models: implications for the electronic band structure," *Superlattices and Microstructures*, vol. 47, no. 1, pp. 134–138, 2010.
- [18] M. Karamehmedovic, R. Schuh, V. Schmidt et al., "Comparison of numerical methods in near-field computation for metallic nanoparticles," *Optics Express*, vol. 19, no. 9, pp. 8939–8953, 2011.
- [19] C. L. Johnson, E. Snoeck, M. Ezcurdia et al., "Effects of elastic anisotropy on strain distributions in decahedral gold nanoparticles," *Nature Materials*, vol. 7, no. 2, pp. 120–124, 2008.
- [20] Z. W. Shan, G. Adesso, A. Cabot et al., "Ultrahigh stress and strain in hierarchically structured hollow nanoparticles," *Nature Materials*, vol. 7, no. 12, pp. 947–952, 2008.
- [21] J. P. Lu, "Elastic properties of carbon nanotubes and nanoropes," *Physical Review Letters*, vol. 79, no. 7, pp. 1297–1300, 1997.
- [22] W. D. Callister Jr., *Materials Science and Engineering*, John Wiley & Sons, New York, NY, USA, 3rd edition, 1994.
- [23] Y. Zhang and C. Pan, "Measurements of mechanical properties and number of layers of graphene from nano-indentation," *Diamond and Related Materials*, vol. 24, pp. 1–5, 2012.

Research Article

Strain Distribution of Au and Ag Nanoparticles Embedded in Al_2O_3 Thin Film

Honghua Huang,^{1,2} Ying Zhang,¹ Cailei Yuan,¹ Gang Gu,¹ and Shuangli Ye²

¹ Laboratory of Nanomaterials and Sensors, School of Physics, Electronics and Communication, Jiangxi Normal University, Nanchang, Jiangxi 330022, China

² Institute of Microelectronics and Information Technology, Wuhan University, Wuhan, Hubei 430072, China

Correspondence should be addressed to Cailei Yuan; clyuan@jxnu.edu.cn

Received 24 November 2013; Accepted 3 December 2013; Published 5 January 2014

Academic Editor: Wen Lei

Copyright © 2014 Honghua Huang et al. This is an open access article distributed under the Creative Commons Attribution License, which permits unrestricted use, distribution, and reproduction in any medium, provided the original work is properly cited.

Au and Ag nanoparticles embedded in amorphous Al_2O_3 matrix are fabricated by the pulsed laser deposition (PLD) method and rapid thermal annealing (RTA) technique, which are confirmed by the experimental high-resolution transmission electron microscope (HRTEM) results, respectively. The strain distribution of Au and Ag nanoparticles embedded in the Al_2O_3 matrix is investigated by the finite-element (FE) calculations. The simulation results clearly indicate that both the Au and Ag nanoparticles incur compressive strain by the Al_2O_3 matrix. However, the compressive strain existing on the Au nanoparticle is much weaker than that on the Ag nanoparticle. This phenomenon can be attributed to the reason that Young's modulus of Au is larger than that of Ag. This different strain distribution of Au and Ag nanoparticles in the same host matrix may have a significant influence on the technological potential applications of the Au-Ag alloy nanoparticles.

1. Introduction

The incorporation of multiple metals into a single system has induced intensive interest due to its promising applications. Therefore, the fabrication of alloy nanoparticles has become a major challenge. Particularly, Au-Ag alloy has been confirmed to be suitable for the application in surface plasmon absorption. These two noble metals have practically the same lattice constant and are chemically similar. Moreover, in the bulk phase they are miscible at all compositions. These properties provide the possibility to study the equal structures of different compositions without having to consider the influence of strong structural changes. By combining these two metals into a single entity, the catalytic performance of the material can be enhanced [1] and the surface plasmon absorption of Au-Ag alloy nanoparticles can be varied continuously between the absorptions of monometallic Au and Ag nanoparticles by changing the ratios of the precursors of Au and Ag [2].

On the other hand, nanocomposite films that consist of small metal nanoparticles embedded in metal oxides have

attracted attention because they are expected to have many useful electronic and optical properties as a result of quantum size effects [3, 4]. These systems have useful applications in catalysis, photocatalysis, sensors, and novel optoelectronic devices. However, substantial compressive strain can be induced during the growth process of nanoparticles embedded in a host matrix. The strain may also have much influence on the microstructure and physical properties of nanoparticles [5, 6]. Therefore, in order to understand and control the properties of Au-Ag alloy nanoparticles, the investigation on the interplay between the strain distribution of the alloy nanoparticles in a matrix and the state of individual Au and Ag nanoparticles is crucial for the technological potential applications of the Au-Ag alloy nanoparticles.

2. Materials and Methods

Au and Ag nanoparticles embedded in an amorphous Al_2O_3 matrix are fabricated by the pulsed laser deposition (PLD) method and rapid thermal annealing (RTA) technique,

respectively. Briefly, a KrF pulsed laser is used to ablate the target in a high-vacuum chamber. The wavelength of the excimer laser is 248 nm. The target to be laser ablated is prepared from a high-purity (99.99%) round Al_2O_3 target with diameter of 25 mm and one small high-purity (99.99%) Au/Ag square plate with length of 2 mm, respectively. During the PLD process, the center of the assembled Al_2O_3 -Au/ Al_2O_3 -Ag target is set to spin slowly around its central axis and the laser beam vaporizes the two-component materials alternately. The laser deposition is carried out in a high-vacuum system with a background pressure of about 8×10^{-7} torr. After the deposition, the samples are subjected to rapid thermal annealing at 400°C for 60 s in air ambient. The structure of the samples is examined by using high-resolution transmission electron microscope (HRTEM) with JEOL2010 microscope. The TEM electron diffraction pattern is matched against a simulated diffraction pattern generated by Java Electron Microscopy Simulation (JEMS) TEM simulating software [6].

3. Results and Discussion

Figure 1(a) shows the HRTEM image of Au nanoparticle annealed at 400°C , with its corresponding electron diffraction pattern on the top right corner. The diffraction pattern is matched against a simulated diffraction pattern generated by JEMS software for the Au nanoparticle embedded in Al_2O_3 thin film. It can be confirmed that the Al_2O_3 thin films still remain amorphous after annealing. It can also be seen that there is a single crystal Au nanoparticle with spherical shape embedded in Al_2O_3 matrix. The average size of the Au nanoparticles is approximately 5 nm. With the experimental and the simulated diffraction patterns, it can be deduced that the structure of the Au nanoparticle is cubic structure (space group Fm-3 m). Figure 1(b) shows the HRTEM image of Ag nanoparticle annealed at 400°C , with its corresponding electron diffraction pattern on the top right corner. It can be seen that there is a single crystal Ag nanoparticle with spherical shape embedded in amorphous Al_2O_3 matrix. The average size of the Ag nanoparticles is also approximately 5 nm. With the experimental and the simulated diffraction patterns, it can be deduced that the nanoparticle structure of Ag nanoparticle is face-centered cubic structure (space group Fm-3 m).

Usually, the two basic approaches to calculate the strain distribution in materials are continuum elasticity and atomistic elasticity. Although atomistic elasticity is expected to give more reliable results, its application is limited by the number of atoms which can be taken into account. Finite-element calculation is a versatile computer simulation technique used for continuum modeling of deformation in materials [7]. The simulations are taken into account for the physical properties of many materials, including elastic anisotropy, thermal expansion, and three-dimensional object shape. Moreover, a general qualitative agreement between atomistic strain calculations and continuum elastic models has been demonstrated in nanomaterials [8, 9]. Recently, using the finite-element calculation to simulate the strain distribution

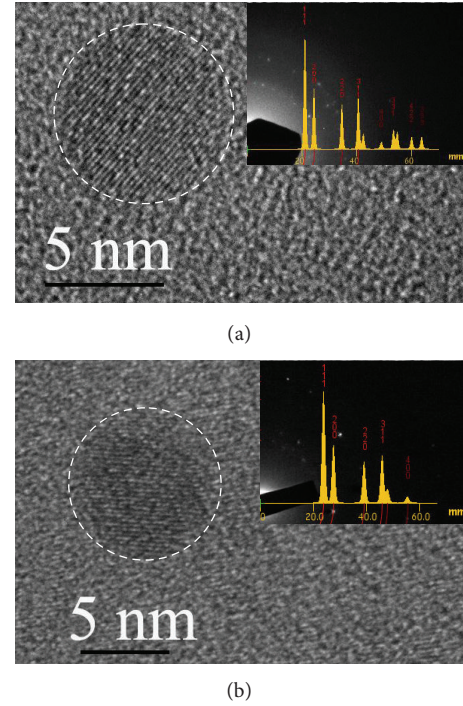


FIGURE 1: (a) HRTEM image of a single crystal Au nanoparticle embedded in amorphous Al_2O_3 matrix, with its corresponding electron diffraction pattern on the top right corner. (b) HRTEM image of a single crystal Ag nanoparticle embedded in amorphous Al_2O_3 matrix, with its corresponding electron diffraction pattern on the top right corner.

of nanoparticles has been widely reported [10, 11]. In this paper, the strain generated by the growth of Au and Ag nanoparticle embedded in an Al_2O_3 thin film is qualitatively simulated by finite-element (FE) calculations [5, 6]. Young's modulus is taken to be 170 [12], 76 [13], and 360 GPa [6] for Au, Ag, and Al_2O_3 , respectively. Poisson's ratio is taken to be 0.42, 0.38, and 0.24 for Au, Ag, and Al_2O_3 , respectively. In our simulation, the FE model for the strain calculations is based upon the following assumptions: a spherical, isotropic, linear-elastic nanoparticle is embedded in isotropic and linear-elastic matrix; the nanoparticle surface is welded to the matrix; the volumes change of the Au and Ag nanoparticles corresponds to a change in annealing temperature with taking the same temperature dependence of thermal expansion coefficient into account for the Au and Ag nanoparticles. Due to the nanoparticle residing in the matrix cavity which is too small, the matrix atoms are not being able to move rapidly enough to accommodate the growing nanoparticle, which results in the compressive strain on the nanoparticle. The strain distribution can be generated by the thermal expansion mismatch because of the growth of Au and Ag nanoparticles.

Figures 2(a) and 2(b) show the cross-sectional strain distributions for Au and Ag nanoparticles grown in Al_2O_3 thin films under the same condition, respectively. The inhomogeneous strain distribution can be found, which is distinguished by the different color as signed by the marks

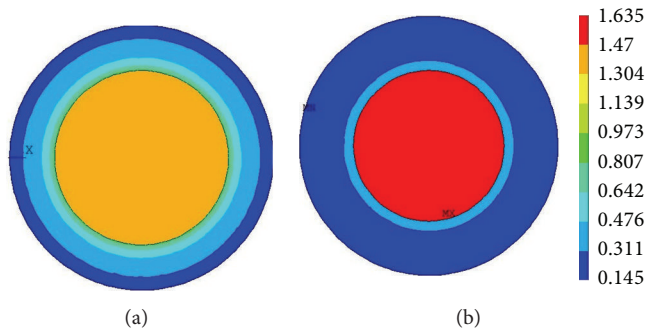


FIGURE 2: (a) Cross-sectional strain distribution of Au nanoparticle. (b) Cross-sectional strain distribution of Ag nanoparticle.

in Figure 2. Correspondingly, Figures 3(a) and 3(b) show the X-Y plane strain profiles of Au and Ag nanoparticles embedded in Al_2O_3 matrix, respectively. Obviously, it can be seen that both the Au and Ag nanoparticles incur compressive strain from the Al_2O_3 matrix. Usually, the nanoparticles formation mechanism can be explained as follows. Firstly, the probability for nucleation increases at higher temperature, and the nuclei density is thus higher. Once sufficient surface energy is available, the number of nanoparticles increases rapidly as fresh nuclei are formed. On the other hand, the nanoparticles already formed by nucleation continue to grow by adatom attachment via surface diffusion, leading to agglomeration of bigger nanoparticles with increasing temperature [3]. Because of thermal expansion mismatch, the formation of nanoparticles in a matrix can be accompanied by the generation of compressive strain [14, 15]; that is, the Al_2O_3 matrix exerts a compressive strain on the Au and Ag nanoparticles due to the volume expansion of Au and Ag nanoparticles. Moreover, it should be noted that the compressive strain existing on Au nanoparticle is much weaker than that on Ag nanoparticle. This phenomenon can be attributed to the reason that Young's modulus of Au is larger than that of Ag. Thus, this different strain distribution of Au and Ag nanoparticles in the same host matrix may have a significant influence on thermal dynamical properties of Au-Ag alloy nanoparticles.

4. Conclusions

In summary, Au and Ag nanoparticles embedded in amorphous Al_2O_3 matrix are fabricated using PLD method and RTA technique, respectively. The HRTEM results reveal that the spherical Au nanoparticle with cubic structure and Ag nanoparticle with Face-centered cubic structure are formed in amorphous Al_2O_3 matrix, respectively. The strain distribution of Au and Ag nanoparticles embedded in the Al_2O_3 matrix is investigated. FE calculations clearly indicate that both the Au and Ag nanoparticles incur compressive strain from Al_2O_3 matrix. The compressive strain existing on Ag nanoparticle is much weaker than that in Au nanoparticle. This phenomenon can be attributed to the reason that Young's modulus of Au is larger than that of Ag. This different strain distribution of Au and Ag nanoparticles in the same host

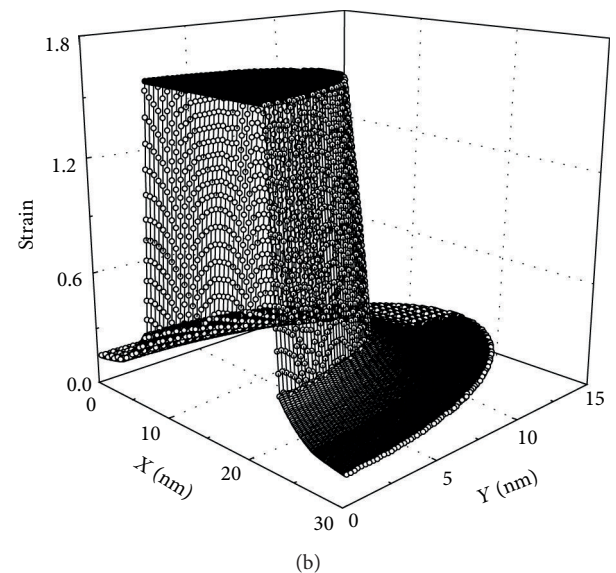
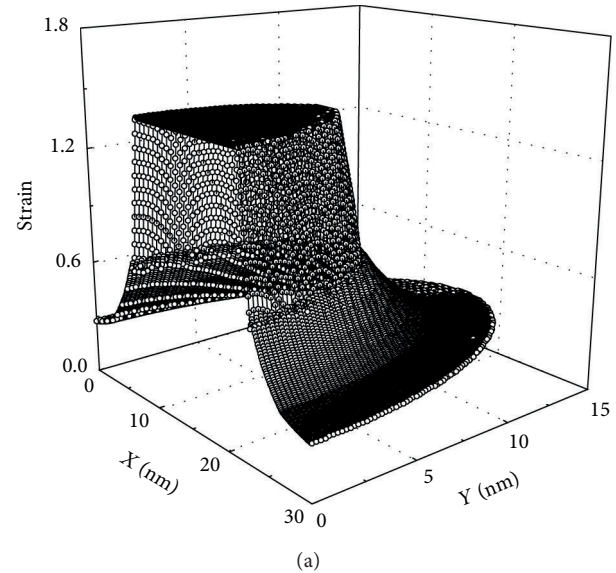


FIGURE 3: (a) X-Y plane strain profile of Au nanoparticle. (b) X-Y plane strain profile of Ag nanoparticle.

matrix may have a significant influence on thermal dynamical properties of Au-Ag alloy nanoparticles.

Conflict of Interests

The authors declare that there is no conflict of interests regarding the publication of this paper.

Acknowledgments

This work is supported by the National Natural Science Foundation of China (Grant nos. 11004087, 11164008, 61006080, and 11174226) and Ph.D. Programs Foundation of Ministry of Education of China.

References

- [1] J.-H. Liu, A.-Q. Wang, Y.-S. Chi, H.-P. Lin, and C.-Y. Mou, "Synergistic effect in an Au-Ag alloy nanocatalyst: CO oxidation," *Journal of Physical Chemistry B*, vol. 109, no. 1, pp. 40–43, 2005.
- [2] P. Mulvaney, "Surface plasmon spectroscopy of nanosized metal particles," *Langmuir*, vol. 12, no. 3, pp. 788–800, 1996.
- [3] C. L. Yuan, P. S. Lee, and S. L. Ye, "Formation, photoluminescence and charge storage characteristics of Au nanocrystals embedded in amorphous Al_2O_3 matrix," *Europhysics Letters*, vol. 80, no. 6, Article ID 67003, 2007.
- [4] X. F. Luo, C. L. Yuan, and Z. R. Zhang, "Synthesis, photoluminescence and charge storage characteristics of isolated silver nanocrystals embedded in Al_2O_3 gate dielectric," *Thin Solid Films*, vol. 516, no. 21, pp. 7675–7679, 2008.
- [5] C. L. Yuan, S. L. Ye, B. Xu, and W. Lei, "Strain induced tetragonal SrTiO_3 nanoparticles at room temperature," *Applied Physics Letters*, vol. 101, no. 7, Article ID 071909, 2012.
- [6] C. L. Yuan, Q. Liu, and B. Xu, "Strain-induced structural phase transition of Si nanoparticles," *Journal of Physical Chemistry C*, vol. 115, no. 33, pp. 16374–16377, 2011.
- [7] K. H. Huebner, D. L. Dewhurst, D. E. Smith, and T. G. Byrom, *The Finite Element Method for Engineers*, John Wiley & Sons, New York, NY, USA, 2001.
- [8] J. Grönqvist, N. Søndergaard, F. Boxberg, T. Guhr, S. Åberg, and H. Q. Xu, "Strain in semiconductor core-shell nanowires," *Journal of Applied Physics*, vol. 106, no. 5, Article ID 053508, 2009.
- [9] D. Baretin, S. Madsen, B. Lassen, and M. Willatzen, "Comparison of wurtzite atomistic and piezoelectric continuum strain models: implications for the electronic band structure," *Superlattices and Microstructures*, vol. 47, no. 1, pp. 134–138, 2010.
- [10] C. L. Johnson, E. Snoeck, M. Ezcurdia et al., "Effects of elastic anisotropy on strain distributions in decahedral gold nanoparticles," *Nature Materials*, vol. 7, no. 2, pp. 120–124, 2008.
- [11] Z. W. Shan, G. Adesso, A. Cabot et al., "Ultrahigh stress and strain in hierarchically structured hollow nanoparticles," *Nature Materials*, vol. 7, no. 12, pp. 947–952, 2008.
- [12] L. T. Sun, A. V. Krashennnikov, T. Ahlgren, K. Nordlund, and F. Banhart, "Plastic deformation of single nanometer-sized crystals," *Physical Review Letters*, vol. 101, no. 15, Article ID 156101, 2008.
- [13] M. F. Ashby and D. R. H. Jones, *Engineering Materials*, vol. 1, Pergamon, Oxford, UK, 1980.
- [14] H. Hofmeister, M. Dubiel, H. Goj, and S. Thiel, "Microstructural investigation of colloidal silver embedded in glass," *Journal of Microscopy*, vol. 177, no. 3, pp. 331–336, 1995.
- [15] V. V. Voronkov and R. Falster, "Strain-induced transformation of amorphous spherical precipitates into platelets: application to oxide particles in silicon," *Journal of Applied Physics*, vol. 89, no. 11, pp. 5965–5971, 2001.

Research Article

A Flexible Blue Light-Emitting Diode Based on ZnO Nanowire/Polyaniline Heterojunctions

Y. Y. Liu,¹ X. Y. Wang,¹ Y. Cao,² X. D. Chen,¹ S. F. Xie,¹ X. J. Zheng,¹ and H. D. Zeng²

¹ School of Materials Science and Engineering, University of Shanghai for Science and Technology, Shanghai 20093, China

² School of Materials Science and Engineering, East China University of Science and Technology, Shanghai 200235, China

Correspondence should be addressed to X. Y. Wang; xianyingwang@usst.edu.cn and H. D. Zeng; huidanzeng@ecust.edu.cn

Received 14 June 2013; Accepted 5 September 2013

Academic Editor: Wen Lei

Copyright © 2013 Y. Y. Liu et al. This is an open access article distributed under the Creative Commons Attribution License, which permits unrestricted use, distribution, and reproduction in any medium, provided the original work is properly cited.

An organic/inorganic light-emitting diode (LED) consisting of n-type vertically aligned ZnO nanowires (NWs) and p-type proton acid doped polyaniline (PANi) is reported. The device was fabricated on flexible indium-tin-oxide (ITO) coated polyethylene terephthalate (PET) substrate. A broad blue light emission band ranging from 390 nm to 450 nm was observed in the electroluminescence (EL) spectra of the device, which was related to the interface recombination of electrons in the conduction band of ZnO NWs and holes in the polaron level of PANi. The turn-on voltage of the device is ~3.5 V, lower than most of ZnO NWs based LED devices. In combination with the easy fabrication, flexibility, low power consumption, and mechanical robustness, this novel device is very promising in the application of blue LEDs.

1. Introduction

ZnO, especially in its nanostructured form, has been considered to be attractive for applications in ultraviolet (UV) lasers [1], LEDs [2–4], and solar cells [5] because of the wide band gap and high exciton binding energy. However, it remains critical and challenging to fabricate high quality ZnO with stable p-type conductivity because of the intrinsically n-type nature. The difficulty in doping ZnO to p-type polarity has led the researchers to seek to create heterojunctions with other p-type semiconductors to enable the use of ZnO in all kinds of electronic devices. Many efforts have been made to grow n-type ZnO on p-type substrates, but usually the quality of such heterojunctions is limited by the lattice mismatch. P-type conducting polymer has many advantages including easy fabrication, flexibility, and tunable carrier densities. Various LEDs based on ZnO NWs/p-type polymer heterostructures have been reported in the literature [3, 4]; however, blue LED is still quite limited [6].

In this work, a blue LED device consisting of vertically aligned ZnO NWs and p-type conducting PANi heterojunction was fabricated. PANi was selected as the hole conducting layer because of its facile synthetic process, good environmental stability, easy conductivity control, and cheap production in large quantities. The structure of the LED device was

schematically illustrated in Figure 1. Vertically aligned ZnO NWs are used as the light emission units, and proton doped PANi is used as the hole-transporting layer. Au film serves as the top electrode, and ITO is the bottom electrode. The function of polymethyl methacrylate (PMMA) is to form a smooth surface for PANi coating. A broad blue light emission band ranging from 390 nm to 450 nm was observed from the EL spectra of the ZnO NWs/PANi heterojunction LED. The origins of the blue emission were also discussed in this paper.

2. Experimental

For the LED device fabrication, ZnO NW arrays were grown on ITO coated PET substrate using a low temperature hydrothermal method. Equimolar (0.05 M) of hydrated zinc nitrate ($\text{Zn}(\text{NO}_3)_2 \cdot 6\text{H}_2\text{O}$) and hexamethylenetetramine (HMT) was used as the precursor. The reaction was carried out at 90°C for 6 hours. After growth the as-grown NW forest was infiltrated with 5% (weight percent) PMMA solution (in toluene) to provide a smooth film for subsequent PANi coating. Then oxygen plasma etching was applied to remove excessive PMMA and expose the NW tips for junction formation with PANi. HCl doped PANi dissolved in dimethylformamide (DMF) was spin coated on top of ZnO NW tips. The device was then baked at 60°C for 10 hours to completely remove

the organic solvents. Finally Au top electrode with the thickness of 150 nm was deposited using e-beam evaporation with the deposition rate of 0.1 nm/s.

The morphologies and microstructures of the as-synthesized ZnO NW arrays were examined using scanning electron microscope (SEM, FEI Quanta FEG), transmission electron microscope (TEM, FEI G30), and X-ray diffraction pattern (XRD, Bruker D8 Advance). Electrical properties of the devices were examined using semiconducting characterization system (SCS, Keithley 4200) equipped with a probe station (Cascade M 150). The photoluminescence (PL) and EL spectra were detected using a FS 920 type spectrometer (Edinburgh).

3. Results and Discussions

From the SEM image of the as-grown ZnO NW arrays (Figure 2(a)), it can be seen that ZnO NWs are uniformly distributed on the PET substrate and primarily vertically aligned. The diameter of ZnO NWs ranges from 80 nm to 130 nm, and the average height is around $3\ \mu\text{m}$. The TEM image of a randomly picked individual NW is shown in Figure 2(b). Clearly, the NW has uniform diameter of 110 nm throughout the entire length. The selected area diffraction pattern shown in the inset of Figure 2(b) demonstrates that the NWs are single crystalline with preferred $\langle 0001 \rangle$ growth direction. Strong (0002) diffraction peak centered at 34.4° can be observed from XRD pattern of the NW arrays (Figure 2(c)), suggesting that the NWs are highly ordered along c -axis with the lattice spacing of 0.52 nm. No other impurity peaks or ITO related peaks are observed. The PL spectra of the as-grown ZnO NW arrays are presented in Figure 2(d). The strong ultraviolet emission peak centered at 383 nm is the intrinsic luminescence of ZnO NWs. The defect related visible emission at around 500 nm is much weaker than the UV peak, indicating that ZnO NWs are of high degree of crystalline quality with few defects.

Figure 3(a) shows the top-view SEM image of the surface of the device after PANi deposition. The bright spots represent the tips of ZnO NWs, and the dark area is the space between NWs solidly filled with PMMA. Obviously the NWs are well separated, demonstrating that no agglomerations occurred during the polymer infiltration process. The density of the NW tips can be estimated to be $14\ \text{NW}/\mu\text{m}^2$. Figure 3(b) shows the current-voltage (IV) characteristics of the ZnO NWs/PANi heterostructure LED device. The IV curve clearly shows nonlinear increase of the current under the forward bias, which indicates the formation of p-n junction between ZnO NWs and PANi. The turn-on voltage of the device is around 1.3 V, as shown in Figure 3(b).

The EL spectra of the ZnO NWs/PANi heterojunction LED device were measured under different forward biasing voltages (2 V, 3.5 V, 5 V, and 6.5 V). As is shown in Figure 4(a), the light emission is too low to be detected when the forward bias is below 2 V. However when the bias voltage is larger than 3.5 V, a broad blue light emission band spreading through 390 nm to 450 nm can be observed. Obviously, this band is neither related with the near band edge nor to the deep level

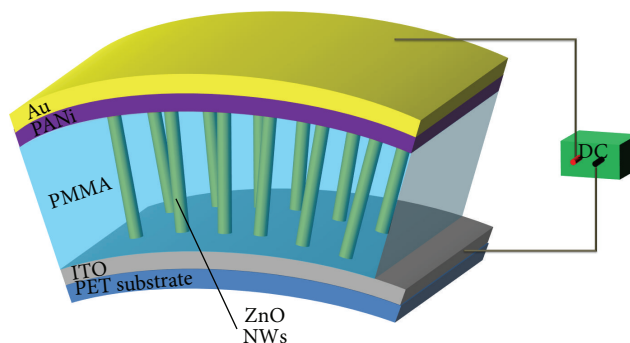


FIGURE 1: Schematic diagram of the flexible LED device. The basic structure of the device is Au/PANi/ZnO NWs in PMMA matrix/ITO/PET substrate.

emission of ZnO NWs. Blue LEDs based on ZnO NWs/p-GaN [2] and ZnO NWs/PFO [7] heterojunctions have been reported before; however, the emission is often dominated by the p-type conducting layer instead of ZnO NWs. To understand the origins of the blue light emission of ZnO NWs/PANi device, the energy band diagrams of all the layers were schematically illustrated in Figure 4(b). Doping caused a self-localized polaron band in PANi, existing as a defect band in the bandgap (3.4 eV) between the valence band and the conduction band. It is half-filled and has a significant band width ($\sim 1.1\ \text{eV}$) [8–10]. When a forward bias is applied, electrons in the conduction band of the ZnO NWs will be driven to move towards the PANi. Also the holes in the polaron band of PANi will move towards ZnO because of the relatively low energy barrier. The electrons and holes recombine at the interface of the p-n junction and produce a photon. The emission wavelength in the EL spectra must be corresponding with the bandgap between the conduction band of ZnO and the polaron band of PANi, although the exact position of the polaron band was not found in the literatures.

Several other features can also be found from the EL spectra. First, the turn-on voltage of ZnO NWs/PANi heterostructure is substantially lower compared with other ZnO NWs based LED devices. For example, the turn-on voltage is 10 V for ZnO NWs/p-type GaN film hybrid junction [2] and 6 V for ZnO NWs/p-Si junction [11]. The small turn-on voltage can be attributed to the low carrier injection barriers (Figure 4(b)). Second, the blue emission peak is increasingly broadened, and the intensity is enhanced with the increase of the bias voltage. The broad blue light-emitting range suggests that the emission behavior is complicated and must be related to the polaron energy band of PANi. With the increase of the forward biasing voltage, more electrons in the conduction band of ZnO are driven to move towards the PANi, and more holes in the valence band of PANi will move towards ZnO. Thus, a larger number of protons can be produced by the recombination of the carriers. Also, peak splitting in the blue region can be observed, which is not well understood. However, it is possible to be caused by the diffraction when the light transmits through hexagonal ZnO NWs. Third, the defect related visible light emission band is broadened, and the peak center is red shifted compared with that in the PL

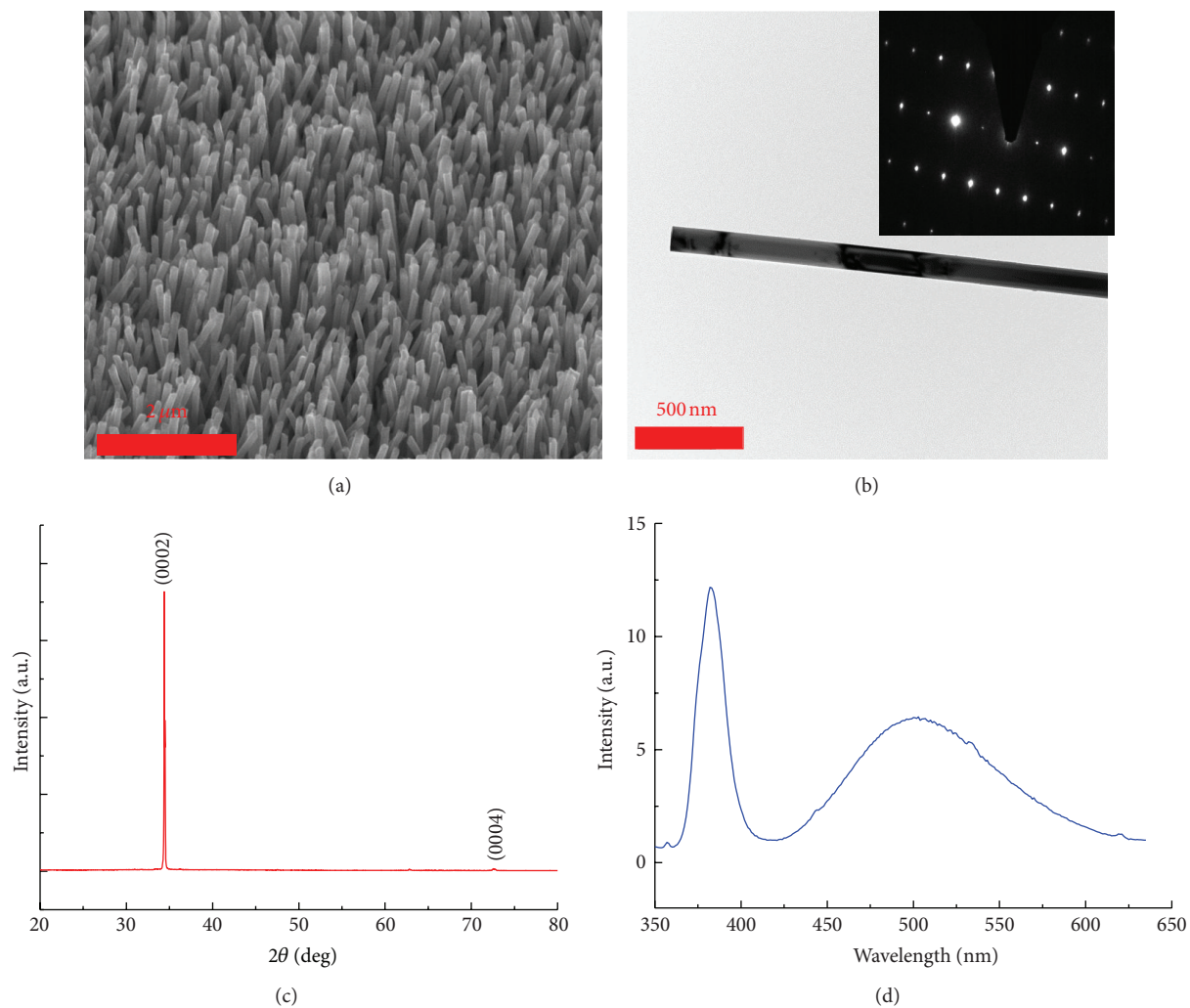


FIGURE 2: Morphology and structural characterizations of ZnO NWs. (a) SEM image. (b) TEM image. Inset: SAED pattern. (c) XRD curve. (d) PL spectra.

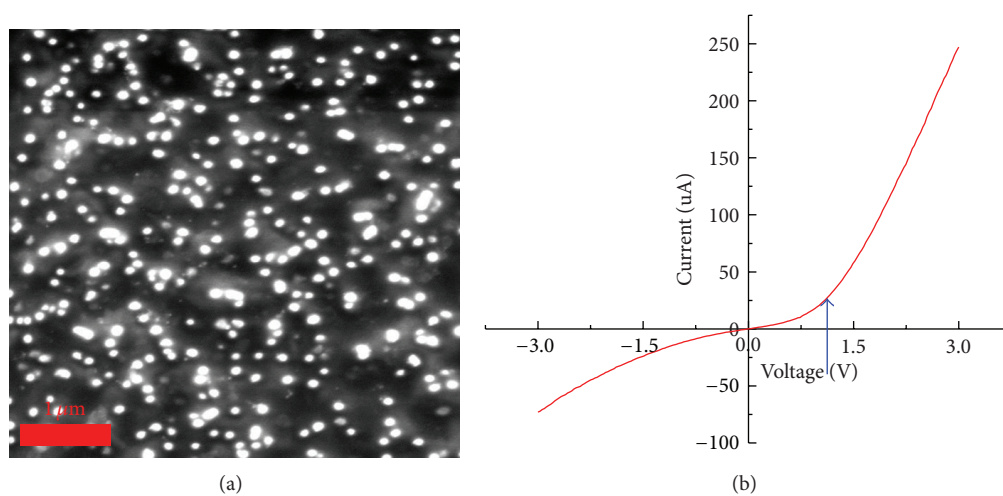


FIGURE 3: (a) Top view SEM image of the ZnO NWs/PMMA hybrids after PMMA infiltration. (b) IV curve of the ZnO NWs/PANI heterojunction blue LED device.

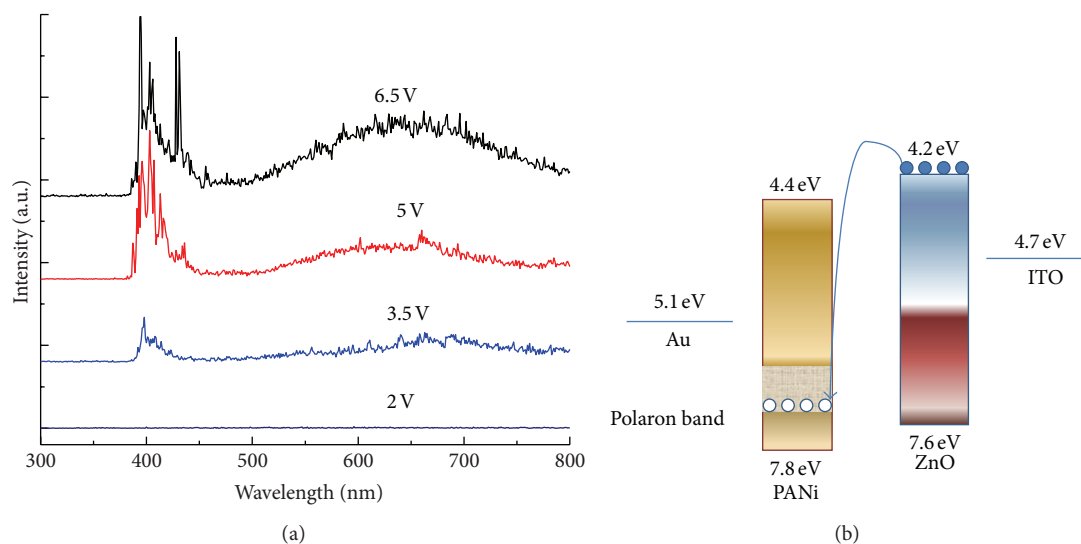


FIGURE 4: (a) EL spectrum of the ZnO NWs/PANi device measured under various biasing voltages. (b) Energy band diagrams of Au, PANi, ZnO NWs, and ITO layers.

spectra. This may be caused by the redistribution of the deep level defects in the ZnO NWs during the device fabrication process.

4. Conclusions

In this paper, an inorganic/organic heterostructure LED device based on vertically aligned ZnO NW arrays and PANi conducting polymer was reported. A blue light emission peak at around 400 nm as well as a broad defect related emission was observed in the EL spectra of the device. The turn-on voltage of the LED device is around 3 V, favoring the low power consumption of the LED device. Also the NWs/PANi composite appears sufficiently robust to absorb large mechanical strain, which is also a fundamental issue in the practical use of organic/inorganic LEDs. Overall, this study demonstrates the possibility of using ZnO NWs/PANi heterojunction for blue light emission. We believe that the performance of such LED can be further improved through adjusting the thickness, carrier densities, and metal contact of the PANi layers.

Acknowledgments

The authors acknowledge the financial support of the NSFC (51072119), Innovation Program of Shanghai Municipal Education Commission (12ZZ139), and the Key Project of Chinese Ministry of Education (12057).

References

- [1] S. Chu, G. Wang, W. Zhou et al., "Electrically pumped waveguide lasing from ZnO nanowires," *Nature Nanotechnology*, vol. 6, no. 8, pp. 506–510, 2011.
- [2] E. Lai, W. Kim, and P. D. Yang, "Vertical nanowire array-based light emitting diodes," *Nano Research*, vol. 1, no. 2, pp. 123–128, 2008.
- [3] X. W. Sun, J. Z. Huang, J. X. Wang, and Z. Xu, "A ZnO nanorod inorganic/organic heterostructure light-emitting diode emitting at 342 nm," *Nano Letters*, vol. 8, no. 4, pp. 1219–1223, 2008.
- [4] R. Könenkamp, R. C. Word, and M. Godinez, "Ultraviolet electroluminescence from ZnO/polymer heterojunction light-emitting diodes," *Nano Letters*, vol. 5, no. 10, pp. 2005–2008, 2005.
- [5] M. Law, L. E. Greene, J. C. Johnson, R. Saykally, and P. Yang, "Nanowire dye-sensitized solar cells," *Nature Materials*, vol. 4, no. 6, pp. 455–459, 2005.
- [6] Ü. Özgür, D. Hofstetter, and H. Morkoç, "ZnO devices and applications: a review of current status and future prospects," *Proceedings of the IEEE*, vol. 98, no. 7, pp. 1255–1268, 2010.
- [7] S. Zaman, A. Zainelabdin, G. Amin, O. Nur, and M. Willander, "Influence of the polymer concentration on the electroluminescence of ZnO nanorod/polymer hybrid light emitting diodes," *Journal of Applied Physics*, vol. 112, no. 6, Article ID 064324, 6 pages, 2012.
- [8] J. H. Jun, K. Cho, J. Yun, K. S. Suh, T. Kim, and S. Kim, "Enhancement of electrical characteristics of electrospun Polyaniline nanofibers by embedding the nanofibers with Ga-doped ZnO nanoparticles," *Organic Electronics*, vol. 9, no. 4, pp. 445–451, 2008.
- [9] J. Kim, S. Park, and N. F. Scherer, "Ultrafast dynamics of polarons in conductive polyaniline: comparison of primary and secondary doped forms," *Journal of Physical Chemistry B*, vol. 112, no. 49, pp. 15576–15587, 2008.
- [10] D. P. Halliday, J. W. Gray, P. N. Adams, and A. P. Monkman, "Electrical and optical properties of a polymer semiconductor interface," *Synthetic Metals*, vol. 102, no. 1-3, pp. 877–878, 1999.
- [11] S. W. Lee, D. O. Cho, G. Panin, and T. W. Kang, "Vertical ZnO nanowires/Si contact light emitting diode," *Applied Physics Letters*, vol. 98, Article ID 093110, 3 pages, 2011.